Integrated Topological Quantum Optics

Mahmoud Jalali Mehrabad

A thesis presented for the degree of
Doctor of Philosophy

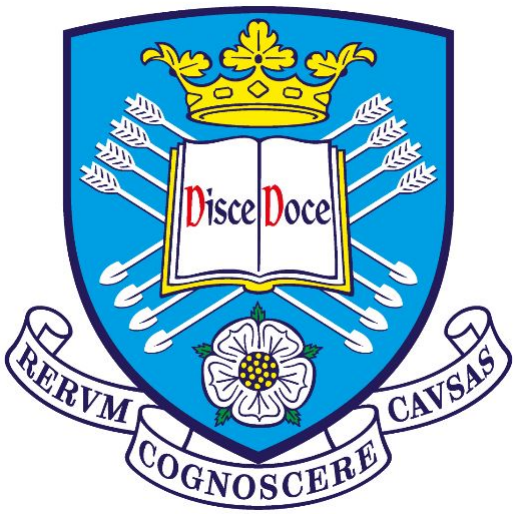

Department of Physics and Astronomy
The University of Sheffield
United Kingdom
October 2021

Integrated Topological Quantum Photonics

Thesis Subtitle

Development of on-chip topological photonics circuits with embedded single quantum emitters

Abstract

This thesis describes the development and experimental investigation of a series of III-V semiconductor nano-photonic circuit elements. A recently emerged approach known as *photonic topological insulators* is used for realization of these photonic components. In this approach, geometrical ideas are utilised to engineer photonic channels to control the flow of light at the nano-scale. Harnessing topological concepts from mathematics and electronic condensed matter physics, these channels are deterministically engineered to offer favourable features such as robustness against imperfections and disorder in the system, as well as control over the direction of transport for propagation of light down to the single photon regime.

Motivated by the extremely appealing features of these *topologically protected* photonic channels, as well as the possibility of realization of fundamentally new concepts and applications, some of the most important optical elements such as straight and bent waveguides, closed optical ring resonators and integrated single/multi channel waveguide-coupled-ring-resonator photonic crystals are developed and investigated experimentally.

Chapter one provides the background and motivation for integrated photonic circuits as an excellent potential platform for quantum computation, commutation, sensing, imaging and metrology, followed by a detailed introduction to electronic and photonic topological insulators. Relevant topological concepts, band structure engineering and key advantageous features for photonic circuits are discussed in detail.

In chapter two, steps involved in development of the nano-photonic topological circuits are discussed, including the iterative process of conceiving ideas, semi-automated nano-photonic design and 3D electromagnetic wave simulations. This is followed by a discussion of the nano-fabrication optimisation and quantum optical measurements of device operation and performance improvement of a series of topological nano-photonic structures. An introduction to the general characteristics of III-V semiconductor quantum emitters, which were integrated in these devices as embedded single photon emitters, is also covered in this chapter.

Chapters 3-5 of this thesis are presented in the *thesis publication format*, in which each chapter is either a published or drafted (unpublished) paper.

In chapter three, the design, simulation and the first experimental demonstration of a hexagonal topological photonic crystal ring resonator with chip-integrated quantum dots is presented. This closed optical circuit is made utilizing

a *Spin-Hall* topological interface, and can serve as a key component for quantum optical filters and gates. The formation of ring resonator modes in this hexagonal optical circuit, as well as the helicity of the modes and topological protection for in-plane propagation of light against defects and sharp bends is demonstrated using finite-difference time-domain simulations. Then, formation, as well as control of the lateral confinement of the modes is experimentally demonstrated via photo-luminescence spectroscopy, utilising GaAs quantum dots as an internal light source in the ring resonator.

In chapter four, a design is proposed in order to further improve and move beyond the optical properties of the Spin-Hall resonator. An upgraded ring resonator is proposed utilizing a *Valley-Hall* topological interface. Significant improvement of the quality factor of modes is demonstrated both in simulations and experiment. To demonstrate the helicity of the modes, first, single photon routing and chiral emission from an embedded QD into a topological guided mode is presented in a straight waveguide geometry. Then, by evanescently coupling the topological ring resonator modes to a topological bus waveguide, chiral coupling of a QD to a resonator mode is presented. Significantly, direct comparison of a trial vs non-trivial topological modes is demonstrated for the first time in the same nano-photonic device.

Chapter five discusses the demonstration of on-chip optical filtering using a novel, integrated, multi-channel topological optical circuit. Device performance flexibility in terms of optical filtering as well as generation and control of the direction of propagation of single photons in this topological photonic *add drop filter* is demonstrated experimentally for the first time.

A summary of results and conclusion of the findings in these thesis, as well as future directions and challenges for these topological photonic circuits is provided in chapter six.

To mum and dad.

There is a crack, a crack in everything. That's how the light gets in.
-Leonard Cohen

Acknowledgements

I would like to thank many amazing people I was most fortunate to get to know in Sheffield, many of whom now I feel blessed to be able to call my friends. I have been most fortunate to be a part of the Low Dimensional Structures and Devices (LDSD) group in the Department of Physics and Astronomy at the University of Sheffield. It has been an honour and tremendous privilege to work with so many amazing individuals from whom I have learned a great deal, both for my professional and personal development. I, therefore, extend my most sincere gratitude to all those who work as part of the LDSD group and to all those who support it, past and present. In particular, I would like to thank my supervisors Maurice Skolnick and Luke Wilson, and my post-doc colleague Andrew Foster, for their endeavours for the group, for their continual guidance during my PhD, and for the opportunity to develop myself as a researcher in the company of experts. Outside of the department, I must also thank my family, friends, and all those who lent a friendly ear, but especially my parents who were the first to teach me the joy of questioning the world around me.

And finally my praise to my friends, Toby, George, Jas, Chris, , Jessica, Sam, Sajad, Yousef, Reza, Mohammad, Amir Hossein and Abolfazl who has had to endure me the most during my studies and to whom I owe so much. Without their continuous unconditional support, time, safe space and love, completing this PhD would not have been possible.

Publications and Presentations

Part of the results presented here have appeared previously in the following papers and presentations:

Papers

1. **M. J. Mehrabad**, A. P. Foster, R. Dost, E. Clarke, P. K. Patil, A. M. Fox, M. S. Skolnick, and L. R. Wilson. **"Chiral topological photonics with an embedded quantum emitter"**, Optica 7(12), 1690 (2020).

2. **M. J. Mehrabad**, A. P. Foster, R. Dost, E. Clarke, P. K. Patil, I. Farrer, J.Heffernan, M. S. Skolnick, and L. R. Wilson. **"A Semiconductor Topological Photonic Ring Resonator"**, Appl. Phys. Lett. 116, 061102 (2020).

3. **M. J. Mehrabad**, A. P. Foster, R. Dost, E. Clarke, P. K. Patil, M. S. Skolnick, and L. R. Wilson. **A chiral topological photonic crystal add-drop filter**, (In preparation).

4. **M. J. Mehrabad**, A. P. Foster, R. Dost, H. Siampour, E. Clarke, P. K. Patil, D. M. Whittaker, M. S. Skolnick, and L. R. Wilson. **Comparison of topological versus conventional nano-photonic waveguides for chiral quantum optics with embedded emitters**, (In preparation).

Conference Presentations

1. PLMCN, France, 2020 (Oral)

2. Quantum Dots, Germany, 2020 (Poster)

3. Quantum Dot Day UK, 2020 (Oral)

4. UK Semiconductors UK, 2018 and 2019 (Oral)

5. Quantum Dots UK, 2018 (Oral)

Contents

Chapter 1

Introduction

1.1 Photonic Quantum Technologies

1.1.1 Background

During the 19$^{\text{th}}$ Century, the idea of an *Analytical Engine*, a machine that can compute and calculate was introduced for the first time. Mankind has transformed this concept into a never-ending stream of efforts to develop progressively more complex computational technologies. With time, the rate and the extent of our species' understanding of himself and the universe has heavily been in correlation with the extent of the computational capabilities available to him. A pivotal point of this journey was around mid 20$^{\text{th}}$ Century, when one of the most outstanding offspring of these endeavours was born: *the computer*. Computers proved to be a revolutionary tool towards deepening our understanding of the past, addressing the most difficult challenges at the present, and paving the way for technological adaptations required for a prosperous future of our species. But this won't be possible if computers' computational capabilities don't match the increasing demand of the increasingly more complex issues mankind is going to have to face.

Computers have become increasingly faster since their invention. Until recently, it seemed like the progress observed in electronic technologies, particularly in the field of semiconductor transistors, could fulfil the famous prediction made by Gordon Moore, conjecturing that the number of transistors on a processor die will double every two years. What became apparent very recently, however, was that this prediction started to increasingly deviate from reality as the transistors got smaller and smaller with fewer number of comprising atoms in each one, proving the issue of quantum mechanical effects detrimentally more and more significant.

While this challenge was becoming more apparent, in 1982 Richard Feynman introduced his revolutionary idea of a computer which would work on the basis of fundamental concepts of quantum mechanics [1]. Such a quantum computer utilizes two of the most important attributes of quantum mechanics- superposition

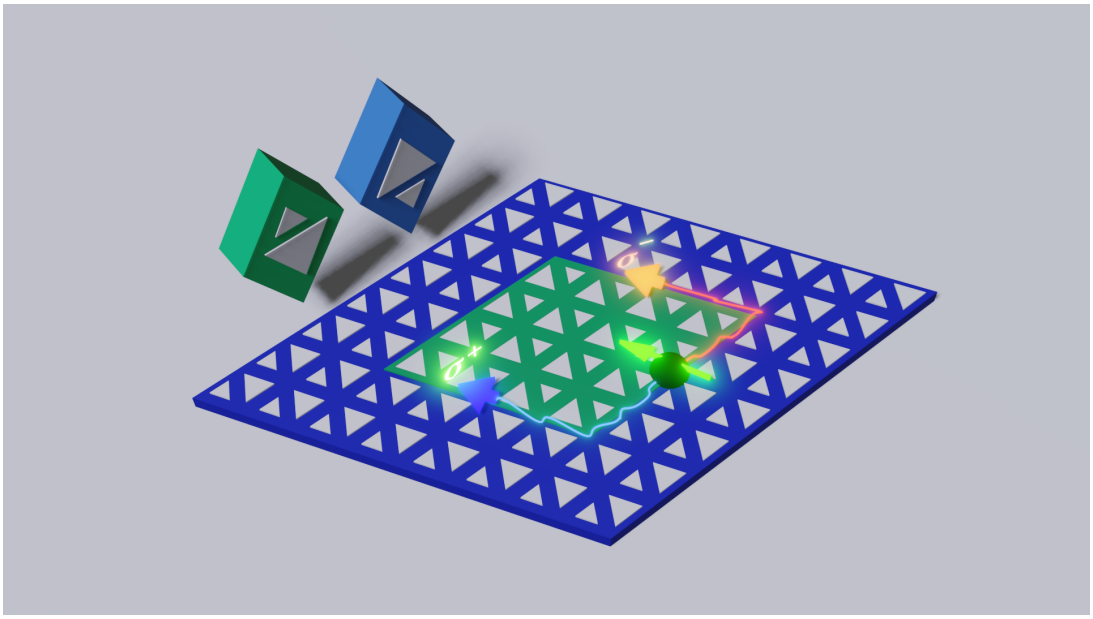

Figure 1.1: Design of a III-V semiconductor photonic ring resonator in which single-photons are generated from integrated QDs (shown as the black sphere). The resonator is made of a Valley-Hall-type lattice, with a rhombic unit cell comprising two dissimilar triangles. The unit cell is inverted at the interface (between the green and blue region) to form confided guided modes. Photons with opposite circular polarisation (the red and blue arrows) propagate in opposite directions of the resonator, robust to sharp bends and fabrication imperfections.

of states and quantum entanglement- in order to introduce a platform for massive scale calculation, highly secure communication and measurements with ultra-high sensitivity. In the following years, schemes and algorithms were introduced for massive scale prime factorisation [2], many-body problems [3] and a quantum internet [4]. It was predicted that compared to classical computers, many such tasks can be performed with significantly fewer physical resources [5]. After outlining the requirements for physical implementation of quantum computer in the early 21st century [6], attempts were made to answer the most challenging question towards fulfilling Feynman's proposal; that is, to find a realistic system that can be a viable candidate to realize the first universal quantum computer.

Various physical implementations of binary quantum systems have been proposed and investigated for this purpose, including the polarization of a photon, discrete energy levels of cold ions, superconducting circuits, the nuclear spin states of an atom, the spin states of an electron, and atom-like two level systems such as quantum dots (QDs). These platforms operate quantum computation on the basis of interactions between a binary system of quantum bits, or *qubits*, and quantum logic gates. One of the most promising candidates for quantum information and computation are semiconductor QDs, due to their many excellent properties such as long coherence, scalability, single-photon generation and

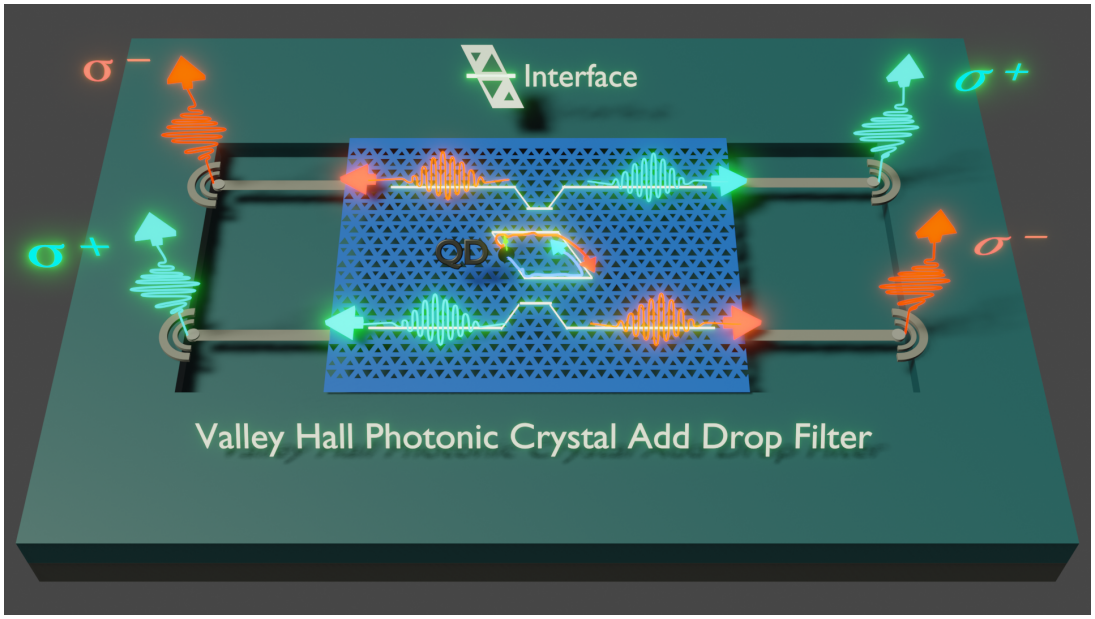

s

Figure 1.2: Design of a III-V semiconductor photonic add drop filter, made of a ring resonator coupled to two bus waveguides. Circularly polarised single-photons generated from integrated QDs in the ring propagate to opposite diagonal ports of the device, forming a multi-channel integrated chiral quantum optical circuit.

possibility of integrated on-chip fabrication [7, 8, 9, 10]. In a QD, the quantum confinement exists in all three dimensions, which results in a system with discrete energy levels, and this system then can be used to encode quantum bits. QDs offer a platform for both studying basic quantum physics, as well as for integration in quantum optical devices.

In the short to mid-term, such integrated quantum optical circuits can form the building blocks for the first universal, fully integrated quantum optical computer, as well as ultra-sensitive quantum sensors. In the longer terms, the resulting technologies from quantum information science could lead to a stream of breakthroughs in many areas, especially in some fields such as genetics, drug designs, neuroscience, astrophysics and robotics, areas in which the scale of computations, as well required precision for sensors are growing exponentially.

Individual optical circuit components, such as waveguides and ring resonators, as well as integrated waveguide-coupled ring resonators and beam splitters serves as building blocks towards realisation of compact and fully integrated all-optical circuits. Device performance of such optical devices can significantly benefit from implementing novel and revolutionary features such as robust one-way flow of light offered by the recently emerged field of topological photonics. As two examples, proposed designs for an optical topological ring resonator and its integration with transport waveguides are shown schematically in Figure 1.1 and 1.2, respectively. Realisation of such robust and novel systems can yield significant progress towards

integrated photonic circuits. Development and investigation of such elements is discussed in detail in this thesis.

1.1.2 Outline and Scope of this Thesis

This thesis focuses on the development of a number of novel topological nano-photonic devices that can be of crucial importance in paving the way towards realisation of a fully integrated quantum circuit comprising III-V nano-photonic structures and embedded light-emitting QDs.

The first chapter primarily focuses on introducing the basic concepts and underlying physics of electronic topological insulators, a recently emerged field of physics bringing topological and geometrical ideas into the field of condensed matter physics. It continues by describing the motivation for implementation of topological ideas in photonics with promising advantages for robust control of the flow of light at the single photon level.

The second chapter describes the methods used to develop and probe the key features of topological photonic systems, starting with an introductory section on the field of self-assembled quantum dots (SAQDs) and their relevant quantum optical properties for implementation in semiconductor photonic devices. The next section discusses the use of the 3D finite-domain-time-difference (FDTD) simulation method to design and optimise topological photonic structures to control the flow of light at the nano scale. The last section of this chapter focuses on the development of a series of nano-photonic devices based on iterative design processes, following by a detailed discussion of several iteration of fabrication and optimisation carried out to obtain high quality photonic devices.

Subsequently, the main chapters of this thesis are presented in the *Publication Thesis format*. These paper chapters demonstrate the development of crucial optical elements for a fully integrated topological optical circuit, starting from a closed optical ring, followed by a a closed optical ring connected to a transport waveguide, then a closed optical ring connected to two transport waveguides. Finally, a comparative study of desirable optical properties in topological vs non-topological optical circuits is presented.

Chapter three is a paper on a Spin-Hall-type topological photonic ring resonator. The underlying physics, band structure, design, fabrication and experimental optical measurements are presented. These results are accompanied by extensive FDTD simulations for further confirmation and demonstration of the device performance.

Chapter four is a paper on improved version of the ring resonator based on Valley-Hall-type photonic interface. Furthermore, the ring resonator is combined with a straight waveguide. This chapter reports the first direct comparison between a topological and a non-topological photonic waveguide mode in the same device, demonstrating why the topological case offers superior optical properties. Additionally, deterministic control over the direction of generated single photons on a chip is presented.

Chapter five reports the draft of a paper on the demonstration of on-chip optical filtering using a novel, integrated, multi-channel topological optical circuit in the configuration of an add-drop fitter. Device performance flexibility in terms of optical filtering as well as generation and control of the direction of propagation of single photons in this structure is demonstrated.

Finally, chapter six provides the summary of the content of this thesis, the conclusions drawn from both simulation and experiment, and possible directions and remaining challenges towards further integration of topological optical circuits for better and more robust control over the flow of light at the nano scale.

Appendix 1 provides supplementary information on electrical and optical properties of quantum dots.

1.2 Topological insulators: from electronic to photonic systems

Conceptualized only a few decades ago, topological insulators now cover an increasingly wide range of areas of physics including acoustics [11], phononics [12], eletronics [13], mechanics [14] and photonics [15]. This section focuses on the geometrical concept of topology in semiconductor condensed matter physics. A description is provided for topological aspects of insulators, how topological ideas were implemented first in electronic band structures leading to novel ways to control the flow of electrons, and then, how topological systems were recently realized in the field of photonics, leading to novel optical circuits with promising properties such as possibility of engineering unidirectional, topologically protected channels for propagation of light in semiconductor photonic structures.

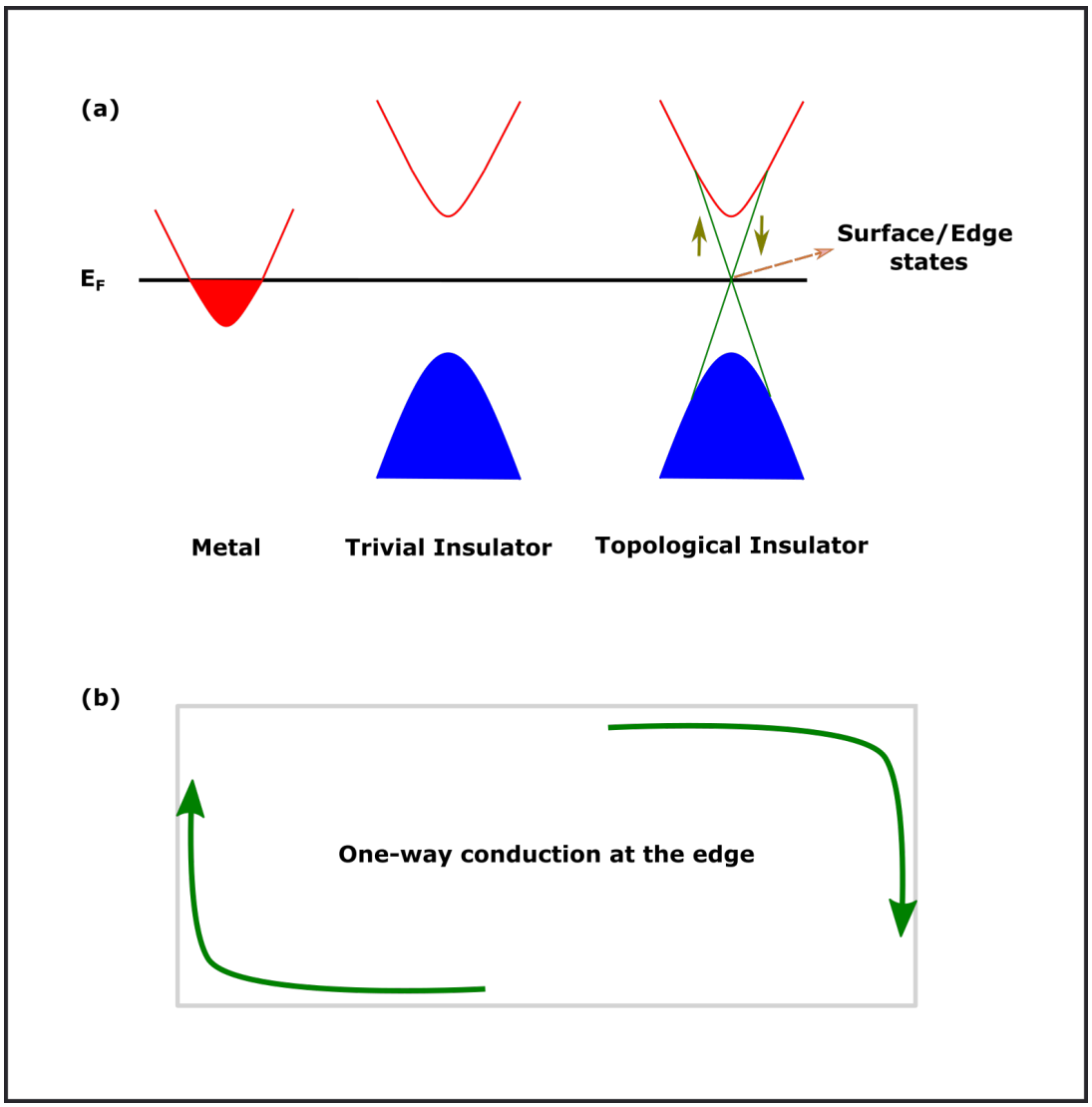

Figure 1.3: (a) Schematic band diagram of conduction (red) and valance (blue) bands for a metal, a trivial and a topological insulator. The black line denotes the Fermi level. (b) Schematic illustration of unidirectional edge conduction in a topological insulator. Conduction at the edge is protected against disorder and defects.

1.2.1 Electronic topological insulators

Quantum Hall effect and topological phase of matter

Topological insulators are materials in which band structure's topology is deterministically engineered such that they are insulating in their interiors or *bulk*, but conducting at the *surface/edges* of the system. They are called topological, since their emergence relies on geometrical ideas from the field of topology in mathematics, and their properties are distinct enough that they are viewed as a new addition to the metal-insulator class. This class of materials started to

draw major attention after it was predicted theoretically, and then subsequently demonstrated that propagation of electrons at the edges of these systems through conducting *edge states* is robust in the presence of disorder and distortions [16]. Electrons with opposite spins travel in opposite directions in these insulators. The existence of such *topologically* protected, unidirectional edge states therefore became the hallmark of a topological system. A description of band diagram of these materials, as well as unidirectional edge conduction in a topological system is shown schematically in Figure 1.3 a and b, respectively.

Topological edge states emerged from the discovery of a series of quantum Hall effects. The starting point can be traced back to research in the early 1980s, which found that the Hall conductance takes exceptionally precise quantised integers when an external magnetic field is applied to a 2D electron gas [16]. This was a quantised or *quantum* version of the ordinary Hall effect, in which, under an external magnetic field, the Lorentz force leads to deflection of electrons in a metal plate. This quantum phenomenon became known the Quantum Hall (QH) effect. QH systems started to draw major attention when three extremely exciting signature features were observed: 1) electrons propagate only at the edges of the system, while remaining localised in the bulk/interior parts; 2) propagation is one-way (unidirectional) depending on the spin projection; 3) the transport at the edge is robust in the presence of defects and disorder in the system [17, 18, 19].

Driven by the potential of these novel and exciting features for both fundamental physics and applications, significant efforts were made to further the understanding of these systems, in particular, to understand why such robust conduction exists. A development was reported in the field of topological physics [20, 21]. The mathematical concept of *topological invariants*, which are properties of a system that remain unchanged under continuous deformation, was paid attention to in particular.

Topology and Topological Invariants

To better understand the robustness of edge conduction in a topological insulator, concepts such as *topology*, *topological invariant* and *smooth deformation* need to be looked at in the context of the geometrical space more clearly. Topology is a mathematical concept that is concerned with the geometrical characteristics of a system. Geometrical properties of an object that remain unchanged under continuous or *smooth* deformations (such as twisting, stretching and bending, opposed to *un-smooth* deformation like tearing or glueing) are called topological invariants of the system. In other words, a topological invariant is *what doesn't change as the system deforms*. An example of a topological invariant is the number of holes within a 2D surface, which is called the genus number (g). g is used to characterise the topology of a given surface, and is defined as:

$$\frac{1}{2\pi}\int_{surface} K\,dA \;= 2(1-g) \tag{1.1}$$

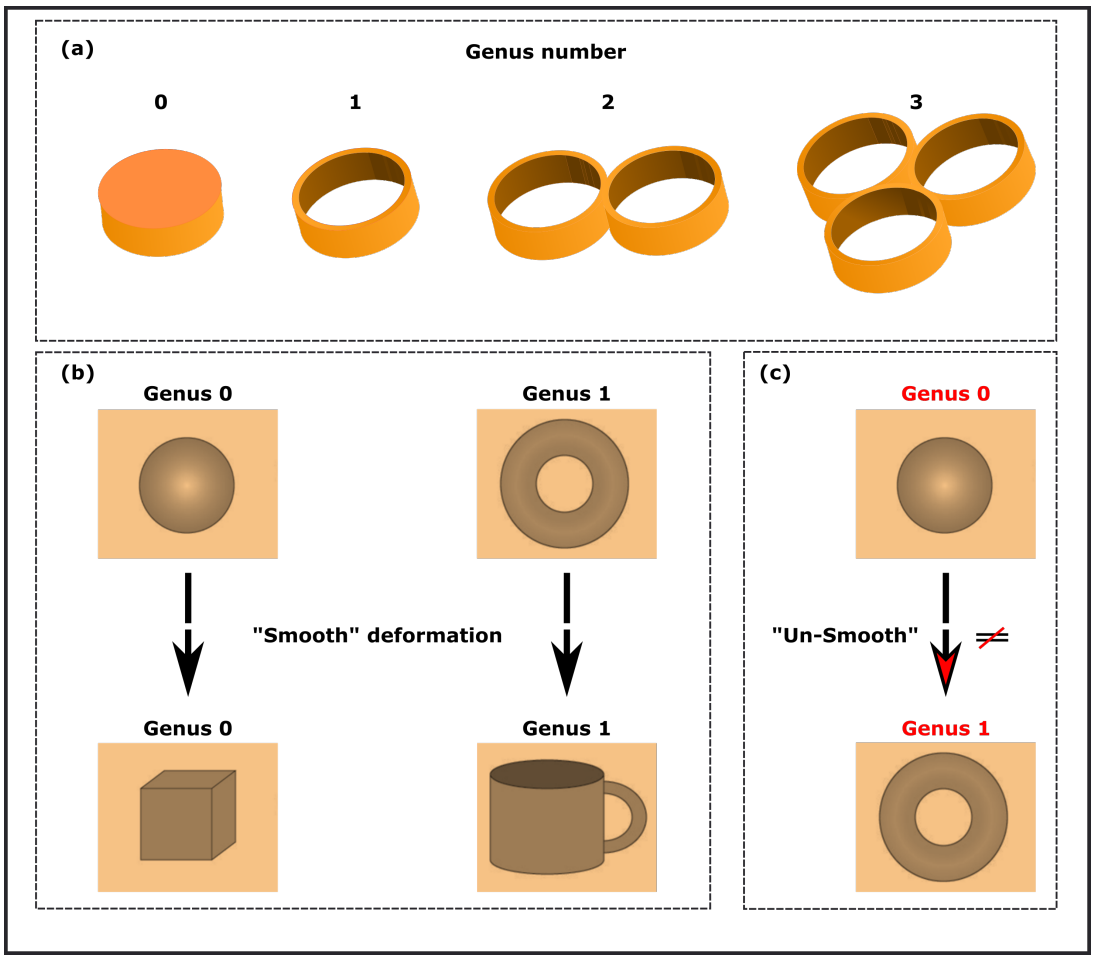

Figure 1.4: (a) Objects classified based on their maximum number of holes or *genus number*. (b) Smooth deformation of a sphere and a doughnut into a cuboid and a mug, respectively. (c) Deformation of a sphere into a doughnut changes its genus number and therefore is not considered a smooth deformation.

where K is the total Gaussian curvatures of the closed two dimensional surface, and is always an integer [22]. Geometrical objects can be classified in different *topological* classes based on their g, as shown in Figure 1.4 a. Once objects are categorised in topological classes, different objects from a certain topological class can be smoothly deformed into each other. For example, as shown in Figure 1.4 b, a sphere and a doughnut can be deformed into a cuboid and a coffee mug, respectively, without changing their topological invariant g. However, deforming a sphere into a doughnut requires cutting a hole in it, which is an un-smooth or discontinuous deformation, resulting in change in its topological class, as seen in Figure 1.4 c.

Such geometrical properties can be considered in condensed matter physics as well. Since a 2D Brillouin Zone (BZ) in momentum space of an insulator is a closed two dimensional surface [22], a torus and a 2D BZ, which has periodic boundary conditions along its edges, are *topologically equivalent*, since a torus can

be formed by curling along the edge of a 2D lattice surface. This provides a starting point from which the concept of topology can be introduced in the momentum space of insulating systems. Topological invariants can be defined in this space to categorize insulators. Un-smooth deformations can be considered through which insulating systems can be deformed into different topological classes.

Consequently, questions now arise regarding fundamental and practical applications of these topological invariants in realistic systems such as condensed matter platforms. A potential answer can be, in particular, to engineer systems such that a useful property of the system becomes *topologically invariant* or *robust*, i.e., this useful property becomes *insensitive* to smooth deformations of the system. To pursue this, a series of topological invariants have been defined for different insulating systems.

Chern number, Spin Chern number and Valley Chern number

After it was observed that in a QH system, Hall conductance is *persistently* quantised as the electron density is varied, attempts were made to bring the concept of topology and topological invariants into QH systems. Due to its robust and quantised nature (similar to the g, the geometrical invariant), the integer of the Hall conduction was given a name, the *Chern number* [21], as one of the first topological invariants to quantify condensed matter systems.

In a paper published in 1984, Sir Michael Berry introduced a series of properties to quantify topological characteristics of a topological insulator in a broader context, called Berry connection, Berry phase, and Berry curvature [20]. The Berry phase, also known as the geometric phase, is the total accumulated phase along a closed path, which can be calculated using an integral around a closed loop in the parameter space, from which Berry connection, which is a local vector potential, and Berry curvature, which is a gauge field, can be calculated. The integral of the Berry curvature over the whole BZ gives an integer, which is called the Chern number of the system. These concepts can be intuitively understood by making an analogy between classical Maxwell's equations and quantum mechanical equations. Berry phase, Berry connection and Berry curvature can be viewed as a *magnetic flux*, *vector potential* and *magnetic field*, respectively. Chern number can be viewed as the number of *Dirac monopoles*. Universal mathematical methods for numerical calculation of the Chern number in a broader context and their calculation methods for different discretion BZs are described in detail in the literature [20, 23].

In an insulating system, if the Chern number acquires a non-zero value, it is said that the system is *topological* or *topologically non-trivial*. The value of the Chern number can give information on the number of edge states in the system. The introduction of these topological invariants and concepts into condensed matter physics were a pivotal point in realisation of topological insulators, since they provided a methodical approach to topologically classify insulators.

Over the past decades, different versions of QH systems were introduced and specific topological invariants were defined to describe them. The QH systems

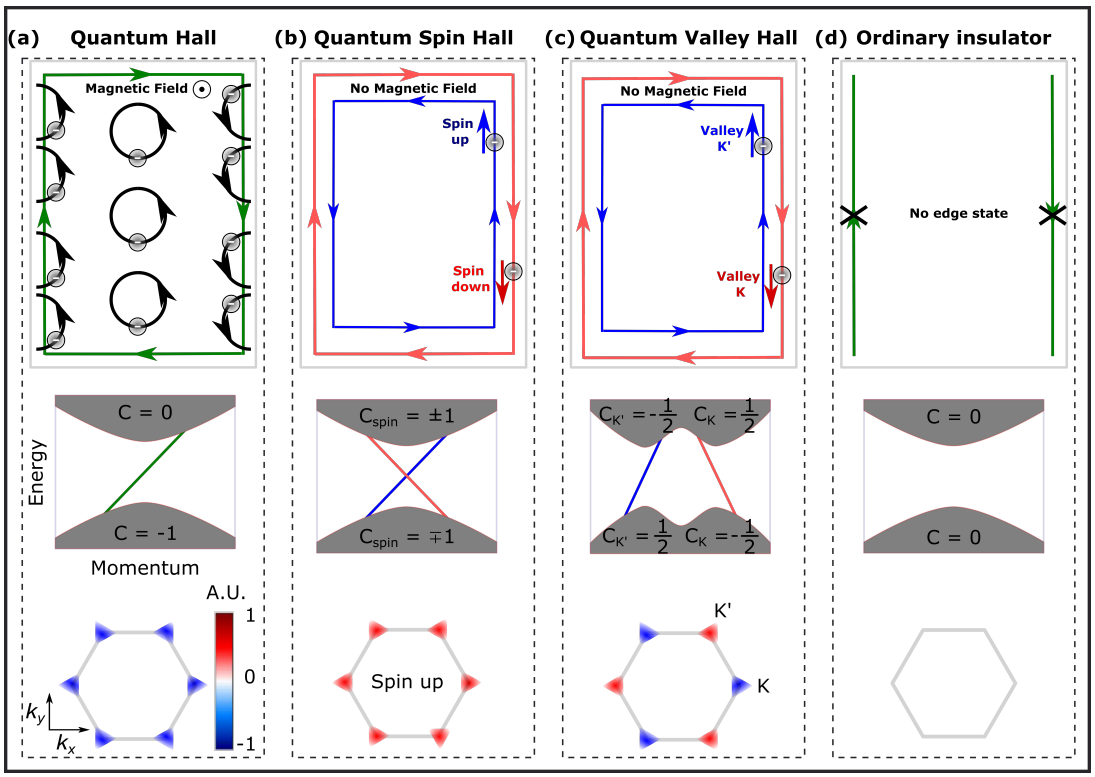

Figure 1.5: Schematic diagram (top panel), edge state dispersion and associated topological invariant (middle panel) and the Berry curvature over the first BZ, which is denoted by a hexagon (bottom panel) for different QH effects. (a) A quantum Hall system with a single one-way edge state propagating along the boundaries, through which backscattering is prohibited. The edge state only exists in the presence of an external magnetic field, and the direction of the field dictates the direction of propagation. (b) In a quantum Spin Hall system, which is similar to a QH system in terms of forbidden backscattering through its edge states, there are two channels instead of one, each one supporting the propagation of electrons with one of the spin projections. Unlike the quantum Hall effect, there is no need for an external magnetic field. (c) In a quantum Valley Hall system, which is similar to the Spin Hall system, the edge states emerge at two Valleys (K and K' points). (d) A trivial insulator shown for comparison.

most relevant to this thesis and their electronic dispersion and topological invariants are described later in this chapter.

Time reversal and inversion symmetry

The underlying physics of formation of topological edge states is heavily correlated with symmetry of the systems. In particular, time reversal and inversion symmetries play a significant part in understanding QH effects. Time reversal symmetry (T) is the theoretical symmetry of laws of physics under time reversal transformation t $\rightarrow$ -t. Inversion symmetry deals with the symmetry of systems

under mirror transformation. By deterministically breaking or preserving these symmetries, different versions of QH systems can be realized and classified [24]. The role of these effects in topological systems is discussed in the next section.

Quantum Hall, Quantum Spin Hall and Quantum Valley Hall phases

Robust and unidirectional edge conduction in QH systems made them extremely exciting. However, since the QH effect requires strong magnetic field and cryogenic temperatures, work continued to address some of these challenges by finding alternative approaches to preserve the robust unidirectional conduction without those restrictions. In particular, since the underlying reason for unidirectionality of edge states in a QH system is that the external magnetic field breaks the time reversal symmetry of the system, the quest began to find an alternative approach to break T and form chiral edge states. One of the proposed schemes, which later was named the Quantum Spin Hall effect (QSH), was essentially combining two QH system, where, instead of one, a pair of edge states exists, each for one of the spin projections of electrons, without the presence of a magnetic field. In these systems, an alternative mechanism can lead to breaking T to realize a QSH system. This mechanism is related to the interaction of the spin, which is a fundamental property of electrons, with orbital angular momentum.

In 2005, a group of researchers who were working on graphene discovered a novel topological phase in their system, which was shown to be the predicted QSH [25]. They showed that in a QSH system with electrons with sufficiently strong spin-orbit coupling (SOC), even without the presence of an external magnetic field, it is indeed possible to open a band gap and achieve one-way electronic edge states. The reason is, electrons with opposite spins experience different forces in the presence of a strong SOC, and each spin projection can be *locked* to a certain direction. This mechanism was named *spin-momentum-locking*. It was shown that, as predicted, at the edge of such systems, unidirectional edge states, or *one-way electronic transport channels* appear, where the group velocity of these channels is locked to the electronic spin: electrons with opposite spins propagate in the opposite direction, and the propagation is protected against electron backscattering [26, 27, 28, 29].

In 2007, it was shown that similar to a QSH system, where the spin degree of freedom gives rise to spin-locked topological edge states, another binary degree of freedom exists as a potential candidate for realization of edge states under T, called the Valley degree of freedom [30]. In a momentum space of condensed matter system, a valley refers to a point with a local energy extremum. Positive and negative valleys can be engineered in the momentum space by breaking the inversion symmetry (P) of the lattice and opening a band gap. When two lattice with opposite Valley properties are interfaced, edge states can arise at the interface and the system is called a Quantum Valley Hall (QVH) system. Edge states at opposite valleys have opposite group velocities and electrons at opposite valleys propagate at opposite direction. This mechanism is known as the *Valley-momentum-locked* propagation. A schematic illustration of these quantum Hall

effects, their edge state dispersion and Berry curvature is shown in Figure 1.5, in addition to a conventional insulator for comparison.

Recently, quantum Valley-Spin Hall systems were introduced, in which both spin and valley degree of freedom coexists, with more complex edge state configurations. These systems are yet to be fully investigated [31].

Degree of robustness in different quantum Hall systems

How *robust* an edge state in a topological insulator system is against deformation depends on its topological invariant and edge state configuration. A QH system, has a single edge state, and its topological invariant, the Chern number, is non zero across the first BZ. This well defined topological nature, and the presence of only one edge state at each frequency leads to suppression of variety of strong disorder [16].

This is not quite the same for a QSH system. A QSH phase can be viewed as two copies of the QH phase, each one for one of the spin projections. The Berry curvature which defines the spin Chern number in the QSH systems, is spin-dependent. For example, the Berry curvature of electrons with spin-down is negative, and that of electrons with spin-up is positive, both of which have the same integer magnitude. The total Chern number, which is the sum of the two spin-up and spin-down spin Chern numbers is therefore zero. This is viewed as a relaxed condition compared to the Chern number in a QH system. The consequence of this relaxation is that the degree of topological protection reduces. QSH edge states are topologically protected as long as the disorder and defects in the system doesn't flip the spin of the propagating electrons, which can introduce *inter-spin* scatterings. One can view this via attributing *magnetic* nature to defects and disorder, the sort of which cause spin-flipping in the system, against which there is no topological protection [32, 33]. In QVH systems, a similar argument can be presented. The valley Chern number takes a non zero value only if half of the first BZ is considered for the calculation of the Berry curvature. In this case, the valley Chern number takes a half-integer value at each valley, with opposite signs at opposite valleys (K and K'). The total Chern number will be zero across the whole BZ. In this case, the protection exists against disorder and defects that doesn't flip the sign of the Berry curvature, leading to a process known as *inter-valley* scattering [33, 34]. In summary, a QH system has a non-zero Chern number across the whole BZ of the system; a QSH system takes integer spin Chern number for each spin channel individually; a QVH system takes half-integer valley Chern number at opposite valleys, but across half of the BZ. The result of this is that degree of protection becomes limited in a QSH and QVH systems compared to that of a QH system. Additionally, having integer spin Chern number compared to the half-integer valley Chern number in QVH systems might mean that QVH systems are less protected than QSH systems, but this is still not fully understood and needs to be investigated more rigorously. That being said, there are still a wide variety of disorder and defects that QSH and QVH systems have been shown to be protected against. Sharp bends, lattice

disorder, and certain types of defects that do not break the symmetry of the lattice are among these. From a practical point of view, intrinsic directionality of the edge states, together with the protection against these type of imperfections make these systems extremely desirable for a variety of applications, and for investigation of new physics. Also, further development can lead to improvements in the degree of offered protection in these systems.

The discovery of quantum Hall effects has opened a new avenue for exploring novel and exciting realms of physics. In addition to QH, QSH and QVH systems, other effects such as Spin-Valley, fractional, integer and anomalous effects were introduced which has helped to deepen our understanding of quantum systems. Intensive research on these effects has been leading toward landmark discoveries in many fields of semiconductor sciences and technologies. The discovery of topological insulators, which is *a new phase of matter* and received the 2016 Nobel prize in physics, became one of the most recent and exciting offspring of this field.

Before discussing the topological properties of photonic structures, the concept of topology and how it was introduced in electronic band structure is discussed in the next section. These concepts will later be used to explain the formation of photonic edge states.

Band inversion and trivial and non-trivial topological band structure

It is useful to consider what is (can be) topological about insulators. The answer lies within the band structure characteristics of insulators. When the topologically distinct geometrical objects discussed in the previous section are considered, similar concepts can be applied to insulators, based on the properties of their electronic valance and conduction band structure. For instance, two insulators can be *topologically* equivalent if they can be deformed smoothly into each other. Here, smooth deformation means without closing the bandgap (i,e without turning into a conductor) as a result of the deformation. In contrast, two insulators are topologically distinct if they cannot be deformed into each other without closing the electronic band gap in the process, and the deformation will be considered *un-smooth*.

When a conventional insulator is considered as as an example, the band diagram of the insulator consists of a valence and a conduction band, separated by a forbidden region or a *bandgap*. This is shown in Figure 1.6 c. If a topological invariant for such an insulator is defined as the sign of the bandgap energy, then the insulator A and B will have positive and negative invariants, respectively, and therefore, they will belong to two different topological classes. One can *smoothly* modify either the insulator A or B, so that their bandgap size changes, and as long as the sign of the gap isn't changed, the topological invariant of each one remains unchanged. However, if insulator A, is modified into insulator B, in a way that the conduction and valance bands of A becomes the inverted version of B, this will not be a smooth deformation, since the bandgap sign is changed, as shown in Figure 1.6 c. This will only be possible through an intermediate step, in which the gap needs to be closed first.

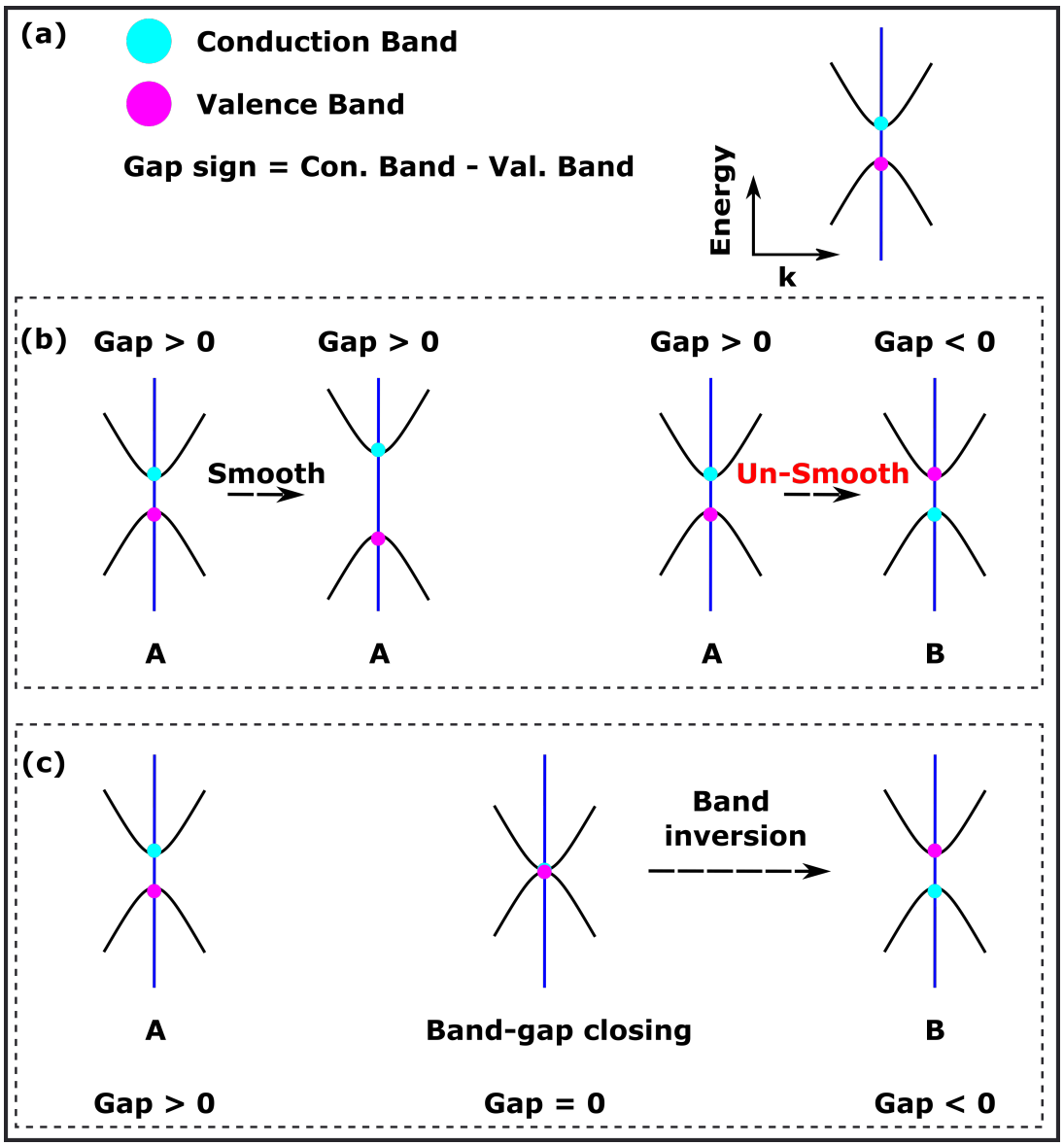

Figure 1.6: Topological band inversion. A trivial insulator, when un-smoothly deformed, can go through a band inversion process, through which the valence and conduction bands are flipped around. This can happen through a band-gap closing intermediate step.

An insulator with a conventional band structure, where the standard order of the valence and conduction bands are preserved (insulator A in Figure 1.6) is called a *trivial* insulator, while insulators with inverted band structure are called *non trivial* insulators (insulator B). This band inversion, when utilised deterministically, is the corner stone of engineering topological edge states, which is discussed in the next section.

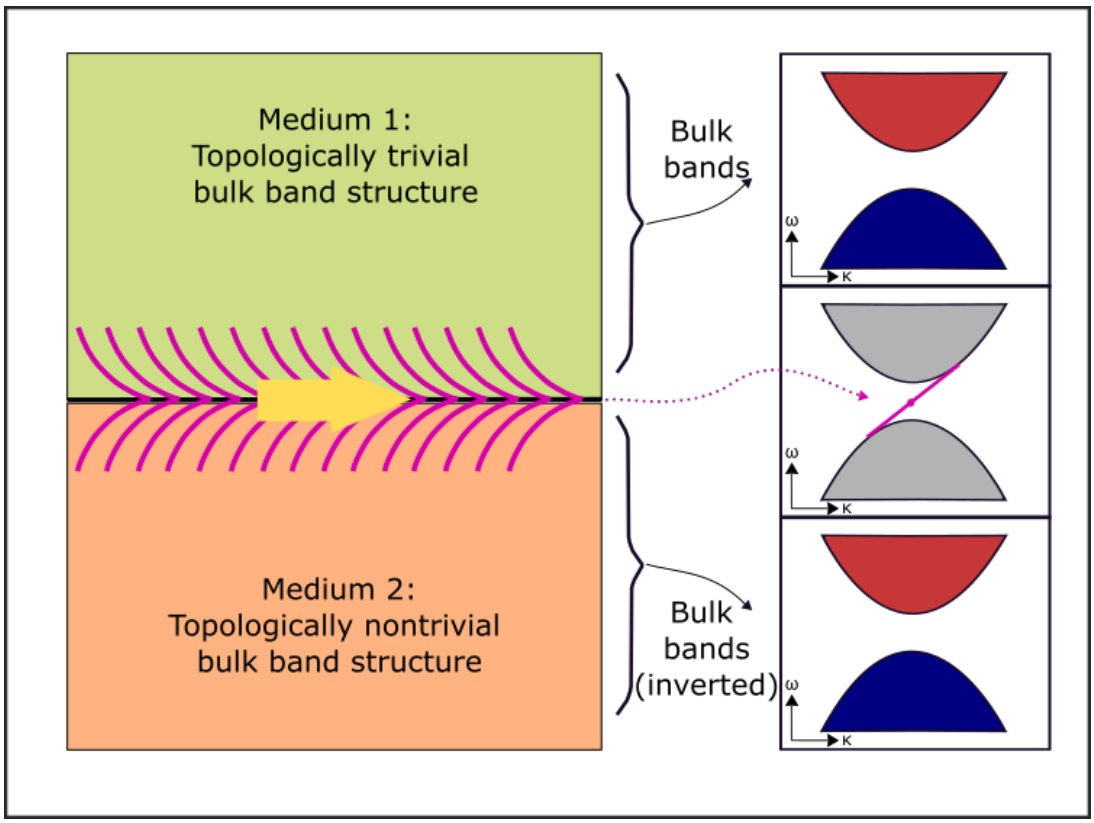

Figure 1.7: Formation of in-gap edge states at in interface between two topologically distinct insulators with inverted band structure. Adapted from [35].

Band Inversion and Formation of Topological Edge States

When a topologically trivial system is interfaced with a non trivial insulator in a periodic structure, bands cross the band gap at the interface between the two. This happens since in a periodic system, the only way to continuously go from a trivial insulator from one side of the interface to a non trivial insulator on the other side is, as discussed, through closing the gap, which leads to the formation of bands at the interface. These states are called (depending on the system) interface, surface or edge states, and since this topological band inversion is the underlying physics for their formation, they are known as *topological edge states*.

This process starts by selecting an insulator with a trivial band structure, meaning the valence and conduction bands are ordered just like a conventional insulator; the valence band has a lower energy than the conduction band. Step two is to modify the first insulator in an un-smooth or topologically distinct way, so that the bands of the second insulator are the inverted version of the first one. This is a non trivial insulator because of this distinct band inversion. Step three is then to introduce an interface between the two. From a topological point of view, continuous transition, which is essential in a periodic system, between the first and second insulator bands can happen only if a band is closing the gap and crosses the band gap at the interface. Therefore, as shown schematically in

Figure 1.7, at the interface between the two topologically distinct structures, in-gap interface or *edge* states form.

Over the last few decades, such topological ideas have been utilized in electronic systems, to achieve scatter-free edge conduction. The suppression of backscattering originates from two features of these systems; firstly, there is no scattering into the bulk modes since edge states only exist at the edge (everywhere else there is a bandgap and there is no band to scatter into), and, secondly then for the interface itself, since there is either only one edge state (in QH system) or only one edge state for each direction (QSH system) of propagation, there is no alternative state to scatter into for a one-way propagating electromagnetic wave. Suppressed scattering and intrinsic unidirectionality therefore exist at the same time in these systems, making them extremely favourable for a variety of applications. It is worth noting that when the QH systems were being studied, the need to have an external magnetic field to form such robust edge states was considered a limitation. Discovery of QSH effect offered a solution in systems with sufficiently strong spin orbit coupling.

The possibility of robust unidirectional and reflection-less transmission of current in these fermionic systems inspired the search for similar concepts in other platforms, including ultra-cold atoms, mechanical structures, phononics and photonics. In particular, due to the important properties of robust light propagation and directional coupling, topological photonics has become an emerging field both for novel physics and applications in integrated photonic circuits. Recent theoretical and experimental studies have shown that practical platforms for deterministic control of topological properties of photonic band structure, as well as engineering unidirectional edge states of opposite helicity propagating in opposite directions are possible at both optical and telecommunication wavelength. These features can help to address some of the main challenges in integrated quantum optics, particularly for photon routing, where one of the main obstacles is controlling and reducing photon scattering losses due to fabrication disorder, bends and splitters in photonic devices. That is where topological features such as backscattering free propagation against bends and mild deformations can promise a novel approach for protected on-chip quantum optical routing and manipulation, which is the subject of the next section.

1.2.2 Photonic topological insulators

Overview

After the demonstration of the QSH effect in graphene, attempts were made to extend the concept of topological insulators in other platforms such as photonics. One particular property of the electronic band structure of graphene offered a significant breakthrough towards this goal. Carbon atoms in graphene are arranged in a honeycomb crystal symmetry, in which conduction and valance bands cross at a point known as the Dirac point or Dirac cone (in 3D k-space). Through careful perturbation, band gaps can be opened around this crossing point, with

both topologically trivial and non trivial properties, such as direct and inverted band topologies, setting the ground for realization of topological edge states.

This picture inspired the attempt to realize topological edge states in a photonic system, via engineering a photonic analogue of graphene, i.e. a honeycomb photonic crystal which has the photonic analogue of graphene's electronic band structure. Once a Dirac point in the band structure is identified, deterministic tuning of the lattice parameters can lead to opening a band gap around this point. Additionally, it is possible to open gaps with inverted band topologies, and similar to electronic topological insulators, when an interface between the two is introduced, edge states can form at the interface. The photonic Dirac point, bandgap opening, band inversion and formation of photonic topological edge states will be discussed in detail in this section. This follows a brief overview of the recent approaches, directions and current related demonstrations in the field of topological photonics.

Brief review of the historical development of topological photonics

The first proposed scheme for realisation of a topological photonic insulator was put forward via breaking time-reversal symmetry. This was demonstrated via applying external magnetic field in microwaves in gyro-optic photonic crystals in 2008 [36, 37, 38].

Robust, unidirectional edge states in these gryo-optic photonic crystals were demonstrated experimentally for the first time in 2009 [39]. This approach was based on the integer Quantum Hall effect which is a strong effect in the microwave domain, but weak for visible and infra red or telecommunication wavelengths (only very small topological band gaps can be opened). The challenge still remained to bring these effects from QH fermionic to bosonic systems, i.e., to realize edge states without needing spin-orbit coupling. The second series of theoretical schemes were then proposed and experimentally realised. This is achieved by aperiodic coupled resonator systems [40, 41, 42], using polarization as spin in PCs [43] and birefringent metamaterials [15].

The first significant demonstration of a photonic topological insulator was reported in 2013 [44]. It was shown that similar to Dirac dispersion in graphene, in an optical honeycomb lattice, the bands cross at a point due to lattice symmetry, then temporal modulation breaks the symmetry, and a gap opens for visible light frequencies. It was demonstrated that the transport occurs around the perimeter, bypassing defects in the system.

A major development was reported in 2018, where a topological photonic laser was proposed and demonstrated. The idea was to harness topologically protected transport of light to make a robust laser [45, 46]. A laser with a cavity acting as a superconductor for light (no resistivity for transport of the lasing mode) was shown to be highly non-linear in a system with gain (where spontaneous emission is replaced by stimulated emission), robust against edges, defects and disorder, with high efficiency and single mode operation. Recently, a number of other developments have been reported, including proposed novel

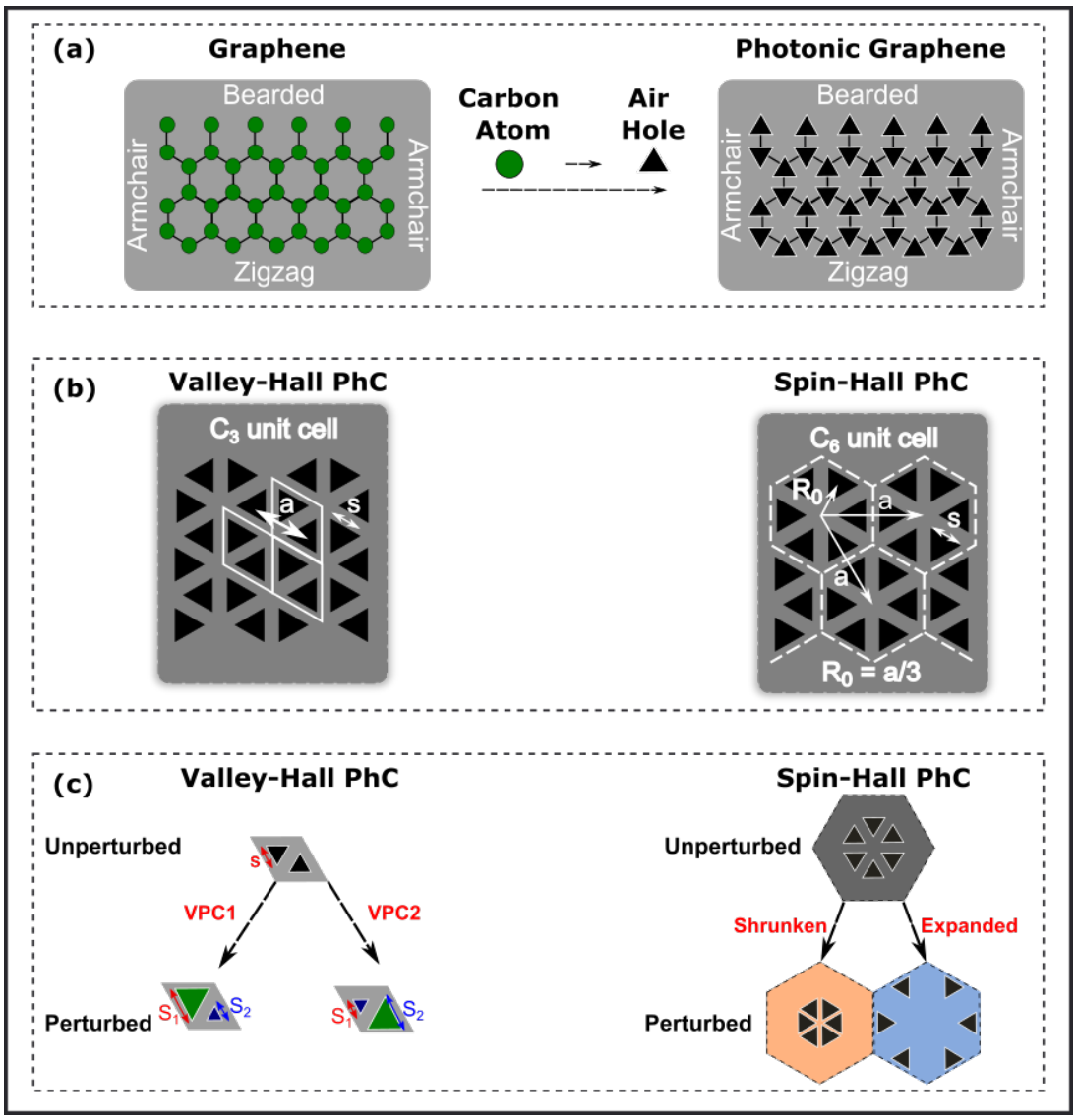

Figure 1.8: (a) Engineering a photonic analogue of graphene by replacing the carbon atoms with air holes. (b) Same honeycomb lattice viewed in two different pictures, one with C3 (left) and the other with C6 (right) symmetries. (c) Perturbing the C3 unit cell and C6 lattices in two distinct way to form two distinct perturbed PhCs.

lasers, waveguides, cavities and resonators. These systems have been introduced and experimentally realised in 1D [47], 2D [48] and 3D [49, 50]. In particular, a branch of topological quantum optical interfaces have been recently realised via introducing QDs in PhC as embedded quantum emitters [48]. The following section focuses on topological properties and edge states in 2D semiconductor PhCs.

1.2.3 Photonic Graphene

One method for the realisation of a photonic topological insulator is to engineer a PhC analogue of Graphene to emulate the QSH effect. The first step is to replace the carbon atoms in the electronic Graphene structure with air holes to form a honeycomb lattice. This periodic PhC for example, as shown in Figure 1.8 a, can comprise triangular air holes (or elliptical, circular, etc). Just like in the electronic band structure of graphene, such a photonic lattice has a pair of bands crossing at a point in its band structure, around which topological bandgaps can be opened.

Similar to graphene, boundaries of such photonic periodic structure will have armchair, bearded and zigzag configurations, and different interfaces can be engineered at different boundaries. The second step involves opening a bandgap in the photonic band structure of the system. One way to do this is to modify the lattice in one of two distinct ways. For example, via inversion symmetry breaking, as discussed later in this section, is based on the QVH effect. Using this approach, two different perturbed photonic Graphene lattices can be realised with C3 lattice symmetry, which are labelled as VPC1 and VPC2 in Figure 1.8 c. A second approach is to be used via break the C6 symmetry of the lattice instead, by expanding and shrinking the unit cell to form two different perturbed PhCs. This alternative method leads to a photonic analogue of the QSH effect, as discussed later.

Spin-Hall vs Valley-Hall band structure

To understand the difference between QSH and QVH photonic edge states, the evolution of the band structure before and after perturbation is discussed for each case. For the QSH case, as an example shown in Figure 1.9a, a honeycomb lattice comprising 6 equilateral triangular holes is considered. The unit cell is perturbed by either shrinking or expanding the cluster. The band structure of the unperturbed (unmodified), shrunken and expanded crystals show that in the perturbed case, a bandgap opens at the Gamma point. For the QVH case, as shown in Figure 1.9 e, the same lattice is considered, but this time the system is viewed as a C3 symmetry lattice, with a rhombic unit cell comprising two triangular holes. By reducing the size of one and increasing the size of the other, and then doing this the opposite way, two perturbed PhCs are formed, with a band gap opened at the K point.

1.2.4 Photonic quantum Spin-Hall effect

The electronic QSH effect discussed previously might not seem compatible with the photonics version at first glance. Photons are bosons and unlike electrons, they do not possess half-integer spins, which is a prerequisite condition for spin-momentum-locked edge states. Now questions arise about how the QSH effect is emulated in a photonic system. The answer lies partially within the polarisation

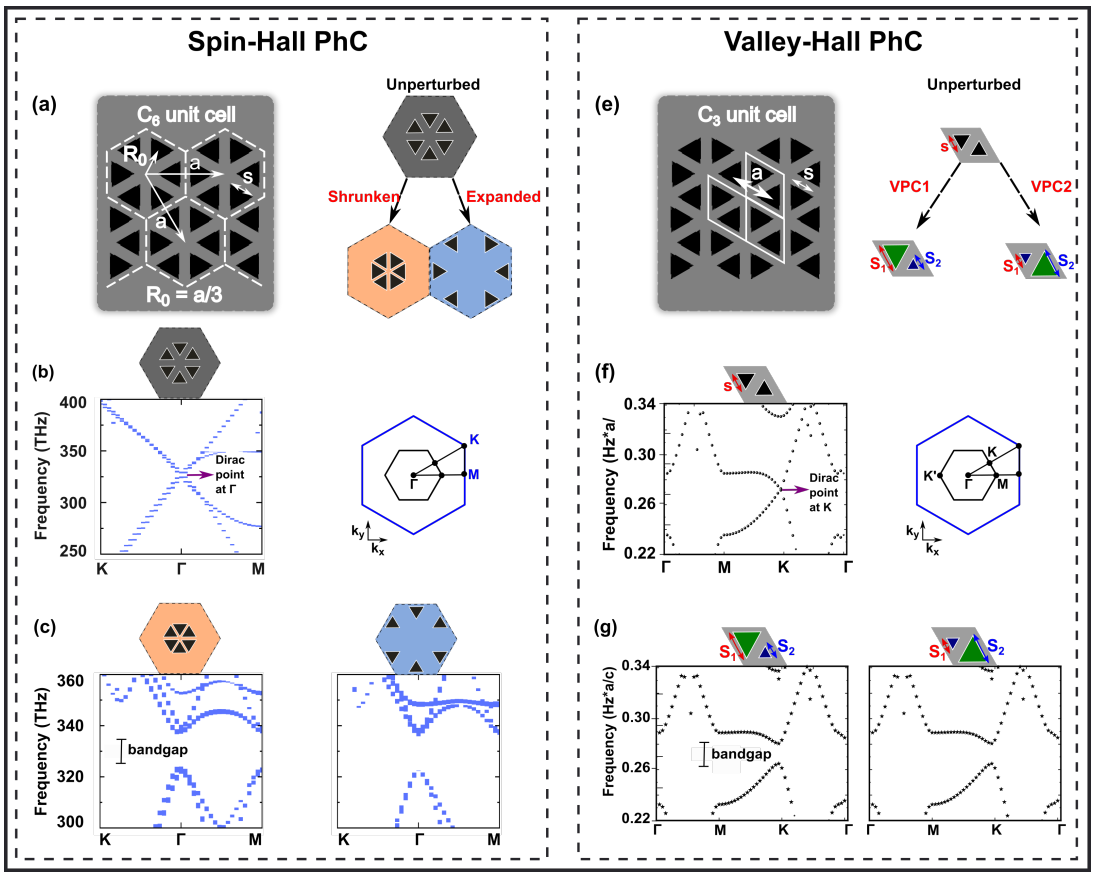

Figure 1.9: (a) Schematic of a Spin-Hall lattice. The honeycomb lattice is perturbed by shrinking and expanding the C6 hexagonal unit cell. (b) Band structure of the unperturbed lattice, with a Dirac point at the Gamma point of the first BZ. (c) Band structure of the perturbed lattices. Both shrunken and expanded lattices have a full band gap at the Dirac point. (e) Same photonic Graphene lattice, but this time viewed as a C3 rhombic unti cell. Two different lattice can be made by perturbing the holes, making one bigger and the other one smaller and then the opposite way around for the second PhC. (f) Band structure of the unperturbed lattice but using the C3 picture. A Dirac point at K can be seen. (g) Band gaps open for both VPC1 and 2 at the K point (and K' point, not shown).

properties of photons. Even in free space, photons possess spin properties thanks to circular polarisation, which can be utilised for realization of spin-locked characteristics for edge states in photonic systems. In 2015, a honeycomb lattice in a dielectric membrane was first introduced to realise such an effect [51], which was later experimentally demonstrated [48]. Using the crystalline symmetries in these systems, it has been shown that photons inside periodic structures can acquire a spin-like property named *pseudospin* which can emulate the time reversal operator of fermionic systems, attributing non-trivial topological properties for photonic bands. For their resemblance to the electronic QSH effect, these systems are known as photonic QSH systems, and they have a pair of counter propagating

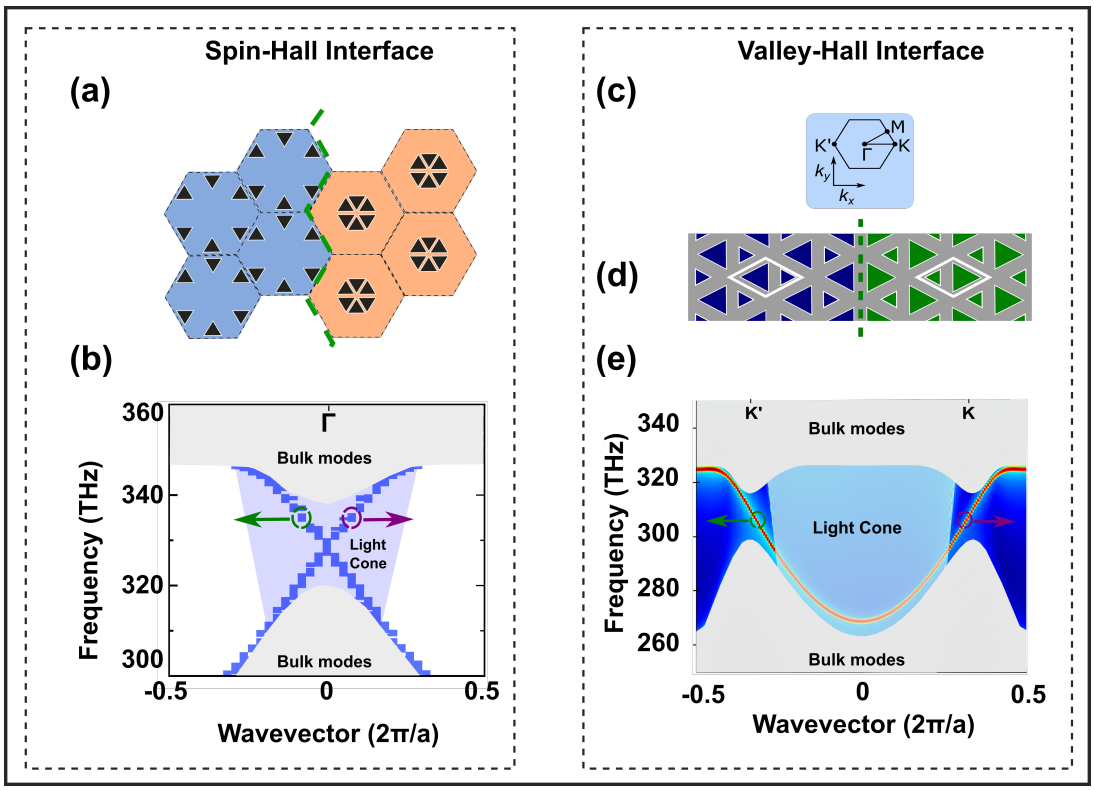

Figure 1.10: (a) Schematic of a Spin-Hall interface, between a shrunken and expanded lattice. (b) Edge states at the interface. Two bands with opposite group velocity, one forward running mode (purple arrow) and one backward running mode (green arrow) cross the band gap at the gamma point. The edge states in this case are above the light line. (c) High symmetry points of the first BZ. (d) A zigzag interface between two Valley-Hall lattice. (e) Edge states for the Valley-Hall interface, with the forward and backward running modes at K and K' points, respectively. The edge states are below the light line. These edge state are tuned to operate at near-infra-red frequencies. Lattice parameters for the Spin-Hall (Valley-Hall) interface: 445nm (266nm) lattice constant, 140nm (106nm and 160nm for the small and big triangle, respectively) triangle side length and 170nm membrane thickness. These parameters are defined in Figure 1.9.

photonic channels. The pseudospin degree of freedom guarantees the formation of these spin-polarized topological photonic edge states. When a QSH interface is considered, as shown in Figure 1.10 a, by interfacing a shrunken and an expanded PhC, a photonic interface can be realized. Figure 1.10 b shows the projected band structure for this interface. Two bands with opposite group velocity cross the bandgap at Gamma point. The in-gap crossing of these edge states and their opposite group velocity demonstrate their resemblance to electronic QSH edge states. It is worth noting that these edge states are above the light line, therefore they are lossy due to out of plane scattering that exist for modes above the light line in general [52]. However, for in plane propagation, photonic transport

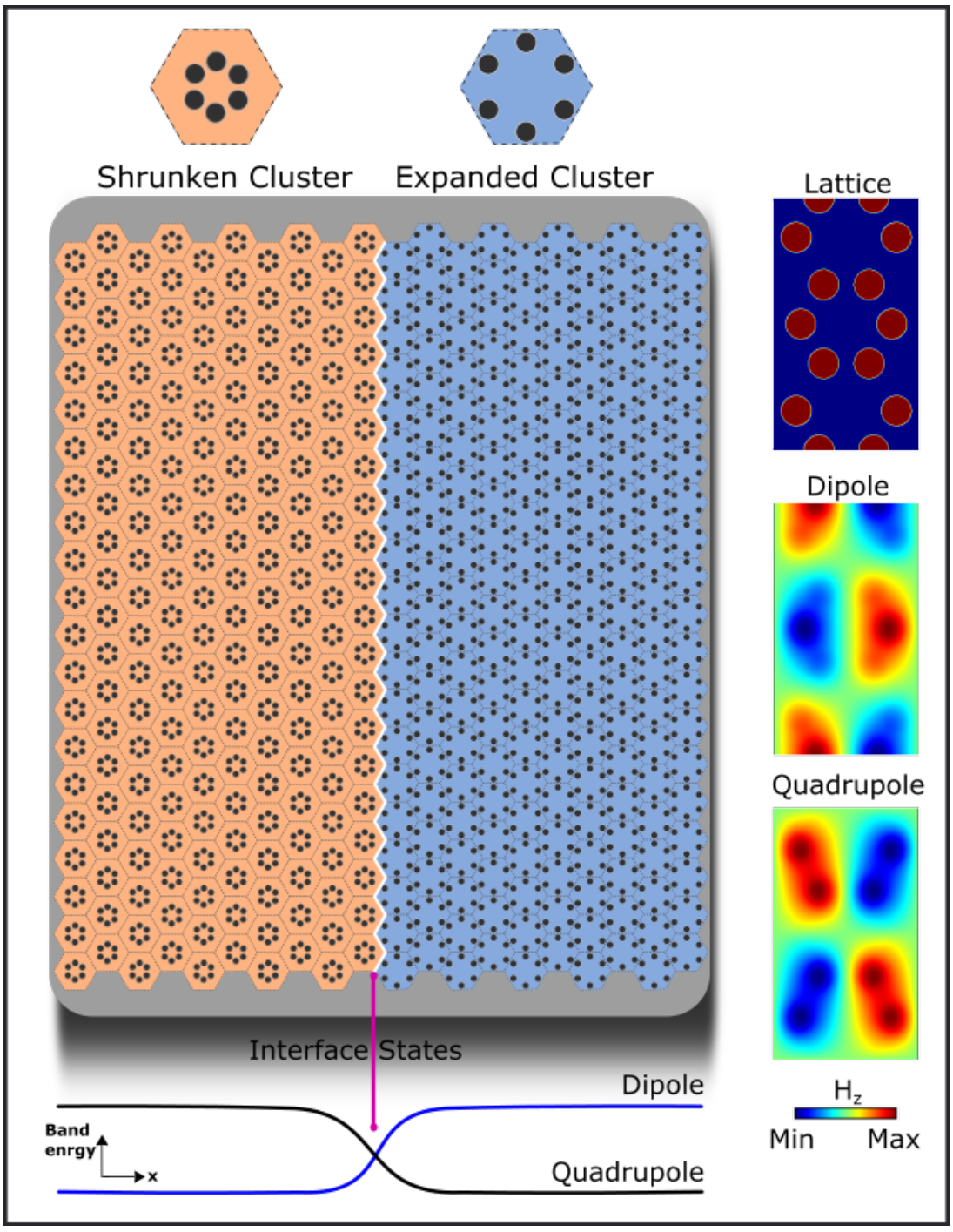

Figure 1.11: A topological photonics interface between shrunken and expanded hexagonal unit cells. Dipole and quadrupole symmetries of conduction and valence bands invert at the interface, giving rise to formation of a pair of edge states.

through these modes is shown to be protected against sharp corners and certain defects and disorder [48].

1.2.5 Photonic quantum Valley-Hall effect

Similar to the pseudospin degree of freedom, another binary degree of freedom was recently proposed [53] and demonstrated [54] as a potential candidate to yield a new photonic topological phase via breaking inversion symmetry, known as the valley degree of freedom, similar to the electronic QVH effect [30]. It was predicted that in such a system, photons at opposite valleys would propagate in opposite directions, since the edge state dispersion of a QVH insulator exhibits opposite signs of the group velocity at opposite valleys. As an example, a photonic QVH interface is shown in Figure 1.10 c. Two inverted C3 unit cells are used to form an interface with broken inversion symmetry. The projected band structure of the interface indeed reveals two bands crossing the band gap with opposite group velocity at K and K' points.

Photonic topological band inversion and formation of edge states

To illustrate the process of formation of edge states in photonic graphene, schematic of a honeycomb photonic lattice is shown in Figure 1.11.

Here, six concentric circular holes form a hexagonal unit cell, with the unit cells arranged in a periodic structure with triangular lattice symmetry. By concentrically moving the circles inward in the hexagonal unit cell (the orange unit cell in Figure 1.11), a photonic bandgap is opened. The photonic eigenstates of the valence band of this lattice have a dipole (p-like) symmetry, while the conduction band shows a quadrupole (d-like) symmetry. When the six circular holes in the hexagonal unit cell are concentrically moved outwards, another photonic insulator is. The eigenstates of this expanded lattice show the inverted symmetry of the shrunken one. The valence band now has quadrupole symmetry, while the conduction band shows dipole symmetry. At the interface between the expanded and shrunken lattice, the dipole and quadrupole bands cross the bandgap to preserve the continuity of the bands across this lattice. These crossing edge states are the channels through which photons can propagate in a robust, one-way manner.

1.2.6 Photonic QSH and QVH topological invariants

The difference between a QSH and a QVH photonic system comes from the difference between the topological invariant of these two systems.

Similar to the electronic case, for a Spin-Hall system, each pseudospin channel acquires a non-zero spin Chern number, which characterizes this system as a QSH topological system with protection against certain types of disorder and defects, as long as the disorder doesn't flip the pseduspin property of the propagating photons. In contrast, for the Valley-Hall interface, the spin Chern number of the system is zero. However, the Berry curvature acquires a half integer value with opposite signs around K and K' points. As long as the disorders or defects in the system do not introduce inter-Valley scattering, propagation though these channels is protected. Examples of Berry curvature, the integral of which across

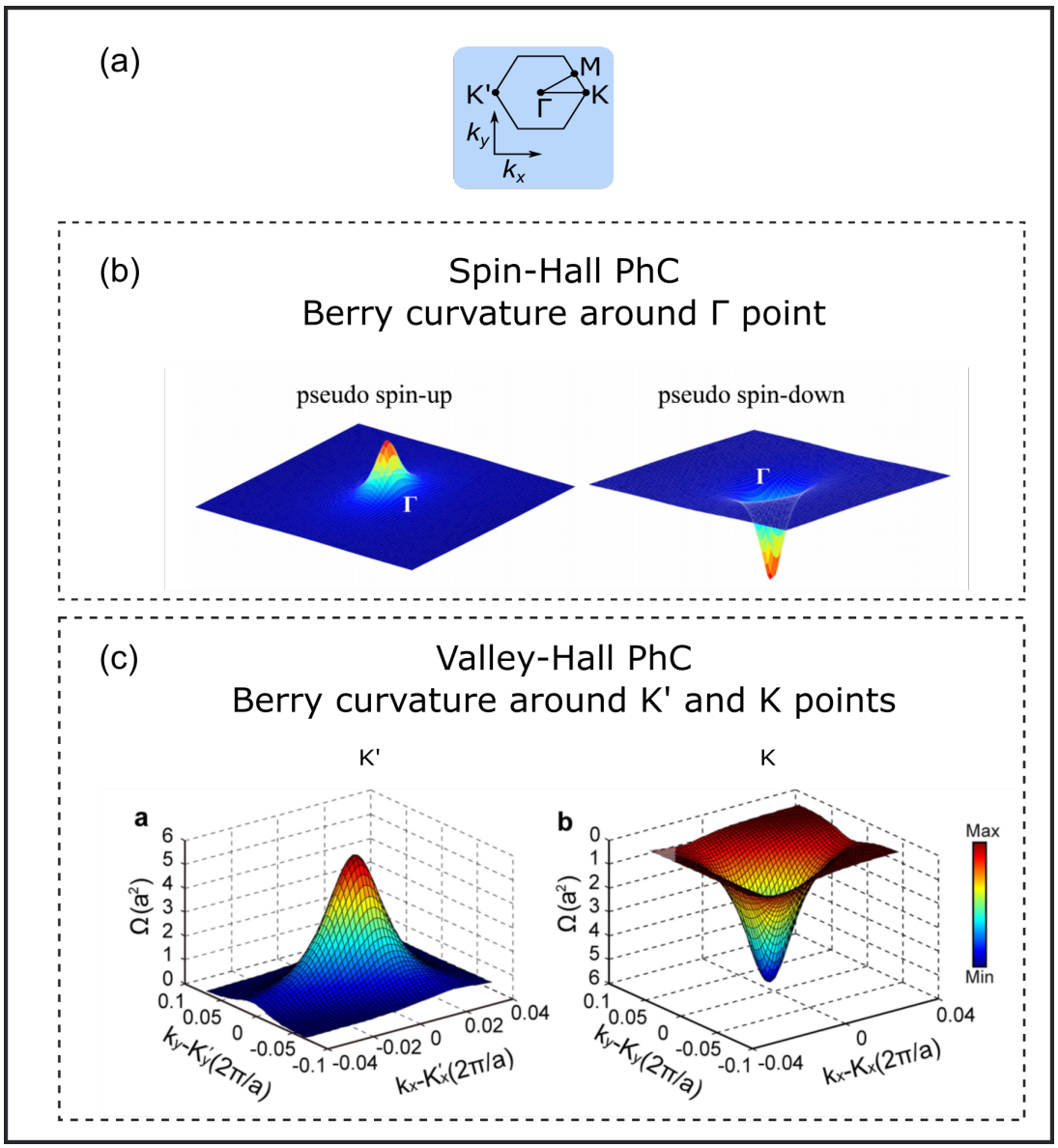

Figure 1.12: (a) High symmetry point of a honeycomb lattice. (b) Spin Chern number for Spin-Hall edge states. Opposite Chern number for opposite spin channels is observed at Gamma [55]. (c) Opposite Berry curvature at K and K' valleys for the Valley-Hall lattice. The total Spin Chern number is zero for a Valley-Hall interface state [56]. The colour map in shows the Berry curvature.

the BZ of each lattice gives the Chern number, for photonic spin and valley Hall systems are shown in Figure 1.12b and c, respectively.

1.2.7 Examples of photonic QSH and QVH interface

Figure 1.13 shows a few examples of Spin Hall lattices and perturbations required to achieve a topological interface. In these systems, usually a photonic analogue

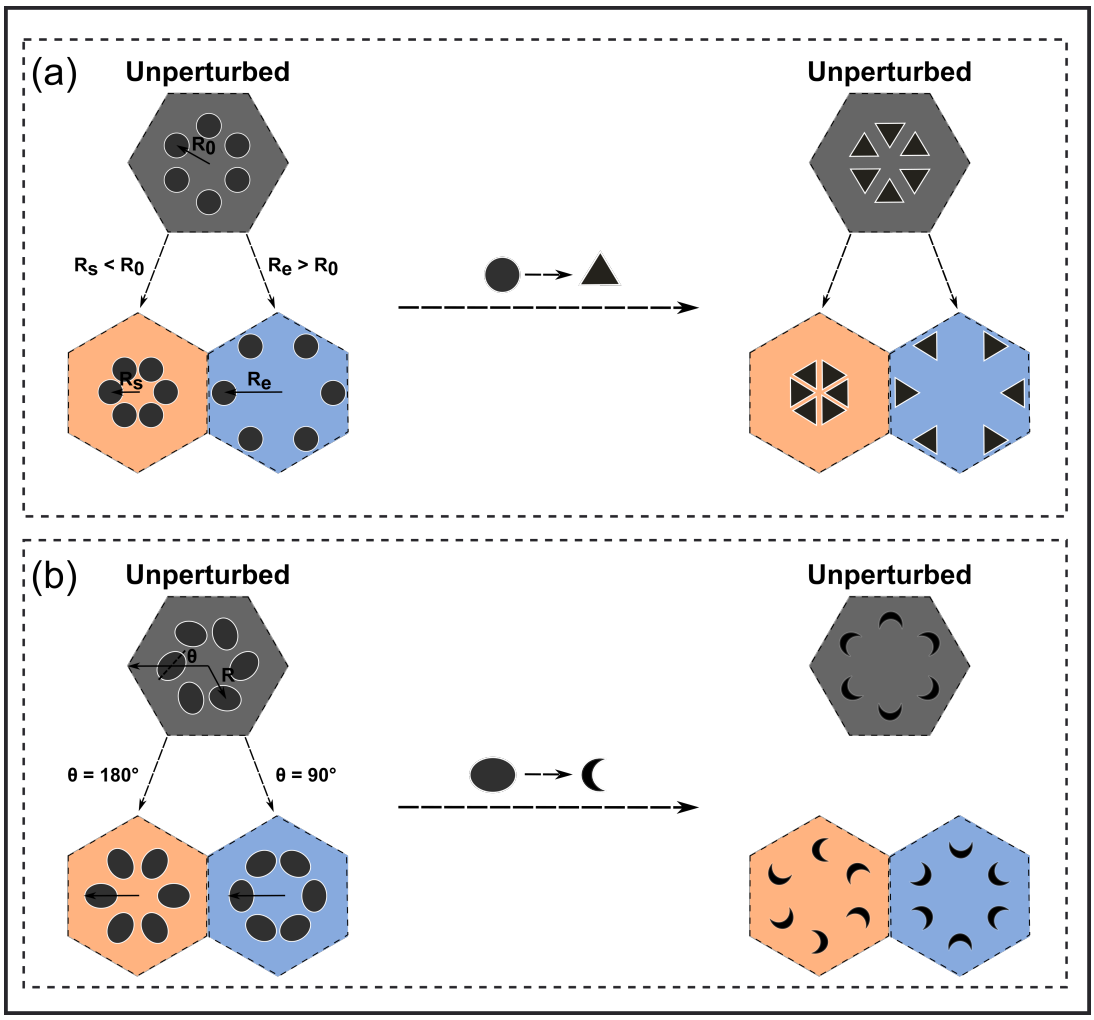

Figure 1.13: Examples of Spin Hall PhCs. (a) Honeycomb Lattice with shrunken and expanded circular (left) and triangular (right) holes. (b) 90/180 degrees rotation as two distinct perturbation for a hexagonal unit cell comprising six ellipsoidal (left) and moon-shape (right) holes. The interface between these perturbed lattices supports a pair of counter propagating edge states in an analogue with QSH physics.

of Graphene is designed in the form of a honeycomb lattice with a hexagonal unit cell, then the unit cell is perturbed in two distinct ways to open a band gap for each case, one with the inverted band topology of the other. Two commonly used methods for perturbation are shown. The first method is performed on the basis of shrinking and expanding the unperturbed unit cell [55, 57]. The second method is based on rotating the air holes in two distinct ways [58, 59].

Examples of Valley-Hall lattices are shown in Figure 1.14. The perturbation here is mainly for the purpose of creating an interface with broken inversion symmetry. Examples of perturbation of two-hole [60, 54] and single-hole unit cells [53, 61] and the resulting QVH interfaces are schematically presented.

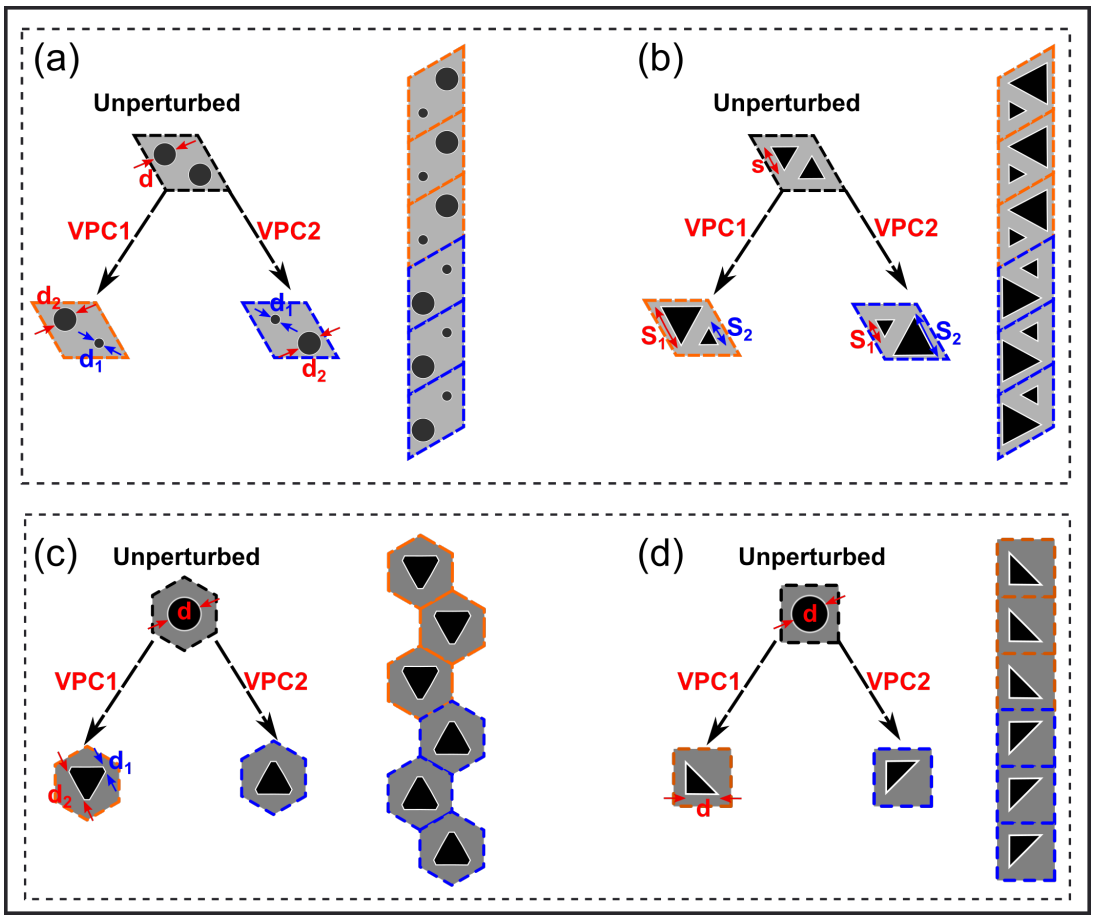

Figure 1.14: Examples of Valley-Hall PhCs in a honeycomb lattice with a rhombic unit cell comprising two (a) circles and (b) triangles. Changing the size of the two holes asymmetrically can break the inversion symmetry of the lattice and open a photonic bandgap. (c) and (d) Alternative example of QVH interface via perturbing a single-hole unit cell into two inverted triangles. In each case, the strip shows the interface.

1.2.8 Bearded and zigzag topological edge states

As discussed previously, a honeycomb PhC can have different types of interface at its boundaries, similar to that of electronic Graphene. When different perturbed honeycomb lattices are interfaced with each other, depending which boundary of the PhC is chosen, different interfaces can be realised [62]. This is schematically shown in Figure 1.15. As an example, an unperturbed honeycomb PhC is perturbed into two QVH PhCs, labelled VPC1 and VPC2. By interfacing a certain boundary of the PhCs, as shown in Figure 1.15 c, bearded or zigzag interfaces can be formed. Edge states for each interface can have different gradient and group velocity.

Edge states for the bearded and zigzag interface are shown in Figure 1.16. The zigzag interface in this case supports a single mode with a high group velocity

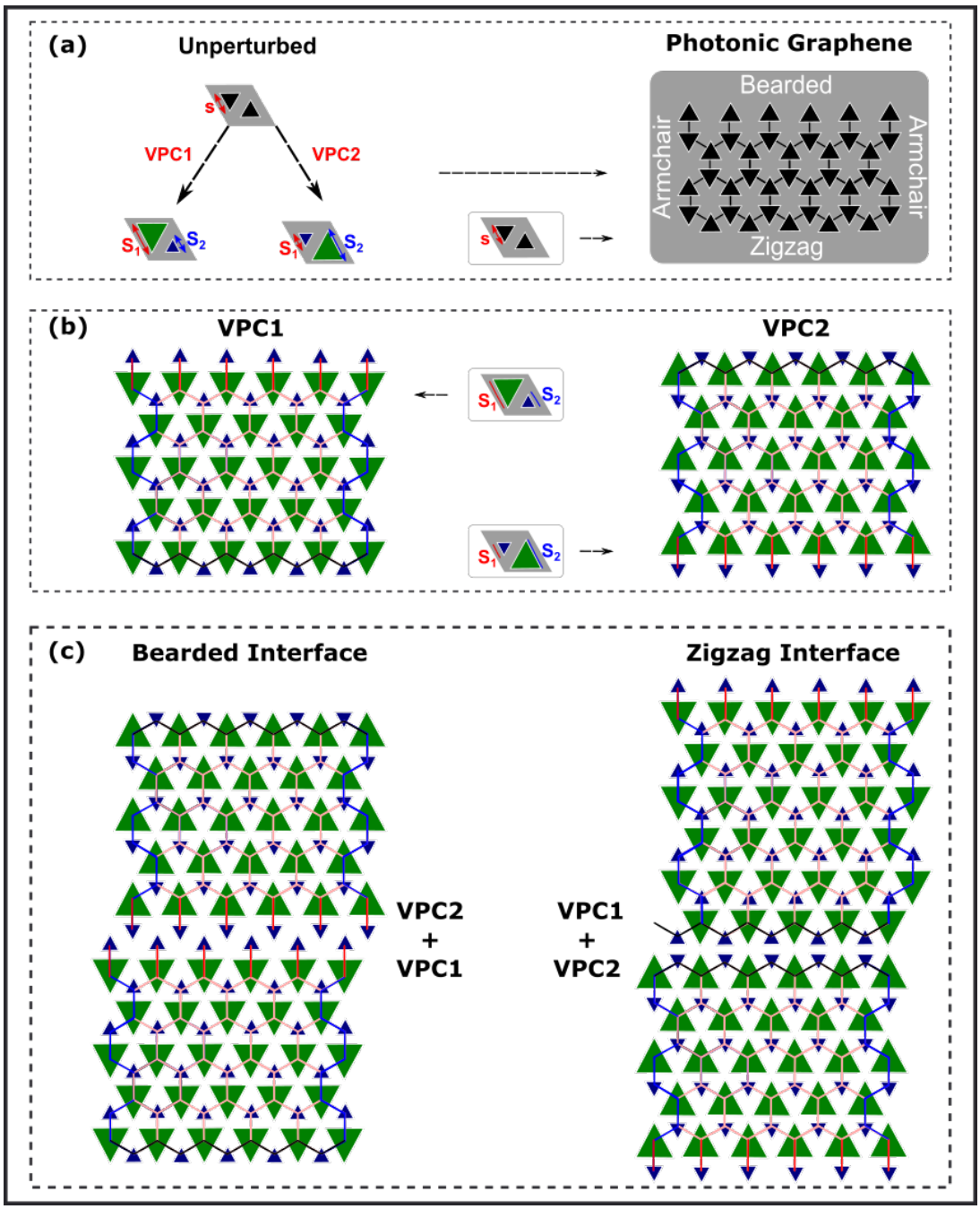

Figure 1.15: (a) Photonic Graphene viewed in a C3 unit cell picture, perturbed in two distinct way labelled as VPC1 and VPC2 with asymmetric triangular air hole sizes. (b) Two PhCs made of each perturbed unit cell in (a). (c) Bearded and zigzag interfaces formed depending on the orientation of the PhCs.

(fast-light behaviour) across the band gap. Two possible configurations labelled as Zigzag Interface (1) and (2). The difference results from whether the big triangles are interfaced or the small ones, resulting in different group velocity for

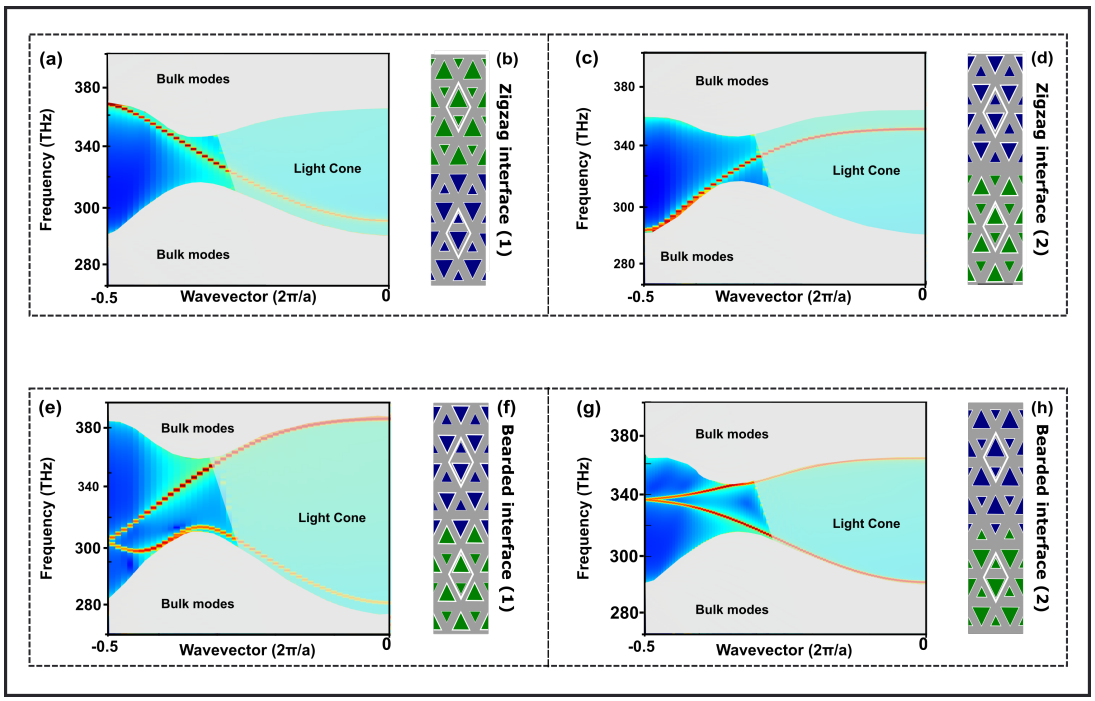

Figure 1.16: Projected edge state dispersion for (a) Zigzag interface (1), (c) Zigzag interface (2), (e) Bearded interface (1) and (g) bearded interface (2). Schematic of each type of interface is shown in (b), (d), (f) and (h), respectively. In calculation of the band structures, the same lattice parameters as the ones in Figure 1.10 are used in all cases.

the edge states. The bearded interface has a different edge state configuration. Two bands exist, instead of one, which are degenerate at the edge of the BZ.

1.2.9 Trivial vs non-trivial topological edge states

It has been recently shown [62] that only one of the two bands in the bearded interface bands has non-trivial topological properties, while the other is a trivial band for which there is no topological protection. These bands are labelled accordingly in Figure 1.17 c. This difference in topological protection can be investigated via formation of a waveguide with sharp bends. Injected light into such waveguide can only propagate without loss for the non-trivial mode. 3D Finite Domain Time Difference (FDTD) simulations show that light is indeed only protected for the non-trivial mode. A detailed study of this type of interface is discussed in chapter 4. Additionally, the group velocity of the non-trivial mode decreases near the edge of the BZ. As a result, the density of photonic states at frequencies near this slow light region increases. Such an interface can therefore be used for slow-light physics, which has potential applications in enhancement of the light-matter interaction.

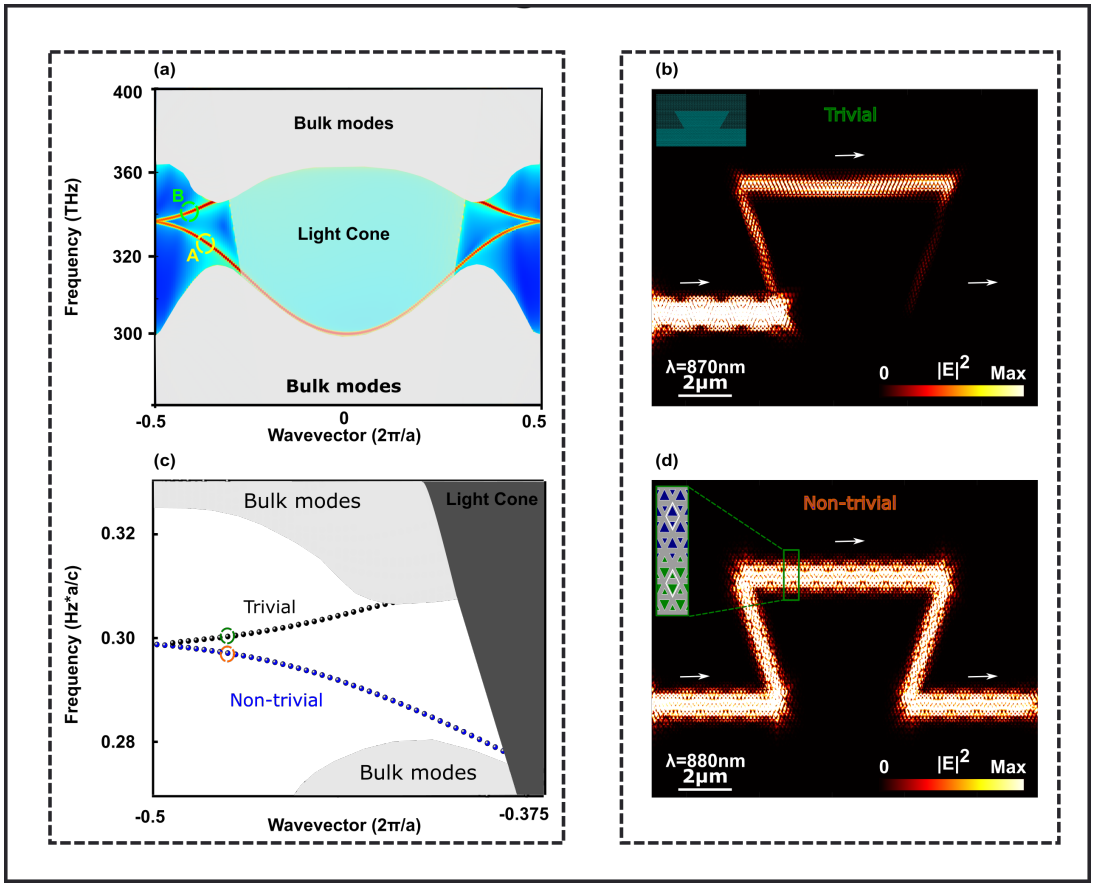

Figure 1.17: Full edge state dispersion of the QVH bearded interface (2). (c) Edge state dispersion near the edge of the BZ, with two bands labelled as trivial and non-trivial. Slow-light behaviour can be predicted due to the reduction of the group velocity near the point that the bands cross. Time-averaged electric field intensity profile for a forward-running mode (from left to right) in a gamma-shape waveguide shown as inset for (b) the trivial and (d) non-trivial bands (marked with green and orange circles in (c), respectively). Unlike the trivial mode, robust propagation of light is observed for the non-trivial mode. Same lattice parameters as the ones in 1.10 are used in all cases.

Initial development in these types of topological interfaces recently have been reported both in theory and experiment [63].

Chapter 2

Methods

2.1 Overview

This chapter describes the methods utilised throughout the development of the topological nano-photonic devices presented in this thesis. The first section provides an introduction to InGaAs semiconductor quantum emitters, which are used as on-chip integrated light sources to probe the performance of nano-photonic devices. The second section describes the simulation techniques utilised to predict, optimise and understand the performance of the optical circuits both before and after fabrication. Finally, the last section reviews the steps involved in designing the photonic structures, followed by imaging analysis carried out on the fabricated devices during optimisation steps.

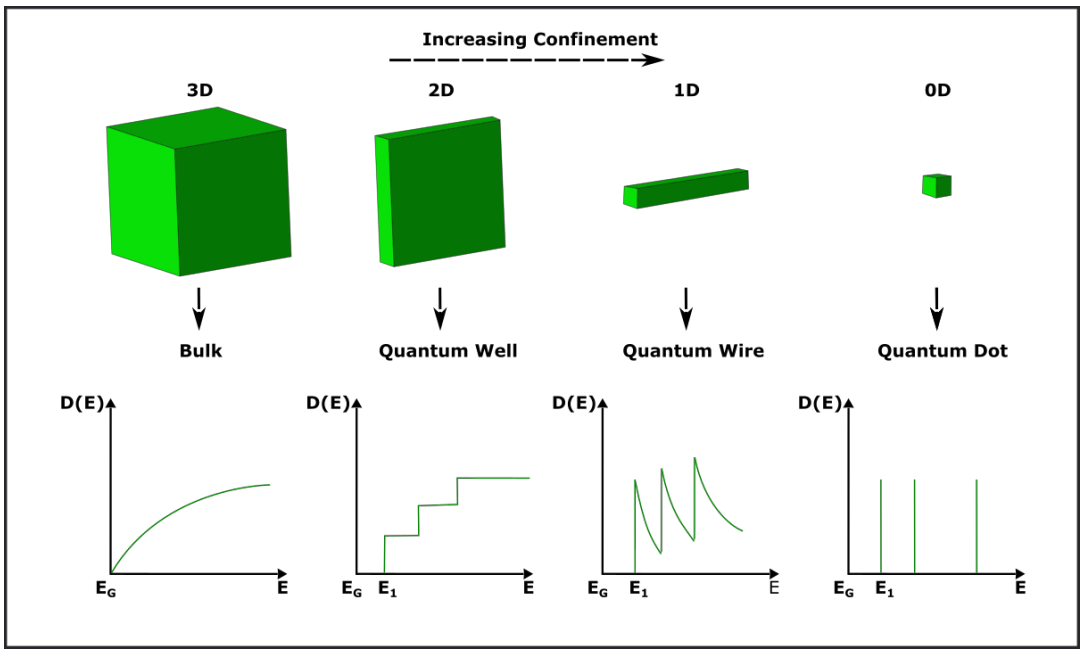

Figure 2.1: Evolution of the density of states (D(E)), as the number of confined dimensions increases from bulk material to quantum wells, wires and dots, respectively.

2.2 Semiconductor III-V Quantum Dots

Quantum Dots (QDs) are excellent candidates for integration in photonic circuits as embedded quantum emitters due to their many favourable properties, which includes atom-like discrete optical characteristics, highly efficient single-photon generation and electrical, optical and magnetic controllability. This section provides a brief overview of the formation, relevant optical and electrical characteristics and properties of Self-Assembled Quantum Dots (SAQDs), primarily focusing on semiconductor InAs QDs which were used in the devices discussed in this thesis. Additional information and supplementary details on these quantum emitters are provided in Appendix 1.

2.2.1 Electronic and Optical Properties of InAs Quantum Dots

Reducing the number of dimensions in a system can be utilised as a deterministic approach to achieve a higher degree of quantum-confined characteristics similar to that of atoms. For example, characteristics of 1, 2 and 3-dimensional potential wells can be observed in a quantum well, wire and dot, respectively. In particular, as the confining dimension decreases to less than the de Broglie wavelength (λ_D), quantum confined characteristics are observed. As the number of confined dimensions is increased, the change in confinement is characterised via the change in the density of states (D(E)), as shown in Figure 2.1.

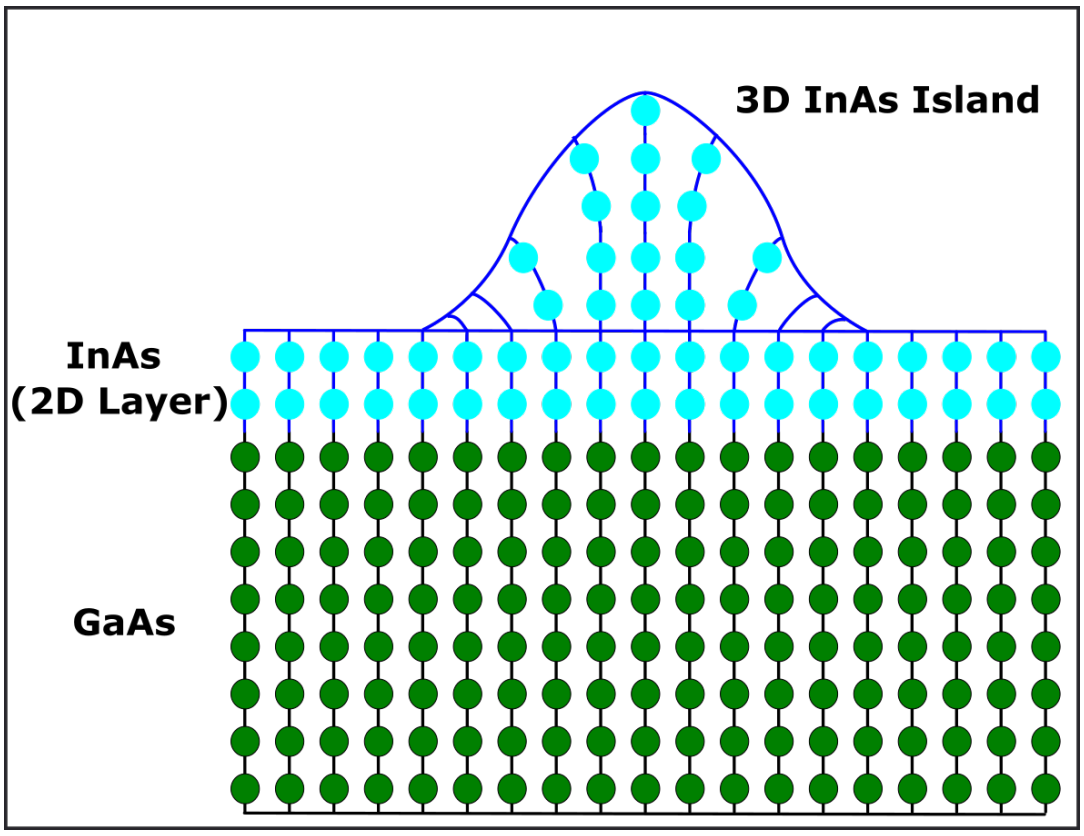

Figure 2.2: Schematic of an InAs/GaAs QD grown using the Stronski-Krastanov method.

In particular, discrete levels of energy are formed in a QD, in a configuration of separated narrow peaks in D(E). This is a very similar characteristic to the energy levels of atoms, and for this reason, QDs are called *atom-like* systems or artificial atoms, and like atoms, they support the required discrete energy levels for implementing a quantum bit (qubit).

QDs were observed initially in a glass matrix demonstrated in the 1980s [64]. Subsequently, numerous approaches have been used to form QDs, including epitaxial growth, droplet epitaxy and colloidal QDs [65]. In the epitaxial method, which is the method used for the growth of QDs used in this thesis, QDs can be grown with very high-quality optical properties such as very narrow linewidth [66], which make them promising candidates as single-photon sources with a high level of indistinguishability, a characteristic required for efficient quantum information processing.

In the Stronski-Krastanov (SK) epitaxial method, QDs are formed due to lattice mismatch between two different layer of thin materials, which is the substrate and the other one is the growth material (for example GaAs/InAs). The growth technique used for these types of QDs is usually Molecular Beam Epitaxy (MBE), in which, elements are condensed under a very high vacuum on a substrate to facilitate their reaction leading to the growth of crystalline layer. Strain builds

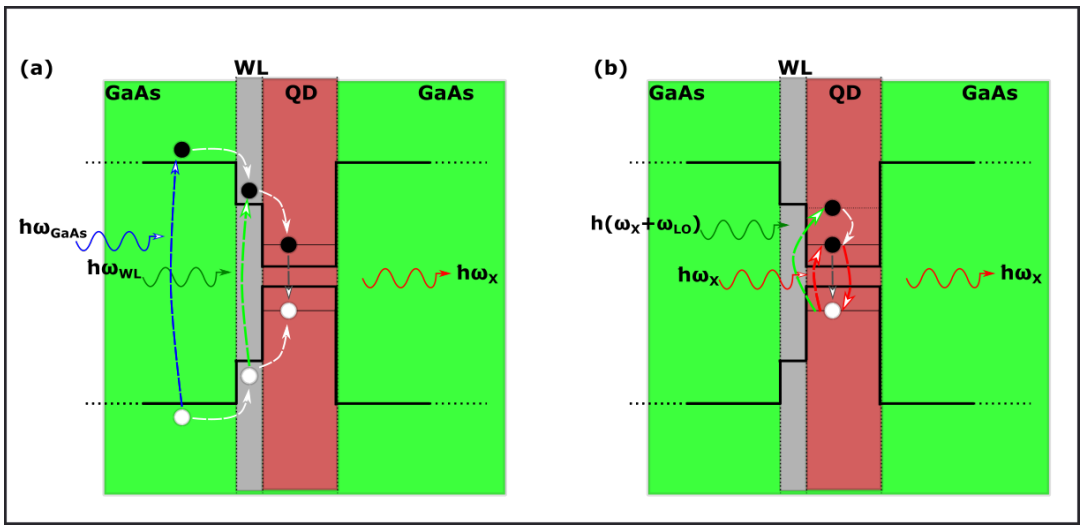

Figure 2.3: Photoluminescence schemes for a SAQD. (a) Above bandgap (non-resonant) and wetting layer excitations are shown in blue and green, respectively. (b) Red and green arrows show resonant and 1LO phonon excitation schemes, respectively. Non-radiative relaxation processes are shown with black arrows.

up within the growth layer due to the lattice mismatch. Then, a very thin 2D layer called the *Wetting Layer* [67] is grown which leads to further increase in the strain, due to which 3D islands of coherently strained material will form (since the formation of these 3D islands are energetically preferential compared to that of the 2D layers). QDs formed based on this mechanism are called SK QDs [68], for which a schematic is shown in Figure 2.2.

After the formation of these small islands, the dot layer then is buried by copping with GaAs. The 3D confinement is therefore achieved and QDs are formed. Due to the stochastic nature of this QD formation mechanism, these QDs are called self-assembled, for which there is a rich literature on formation details, on-chip integration and application [69].

The self-assembly nature of this QD growth technique leads to the existence of a range of sizes and, therefore, energies of the SAQDs. The growth conditions such as growth rate and temperature are usually used to control and modify both the transition energies as well as the distribution density of QDs. Lower QD density, greater uniformity in transition energy and narrower linewidth are particular features that are favourable for efficient and deterministic QIP.

The QDs formed using this method are formed at random positions. However, there are methods to address this, namely a pre-growth positioning technique called site-controlled growth, as well as a post-growth method called QD registration, for locating the QD positions after their formation [70, 71, 72]. Both of these methods can be used to deterministically position the QDs in desired locations in an optical circuit.

In SK QDs, electron-hole binding arises due to the Coulomb attraction between an electron promoted to the conduction band, and the resulting hole in the val-

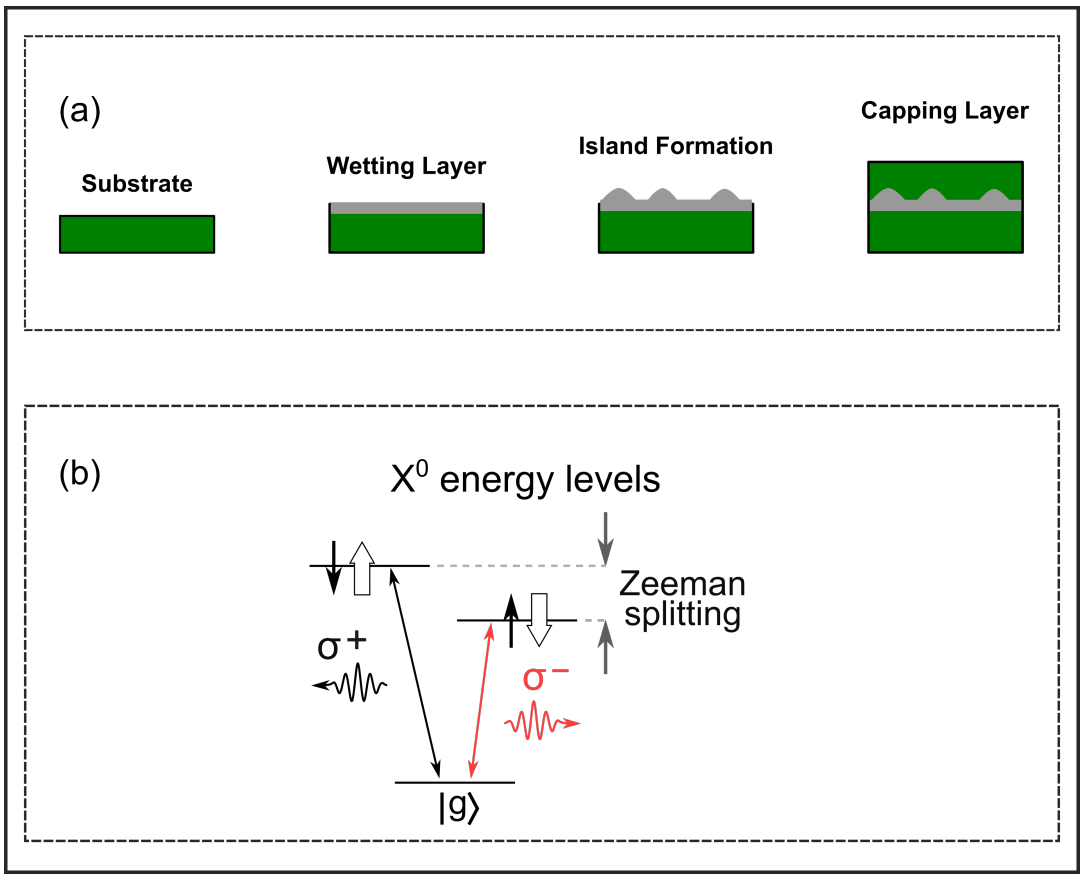

Figure 2.4: (a) Formation of InAs QDs (grey) capped between a substrate and a capping layer of GaAs (green). (b) Energy levels for the X_0 (neutral) exciton under an external non-zero magnetic field. Black and red arrows show the positively and negatively circularly polarisation transitions, respectively.

ance band. This quasi-particle, the bound electron-hole pair, is called an exciton (See Appendix 1).

Photoluminescence

Photoluminescence (PL) emission resulting from excitation of integrated QDs is used for on-chip generation of light in the nano-photonic structures presented in this thesis, primarily to probe the optical performance of topological photonic circuits down to the single-photon regime. Schemes for obtaining PL from a QD are illustrated in Figure 2.3.

Zeeman effect

Schematic of capped QDs grown using the SK method, as well schematic of the Zeeman-split transitions for a QD is shown in Figure 2.4. The excited state of a neutral exciton (X_0) in a QD can be split into two energetically resolved states due

to the Zeeman effect (charged exciton states also can be split similarly). While the (X_0) transition leads to the generation of photons with linear polarisations, the applied magnetic field splits the transition into two branches with opposite circular polarisations. The circularly polarised photons generated using this effect were intensively utilised to probe the directionality of edge states in a variety of nano-photonic device configurations presented in this thesis.

2.3 Simulation

To study, investigate and optimise the performance and optical characteristics of topological photonics devices, computational electromagnetic simulations were carried out before fabrication. These simulations provide a platform to study device parameters and facilitate an optimisation process to maximise the chance of successful fabrication. For this thesis, the finite-difference time-domain (FDTD) is used, based on the iterative solution of the time-dependant Maxwell equations. Using this method, temporal responses and field evolution within a variety of structure are studied. Subsequently, properties of photonic structures such as Q-factors of resonators and cavities resonant modes, transmission spectra and electric and magnetic field profiles of different structures were investigated. The software used for this purpose is the commercially available Lumerical FDTD solutions, which is an eigenmode solver and propagator simulation software used in photonics. In particular, for the work presented here, the intensive use of FDTD simulations significantly facilitated high-fidelity prediction and understanding of the behaviour of topological devices, as well as helping to set agendas for deterministic device applications via establishing more experimentally friendly designs for either new optical protocols or improving already existing approaches.

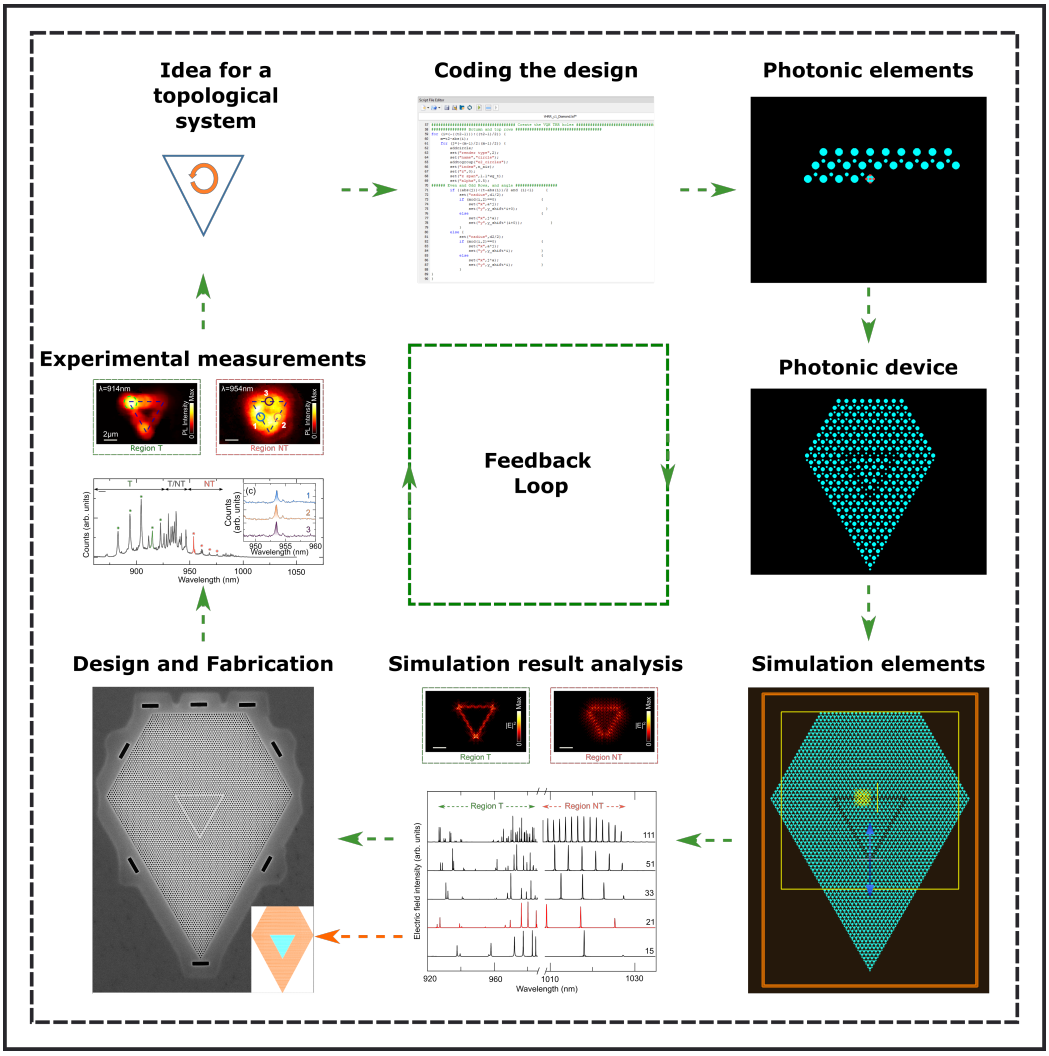

Figure 2.5: Feedback loop for developing topological photonic devices. A triangular-shaped QVH-type topological PhC ring resonator is considered here as an example. Starting from the top-left corner and moving counter-clockwise: a design for the ring is proposed. Then, FDTD scripts are developed to generate the PhC holes and other related structural elements for the device. This is followed then by adding electromagnetic monitors to record the spectral, temporal and field profiles of the fields within the structure. After running the simulation, information such as resonant spectrum and field profiles and Q factors are extracted. Simulations are repeated for a variety of device parameters such as hole sizes and device dimensions. Once a desired set of parameters are identified, Python scripts are developed for the design and fabrication of the structures. Devices are then fabricated and investigated experimentally using optical spectroscopy methods, the results of which are compared to simulations and then the findings are fed into the first step again to address the challenges and improve the design. The loop is then repeated until desired performance and properties are demonstrated.

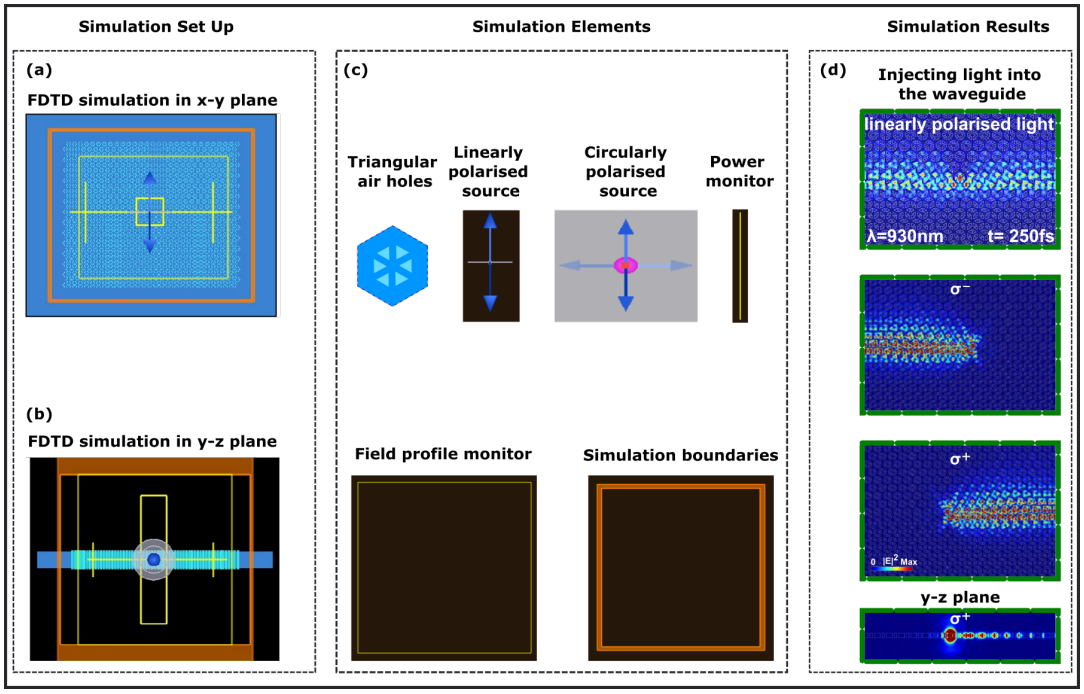

Figure 2.6: (a) an FDTD simulation set-up viewed from x-y plane (from above the membrane). (b) Same simulation viewed from y-z plane, showing the suspended semiconductor membrane. (c) Simulation objects. (d) From top to bottom: emitted light from an embedded dipole propagating along the waveguide for linear as well as circularly polarised light. The bottom panel shows the circularly polarised case viewed from y-z plane, showing 2D confinement due to total internal reflection for the propagating light.

2.3.1 Iterative process for photonic device design

The two main advantageous properties of topological photonic edge states, which is their intrinsic unidirectionality and robustness against back-scattering and (some) disorder, paves the way for the design of novel photonic devices with appealing properties. During the development of photonic devices discussed in this thesis, an iterative feedback process was used. As an example, Figure 2.5 shows the general steps in such a loop which was repeatedly used for a variety of structures, shown here for a topological photonic ring resonator.

The first step in this feedback loop, starting from the top left corner, is conceiving an idea for a photonic device that can benefit from topological properties of edge states. Such an idea encapsulates the unidirectionality as well as the robustness of the edge states to form a closed optical circuit that could be used as an important element in integrated optical waveguides and filters. Since the propagation of light around sharp corners is protected for a topological edge state, this characteristic is utilised and a triangular ring resonator is proposed using one of the QVH interfaces discussed in chapter 1. Then, scripts are developed to generate the photonic elements such as air holes and semiconductor slabs (and, when

needed, nano-beams, out-of-plane couplers, etc) for such a structure, in order to define the refractive indexes of the structures. This is followed by adding simulation elements such as light sources, transmission and field profile monitors and periodic simulation boundaries. Simulations are carried out for an appropriate time and then field profiles, spectral information, transmission bandwidth and resonant mode Q-factors are extracted; this is repeated for a variety of parameters such as ring resonator sizes, hole sizes, lattice constant, device dimensions, etc. Optimised parameters are then extracted, and after taking into account fabrication considerations (discussed in the next section), a series of devices are designed and fabricated. Extensive quantum optical experiments are carried out on these devices. The results are used to better understand the performance of the structure in reality and to assess potential optimisation. This may include crucial information which is fed into the improved versions of the original design, or sometimes, if needed, a major upgrade or proposed structure.

This iterative process was frequently used for a series of different novel photonic topological devices such as waveguides, ring resonators, cavity-coupled waveguides and PhC filters, for which the FDTD simulations played a significant role in particular in maximising the success rate of the device design process and fabrication.

For better familiarization of the types of simulations carried out in studying these devices, an example of a simulation set-up for a basic QSH interface waveguide and its elements is discussed here. The QSH interface is formed from shrunken and expanded PhCs (see Chapter 1), supporting two edge states with opposite group velocities. In this particular case, the aim is to study how the light emitting from a dipole can couple to the topological edge states of the PhC waveguide. The 3D simulation set-up viewed from a point in z-direction (above the structure) for such a simulation is shown in Figure 2.6 a. The structure consists of triangular air holes arranged in a hexagonal unit cell to form a honeycomb lattice within a semiconductor membrane periodic boundaries. Simulation objects/elements are placed around the structure. As an example, an electric dipole acting as a light source, is placed at the interface within the PhC, and transmission and field profile monitors are placed around it to monitor the spectral and spatial distribution of light after a specific simulation time. Time-averaged electric field intensity profiles extracted from the monitors (see Figure 2.6 d) show that the light from the dipole couples to the QSH edge states of this honeycomb interface and propagate along with interface in the x-direction. A linearly polarised light excites both edge states, propagating in both left and right directions, while circularly polarised light demonstrate unidirectional behaviour: light with orthogonal polarisation propagates in opposite directions. A snapshot from the y-z plane shows that the propagating light is confined in the x-y plane due to total internal reflection.

In addition to field profile information, the temporal evolution of electromagnetic fields is informative for the behaviour of light in these photonic structures. For example, as discussed in chapter 1, photonic bandgaps can be opened in a

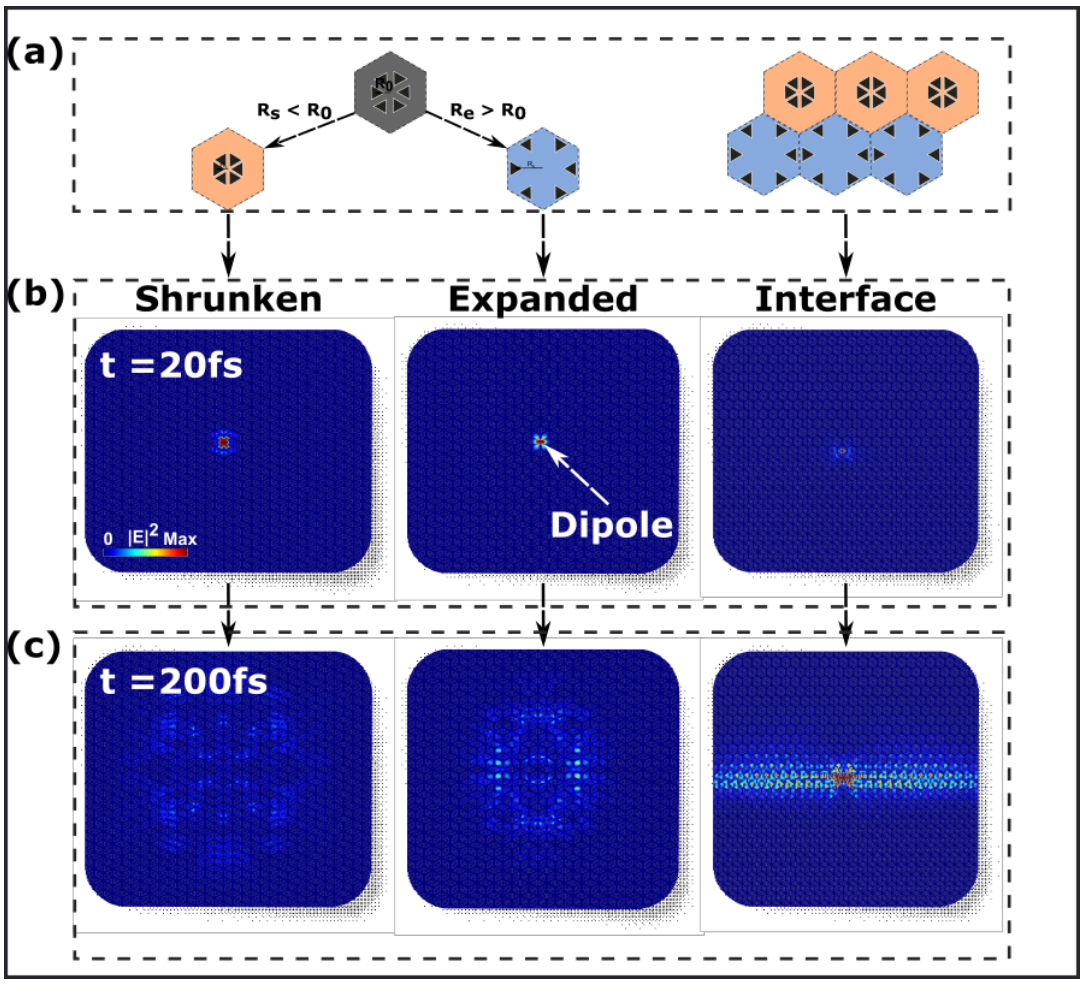

Figure 2.7: Temporal evolution of light emitted from a linearly polarised embedded dipole into a (left) shrunken PhC, (middle) expanded PhC and (right) an interface between the two. After 200fs, light dissipates in the case of perturbed PhC with band gaps, while it propagates at the interface between the two, which supports QSH edge states.

honeycomb PhC via expanding and shrinking the hexagonal unit cell, and when interfaced, edge states can be formed to guide the light at the boundaries. To investigate this via FDTD simulations, as shown in Figure 2.7, a dipole is embedded in three different honeycomb photonic crystals (two with bandgaps, and one which is the interface between the two, supporting guided QSH edge states). By investigating the time evolution of emission at early and late stages of the simulations, it can be seen that the emitted light from an embedded dipole in the PhC dissipates for the shrunken and expanded lattices which have a photonic bandgap, while for the interface case, the light from the dipole couples to the edge states and propagates along the interface direction.

Another FDTD technique widely used in this thesis is to study the behaviour of light in topological optical ring resonators. For example, monitoring the rate

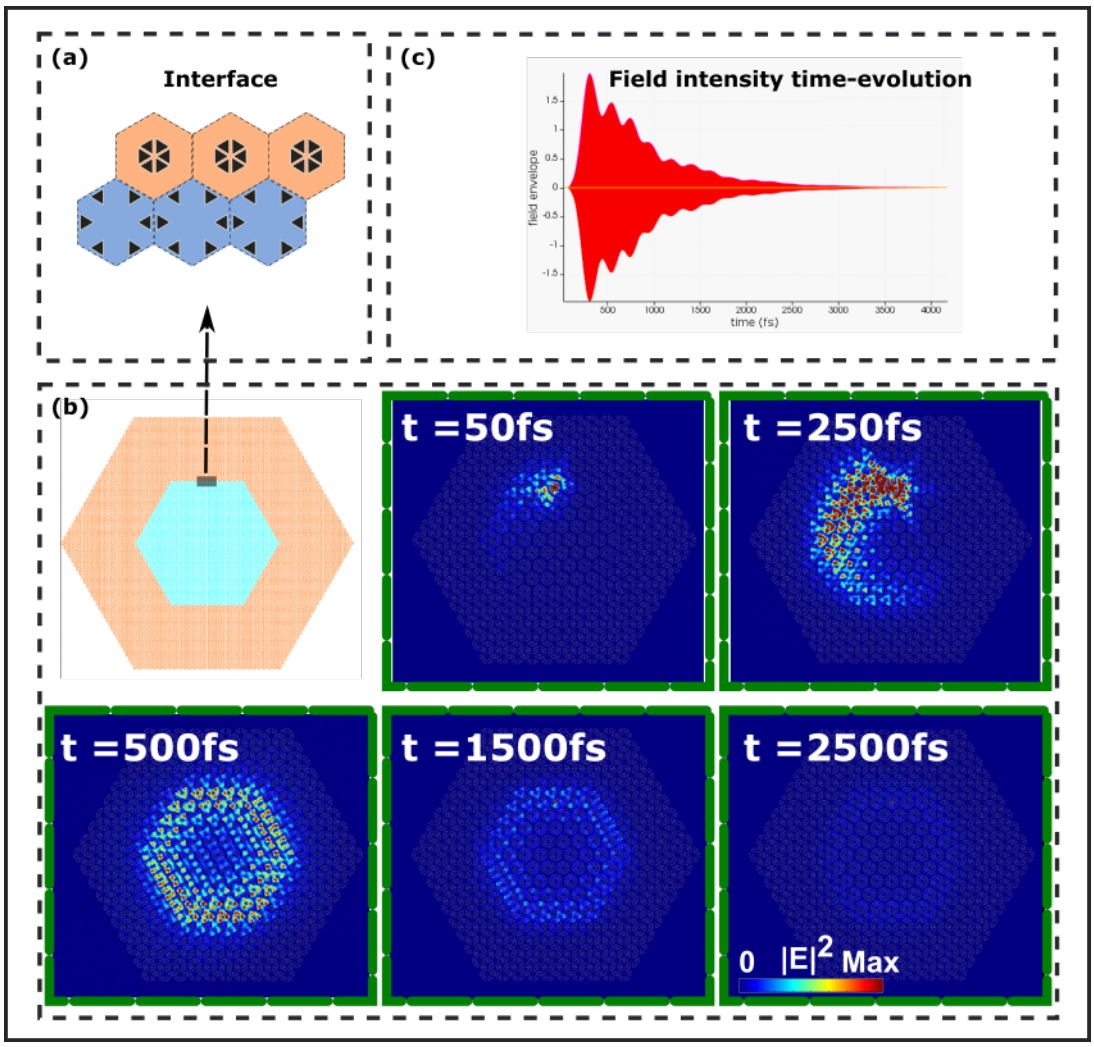

Figure 2.8: (a) The QSH interface used to form a hexagonal PhC ring resonator. The interface supports two chiral edge states, and light from a broadband emitter can propagate unidirectionally around the ring without scattering at the sharp corners due to topological protection. (b) Time evolution and decay of light emitted from an embedded dipole into the ring resonator. (c) Decay of the field intensity vs simulation time.

at which the field intensity of a resonant mode decays gives information about the lifetime and the Q factor of the mode. To study this, as shown in Figure 2.8, light from a circularly polarised light source is injected in a hexagonal-shape PhC ring resonator using a QSH interface. The evolution of the field profile of a resonant mode confined at the interface region, as well as temporal evolution of the resonant mode at different time intervals is shown. It can be seen how and with what rate the resonant mode of the ring decays.

The FDTD method was intensively used to design, optimise and study the control of the flow of light in topological PhC devices with increasing complexity

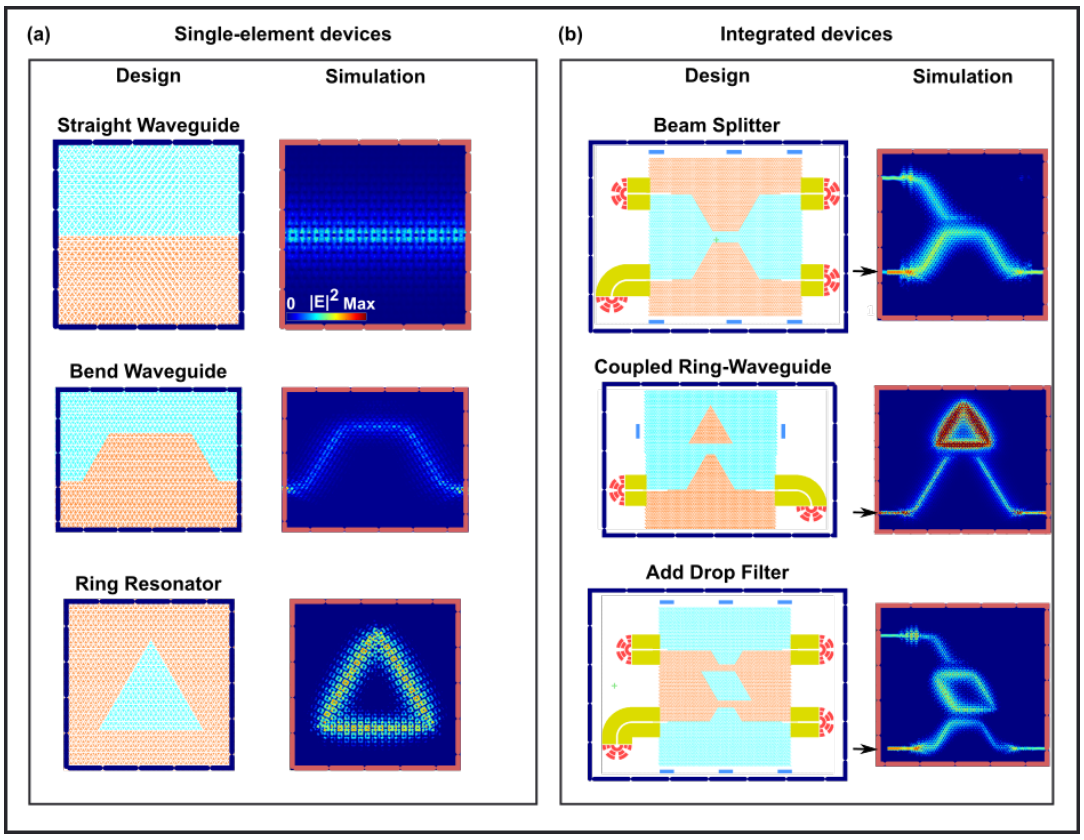

Figure 2.9: Design and FDTD simulation of topological photonic devices with increasing complexity and functionality. Design (left) and FDTD simulated time-averaged electric field intensity profile (right) for the edge state in (a) single-element and (b) integrated topological photonic devices. In the straight and bend waveguides, the light is injected into the device from the left-hand side, while the light in the resonator comes from an embedded dipole source at the interface. For devices in (b), in all cases, the light is injected through the bottom-left port of the device.

and functionality. A few examples of these devices are shown in Figure 2.9. In each case, the design of the structure, as well as the field profile of the excited edge state is shown at the interface of a QVH system. The left column shows simpler, single-element devices, where there is only one QVH PhC interface used to control the flow of photons, starting from (top) a straight waveguide to (middle) a waveguide with four sharp bends and then (bottom) a triangular shape ring resonator. Each one of these devices can serve as an element in an optical circuit, or be used to build more complicated multi-functional devices. For example, as shown in right hand side, two bent waveguides (top) are brought close to each other in parallel, so that input light from one of the ports, when travelling through one of the waveguides, evanescently couples into the other waveguide to form an on-chip beam splitter that can separate a desired fraction of input light and send it to a different port. In the next device (right column, middle row) a ring

resonator is coupled to a bent bus waveguide, where the strength of evanescent coupling of the ring modes into the bus waveguide can be controlled using the design parameters such as the ring-waveguide separation distance. Finally, a four-sided ring resonator (bottom right corner) is coupled to two bent bus waveguides at the bottom and top to form a topological add-drop filter. In this device, some fractions of a broadband input injected into one port is filtered by the resonator and redirected to a different port. A detailed study of features, optimisation and experimental performance of some of these devices will be discussed in the following chapters.

In high precision simulation of these 3D devices, some of which are large-scale, complex structures, the University of Sheffield's High Performing Computer clusters (ICEBERG and SHARC) were used. Some simulations took multiple weeks to finish, and at times, up to several thousands of GBs of RAM were utilised for the simulation of larger 3D structures. The FDTD simulations proved crucially important both as a preparation and design optimisation step before the fabrication, as well as a powerful tool to understand the behaviour observed later in fabricated structures.

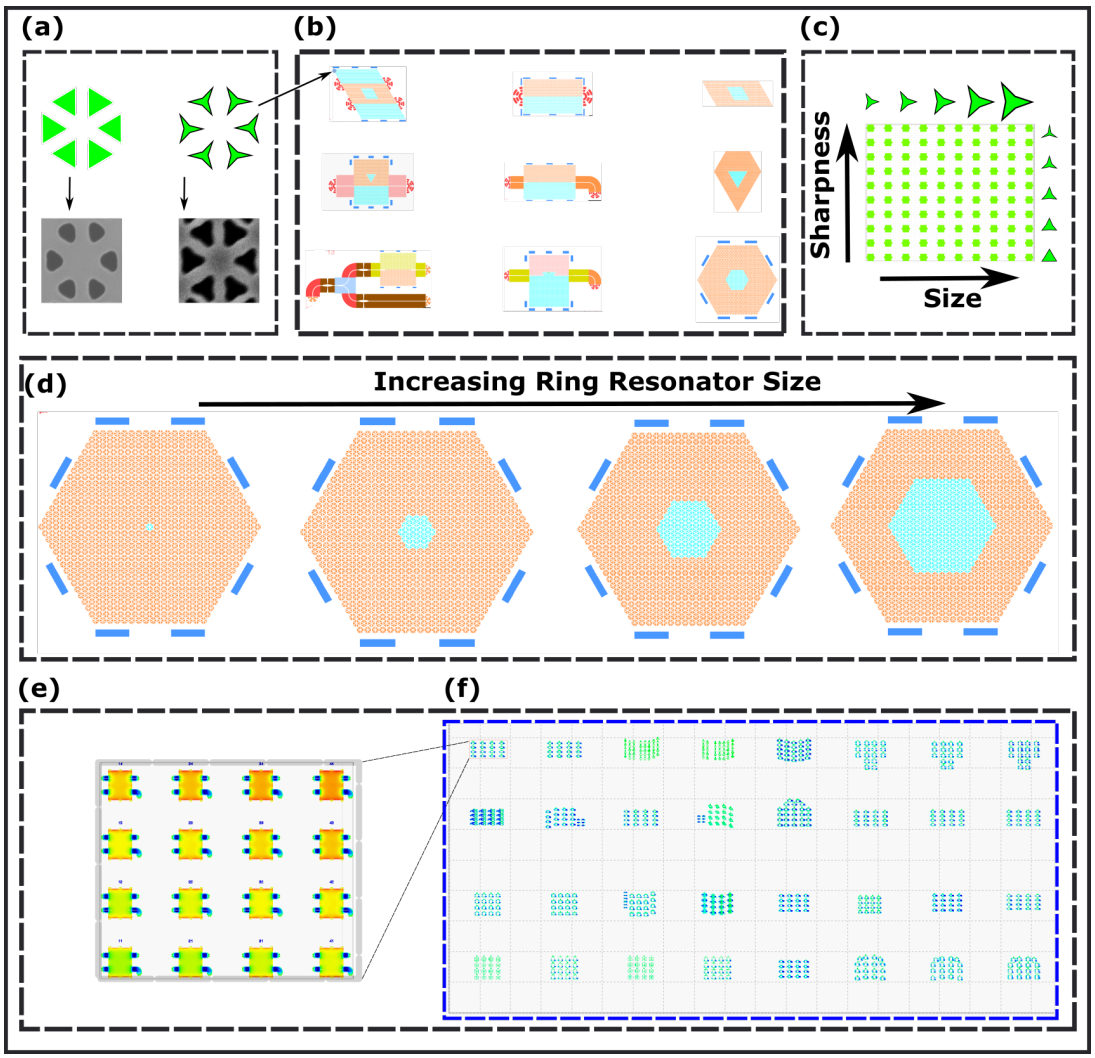

Figure 2.10: Steps in designing a photonic chip. (a) Designing and modifying the unit cell (here, for example, to achieve sharper triangles, the design was modified, the detail of which will be discussed later in this section) of a topological lattice. (b) Developing PhC interfaces for different applications and in different device configurations. (c,d) Generating a matrix of devices with varying parameters such as (c) hole size and shape modification (d) device dimensions. (e) Proximity correction of the design matrix and (f) assembling all of the matrices for fabrication on the same semiconductor sample.

2.4 Design and Fabrication

This section provides information on the design process as well as fabrication optimisation of the topological PhC devices. A variety of devices with different functionalities were designed and optimised at different stages for the work presented in this thesis, for which semi-automated Python scripts were developed to speed up the process of designing samples with numerous devices with varying

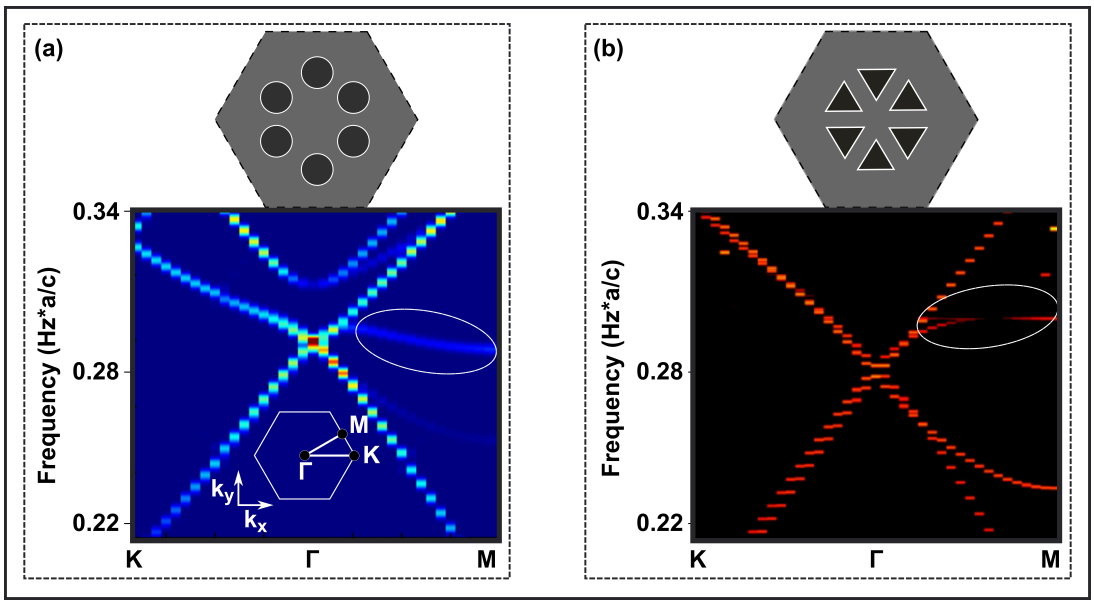

Figure 2.11: (a) band structure of a hexagonal unit cell comprising 6 same-size circles. Valence and conduction bands are degenerate at the Dirac point. However, as marked with an ellipse, there is a bulk conduction band bending towards the Dirac point frequency causing multi-mode scattering issues at the Dirac frequency, which is detrimental to the PhC performance. High symmetry points of the first BZ of the lattice is shown in the inset. (b) Same hexagonal unit cell with instead triangular holes. The marked band is lifted upwards and away from the Dirac frequency, paving the way for the opening of a clear, full band gap.

parameters. Steps involved in the design of the photonic structures will be discussed, followed by fabrication results and Scanning Electron Microscopy (SEM) imaging analysis of the nano-photonic topological devices.

2.4.1 Design

After conceiving the idea, using FDTD simulations to optimise the photonic devices parameters, the next step is to design each device for nano-fabrication.

The first step of the design process of a PhC structure is the development of the repeating unit cell of the crystal. For example, the hexagonal unit cell of a QSH honeycomb PhC which consists of six equilateral triangular holes can be used to form QSH topological waveguides and resonators. To do this, Python scripts are developed to write the coordinates of the six triangles for such unit cell in an ASCII file, which later can be read by Raith Voyager GDS software to create the structure. An example of such a unit cell is shown in Figure 2.10 a. Before proceeding to make a periodic photonic crystal using this unit cell, fabrication considerations are taken into account. For example, the first fabrication tests revealed that if simple triangular shapes are designed, the fabricated aper-

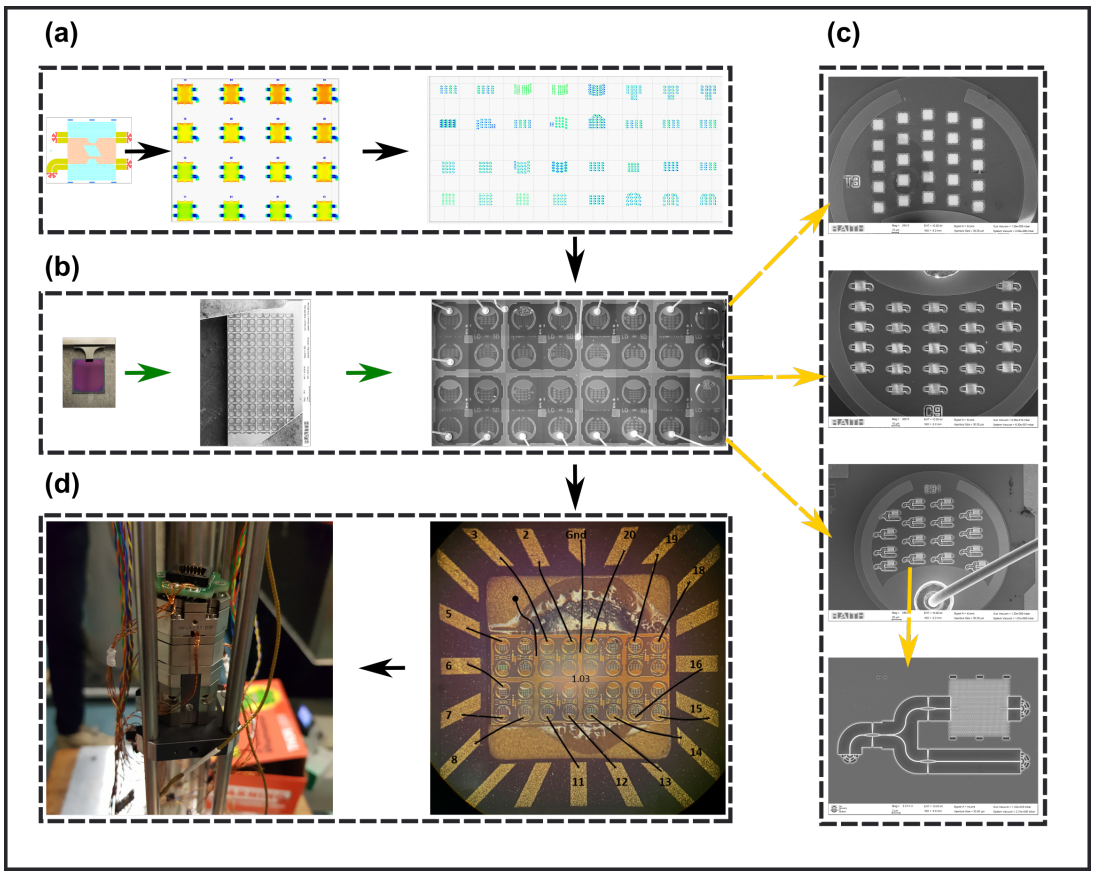

Figure 2.12: Fabrication steps in designing one of the topological photonic samples. (a) Design, proximity correction and assembling of the matrices of devices. (b) (left) A scribed piece of the semiconductor wafer (GaAs membrane with embedded InAs SAQDs). (Middle) fabrication of diode mesas which allow for electrical control of QDs. (Right) The fabricated sample after multiple dry and wet etching processes and bonding of the diodes. (c) SEM imaging analysis of the different matrices and devices. (d) Sample on a chip mount (right) and then installed on an x-y-z stage (left) for insertion in a bath cryostat.

tures will come out rounded especially at their corners. This is most probably due to the Gaussian shape of the electron beam used to make the holes during the fabrication. This difference can be detrimental to the desired photonic band structures of the PhC. By causing the dispersion of one of the bulk bands to move inwards towards the frequency of the Dirac point, and preventing the possibility of opening a full bandgap which is essential for the formation of scatter-free topological edge states (as shown in Figure 2.11). A modification is therefore considered here,which the sides of the triangles are moved inwards in the designed triangle, which as can be seen in the SEM images in (a), leads to triangles with sharper corners. Such correction and similar fabrication considerations were frequently utilised from SEMs taken from fabricated devices, using the information to further improve the design.

The design process is then followed by periodically drawing the unit cell (and adding the coordinates of each one to the ASCII file) in the desired configuration to form a variety of devices as shown in Figure 2.10 b. Photonic elements such as output couplers (to collect/inject light into the plane of the device), tapered nano-beams (to convert from PhC modes to nanobeam modes and vice versa), supporting struts (to prevent the suspended structures from collapsing/bending) and rectangular trenches (to facilitate under-etching of the devices during the wet-etch step) are added to each device. Then, for each device, a matrix is formed with varying parameters in x and y direction of the matrix. The range of these variables is chosen based on the FDTD simulation optimisations. For example, in Figure 2.10 c, triangle hole size and corner sharpness are varied in the x and y direction of the matrix, respectively. A further variation of the parameters is also included where necessary, such as the case shown in Figure 2.10 d where the size of a ring resonator is varied to study different free spectral range configurations. Once the matrices of devices are generated, they must be proximity corrected to achieve high quality fabrication during the Electron Beam Lithography (EBL), as shown in Figure 2.10 e. Proximity correction for fabrication of small nano-features can be very helpful since it addresses the Gaussian shape of the E-beam gun used to create the features, and ensures better uniformity and shape for the fabricated nano-features. Finally, these matrices of different devices are assembled to be fabricated all on the same chip.

The design and fabrication steps prior to optical measurements are shown in Figure 2.12. Once devices are designed and assembled in a matrix (a), standard nanofabrication methods are used to fabricate the structures. A GaAs membrane with a typical thickness of 170nm and containing a layer of embedded InAs QDs is used. A piece of the wafer is scribed, SiO_2 hard mask is deposited and electron-beam resist is coated on the top (b), and then mesas made using standard lithography are deposited for electrical control over the chip. Then, EBL is used to transfer and write the designs on the E-beam resist spin-coated sample. Dry RIE (for etching through the hard mask), and ICP (for etching through the 170nm GaAs into the sacrificial layer under the membrane) etching steps are used to vertically etch the holes and other photonics elements. The remaining E-beam resist is removed using Xylene. HF wet etch methods are then used to remove the hard mask and to under etch (removing the sacrificial layer) the structures to form suspended devices. Under etching creates a membrane with air/vacuum above and below, allowing for total internal reflection. The sample is then mounted on a ceramic chip carrier with electrical contact pads. Gold wires are bonded from the pads to each diode, the result of which is shown in Figure 2.12 d. Before this stage, intensive SEM imaging analysis is performed to investigate the quality and uniformity of devices and photonic crystals. If satisfactory fabrication quality is achieved, the sample is then transferred to the lab and mounted in a helium exchange gas for cryogenic optical measurements.

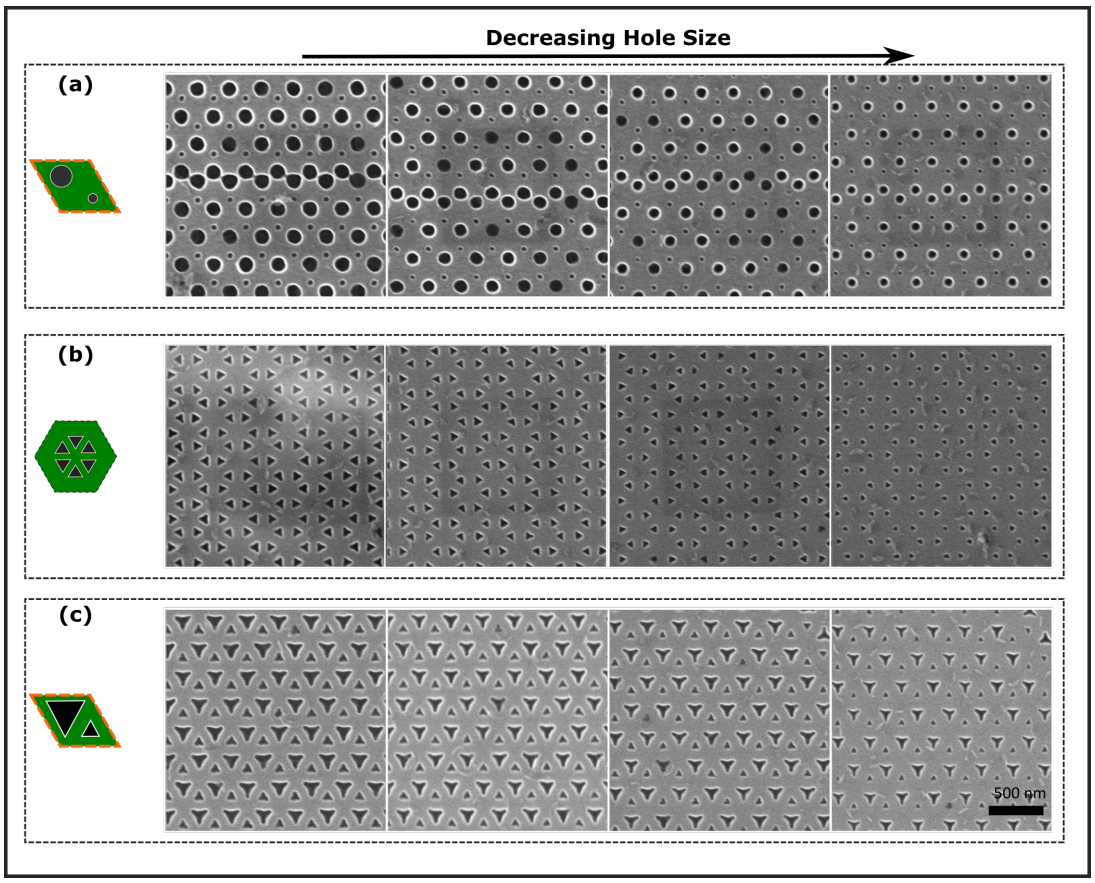

Figure 2.13: SEM images of hole size optimisation via changing the hole size parameter in the design for a QVH PhC with (a) circulars and (c) triangular apertures, and (b) QSH PhC with triangular apertures.

2.4.2 SEM analysis and fabrication optimisation

The importance of high-quality fabrication of uniform and precise features cannot be overstated when considering the performance of nano-photonic structures. This is especially true when the devices under study contain features with dimensions down to a few 10s of nanometres. Significant efforts were dedicated to investigate the fabricated structures via SEM analysis, from which information was extracted to improve the quality of the features in the next fabrication iteration. The main steps of the standard nano-fabrication process (in particular EBL, dry and wet etch steps, as well as bonding and sample cleaning and mounting) for the devices studied in this thesis were undertaken by Dr. Rene Dost. Training on most of these steps proved important to develop insights into designing progressively more fabrication-friendly structures. However, the work for this thesis was primarily focused on the design step as well as SEM imaging analysis of structure during/post-fabrication. Needless to say, these analyses shed crucial light on the behaviour of fabricated topological devices and identifying improvements required to overcome some of the challenges faced in the early stages of

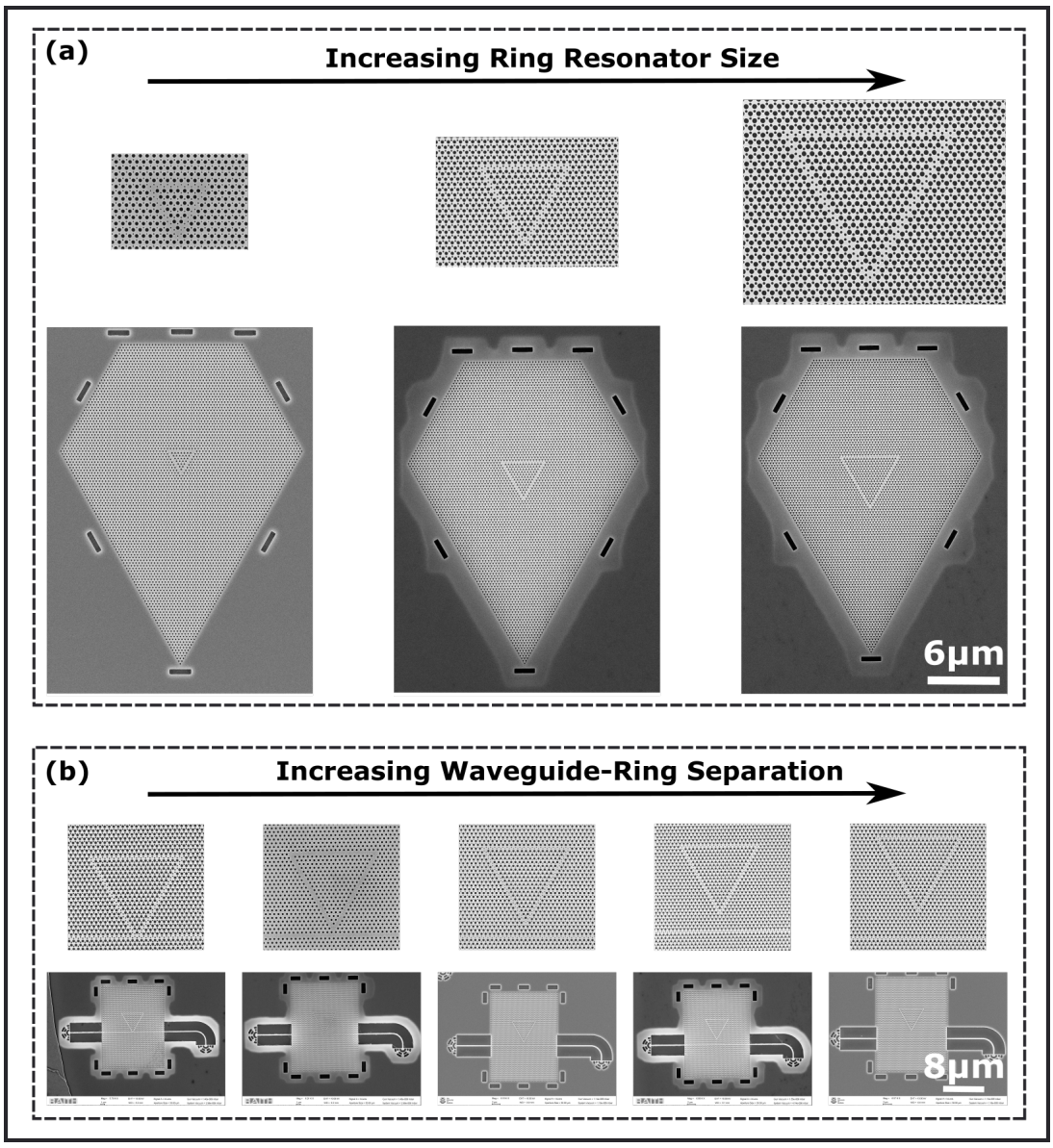

Figure 2.14: (a) Variation of a QVH PhC ring resonator size. (b) Variation of the ring-WG separation for controlling of the coupling strength between the two.

development. A summary of some of the important steps of the analysis and optimisations are discussed in this section.

Naturally, in a PhC, lattice constant and hole size plays a significant role in the band structure configuration and photonic behaviour of a device, in particular in determining the frequency bandwidth of the photonic bandgap of the lattices. By varying the hole size parameters in the design of the topological PhC, and subsequent SEM imaging, desired values for the PhC can be identified for holes at small scales. As an example, SEM images of hole size variation of three topological PhCs are shown in Figure 2.13. Hole sizes in a QVH lattice with circular (a) and triangular holes (c), as well as triangular holes in a QSH lattice (b) are varied from

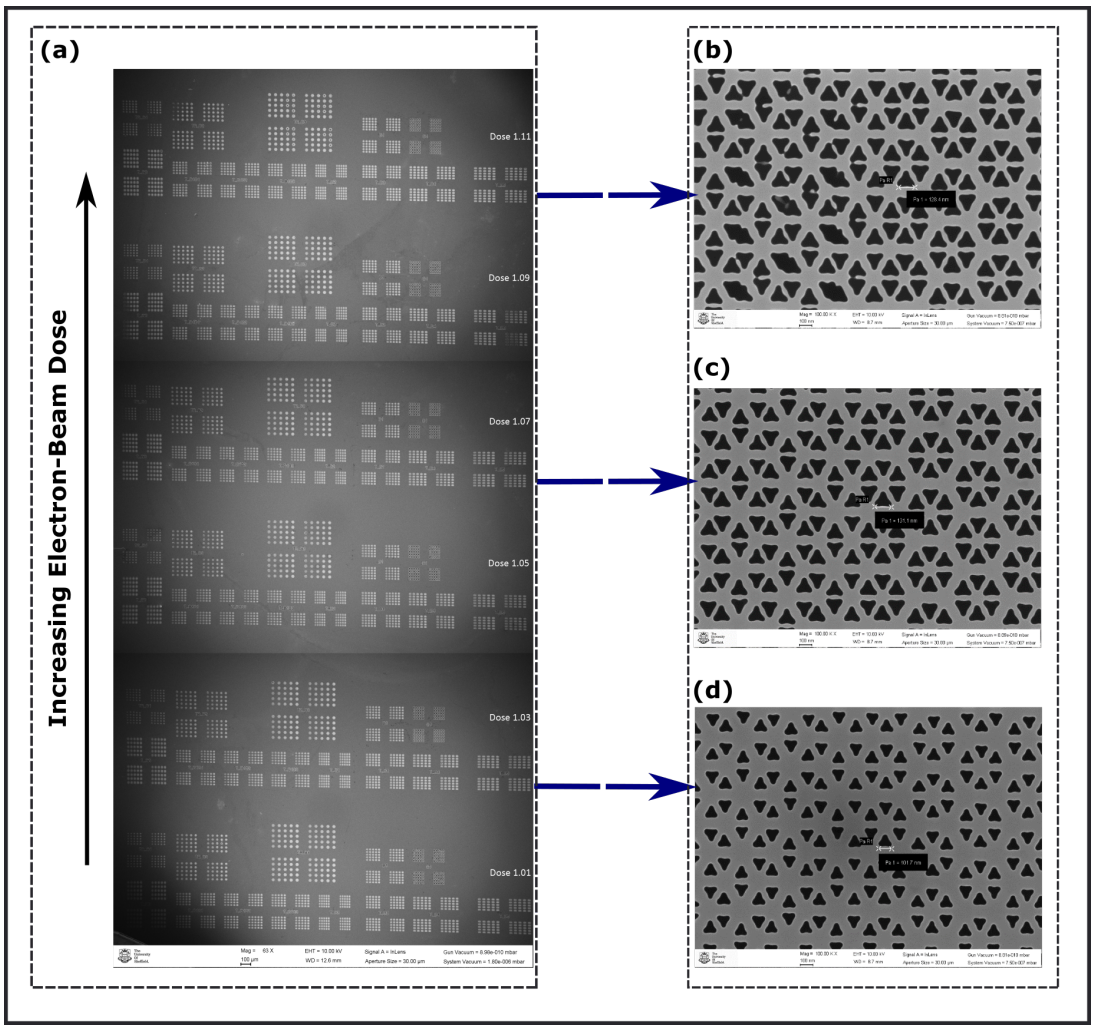

Figure 2.15: (a) From bottom to top: a series of copies of a same photonic chip with increasing EBL E-beam base dose. (b-d) Higher magnification SEM image of an identical design with a (b) high, (c) medium and (d) low base dose, showing a direct correlation between the applied base dose and PhC hole size.

larger to smaller hole sizes (from left to right), to identify desired values. This was achieved by varying the hole size parameters in the design process. Changing the hole size in PhC varies the effective refractive index, resulting in a shifting of the photonic bandgap, and, as a result, the bandwidth operation of the edge states. These were primarily aimed to operate at 900-1000nm, compatible with the InAs QDs used.

An important design parameter in the PhC ring resonator is the optical length of the ring, which dictates the free spectral range (spacing between resonant modes) as well as mode Q-factors (discussed in detail in Chapter 3). In Figure 2.14 (a), the size of a Valley-Hall PhC ring resonator is varied to study the experimental effect of this variation. Once a desired value for the ring size is achieved, the ring resonator is integrated with a bus waveguide for evanescent

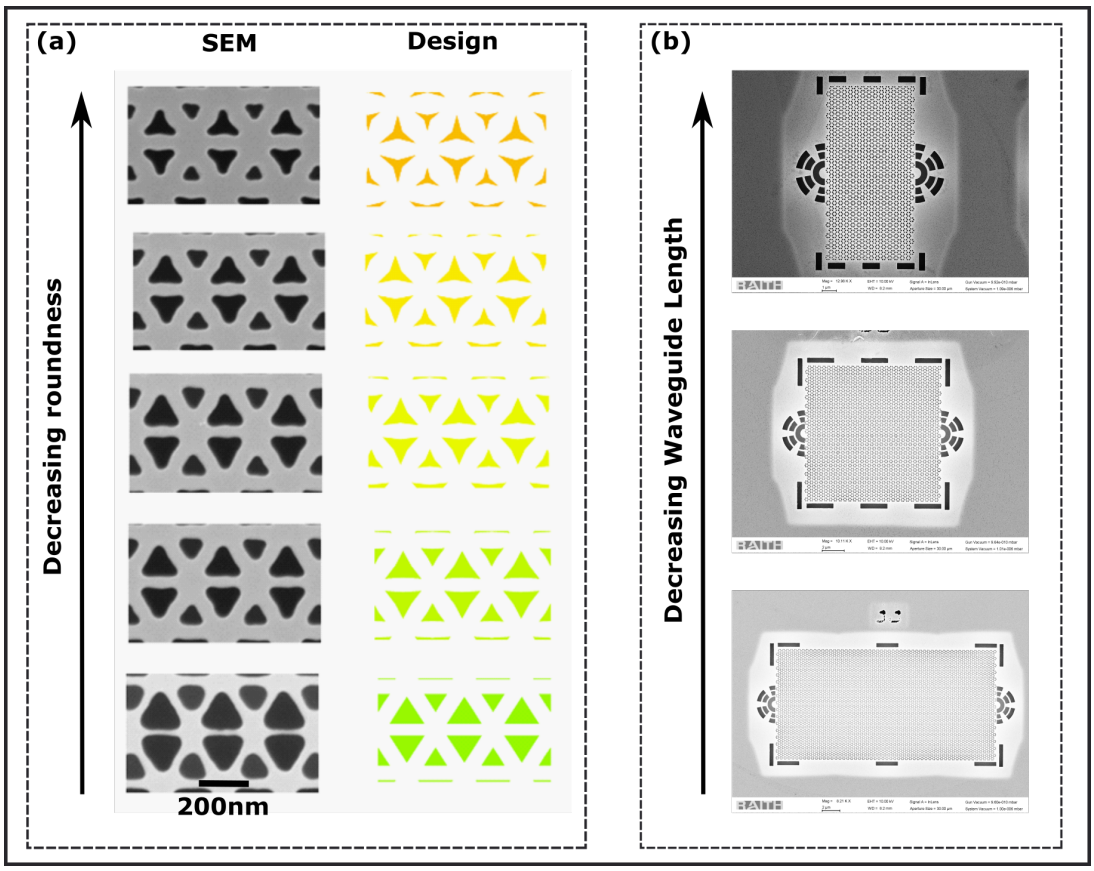

Figure 2.16: (a) (right) Modifying the triangle hole design by increasingly bending the triangle sides inward achieves sharper triangle holes, as shown in SEM images (left). (b) WGs with different waveguide length.

coupling of the ring modes to a waveguide for off-chip collection. By incrementally increasing the ring-WG separation, desired values for different coupling strength conditions between the two can be achieved.

Changing the hole sizes in the design is not the only way to vary the fabricated hole sizes. By applying a base-dose multiplier factor to the E-beam dose used in the EBL process, PhC holes with different sizes can be achieved. It should be noted that the shape of the holes also might be modified here as well. Therefore, for a designed chip, a series of copies with different base doses were fabricated and SEM images were taken and analysed to select the PhC with the desired shapes and sizes. As an example, one of the designed samples is shown in Figure 2.15, where (a) shows a series of copies of the chip fabricated on the same GaAs wafer, with increasing EBL E-beam based dose from bottom to top. On the right-hand side, zoomed images of the same section of a PhC is shown from different doses. (b) shows the case where the base dose was too high and the triangles came out too large, with adjacent holes starting to merge, while in (c) and (d) the holes are separate, (d) shows a smaller hole size on average when compared to (c), which

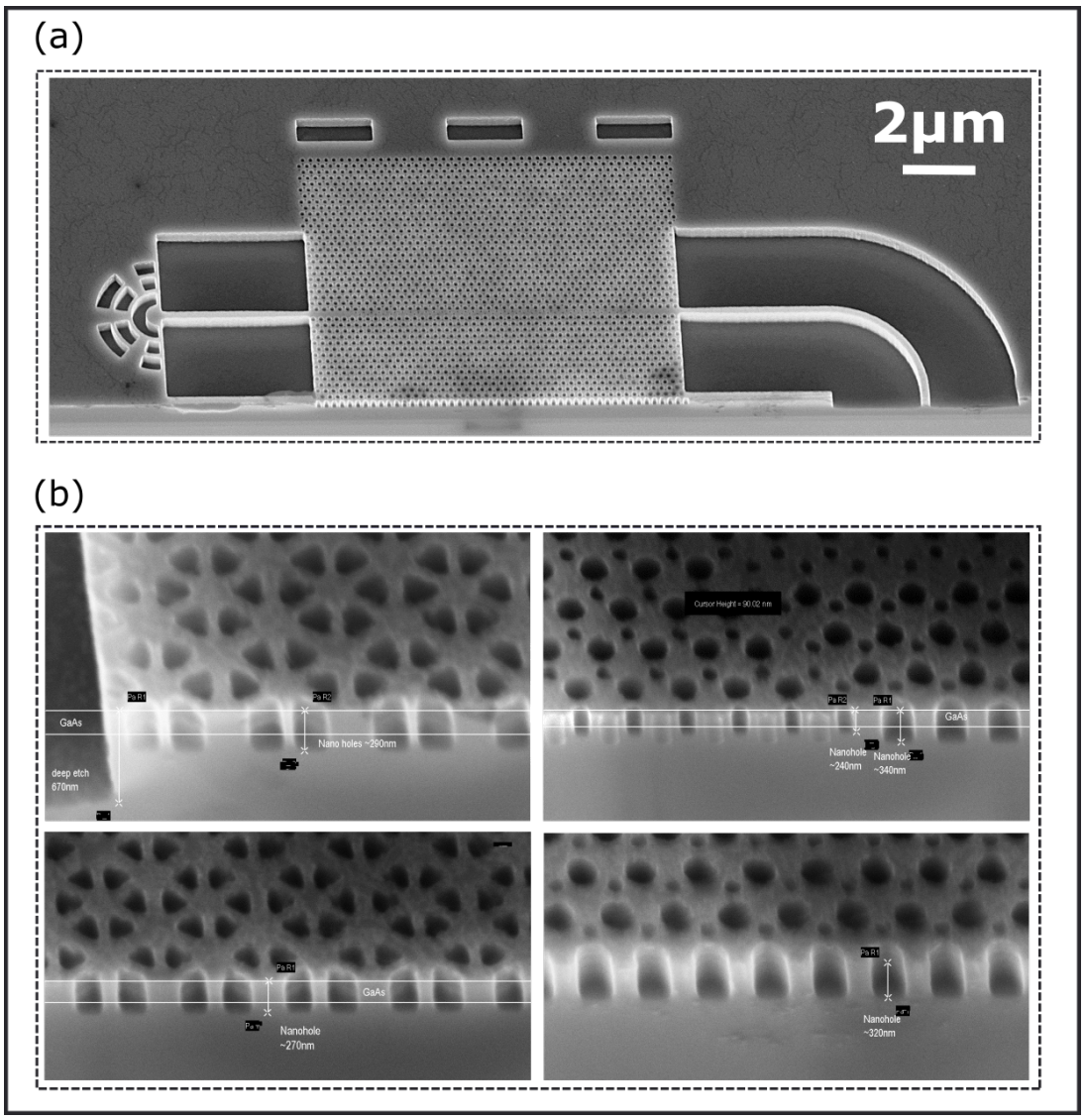

Figure 2.17: (a) A scribed PhC waveguide. (b) Side-view of (left) a QSH and (right) a QVH PhC with different hole sizes. This analysis makes sure that the etch depth was deeper than the 170nm GaAs membrane thickness (marked by two parallel white lines in (b).

shows how lower base dose results in the fabrication of smaller air holes from the same designed PhC.

As discussed in the previous section, triangles with rounded corners can be detrimental in achieving desired photonic properties of some of the topological PhCs. An optimisation was performed to control the sharpness of the triangular holes. As shown in Figure 2.16 a, the sides of the triangles in the design (right) are increasingly bent inwards (towards up). SEM images showed that sharper triangles could be achieved. Once the desired sharpness and hole size are achieved, WGs with different sizes were also designed to tailor for desired waveguide length

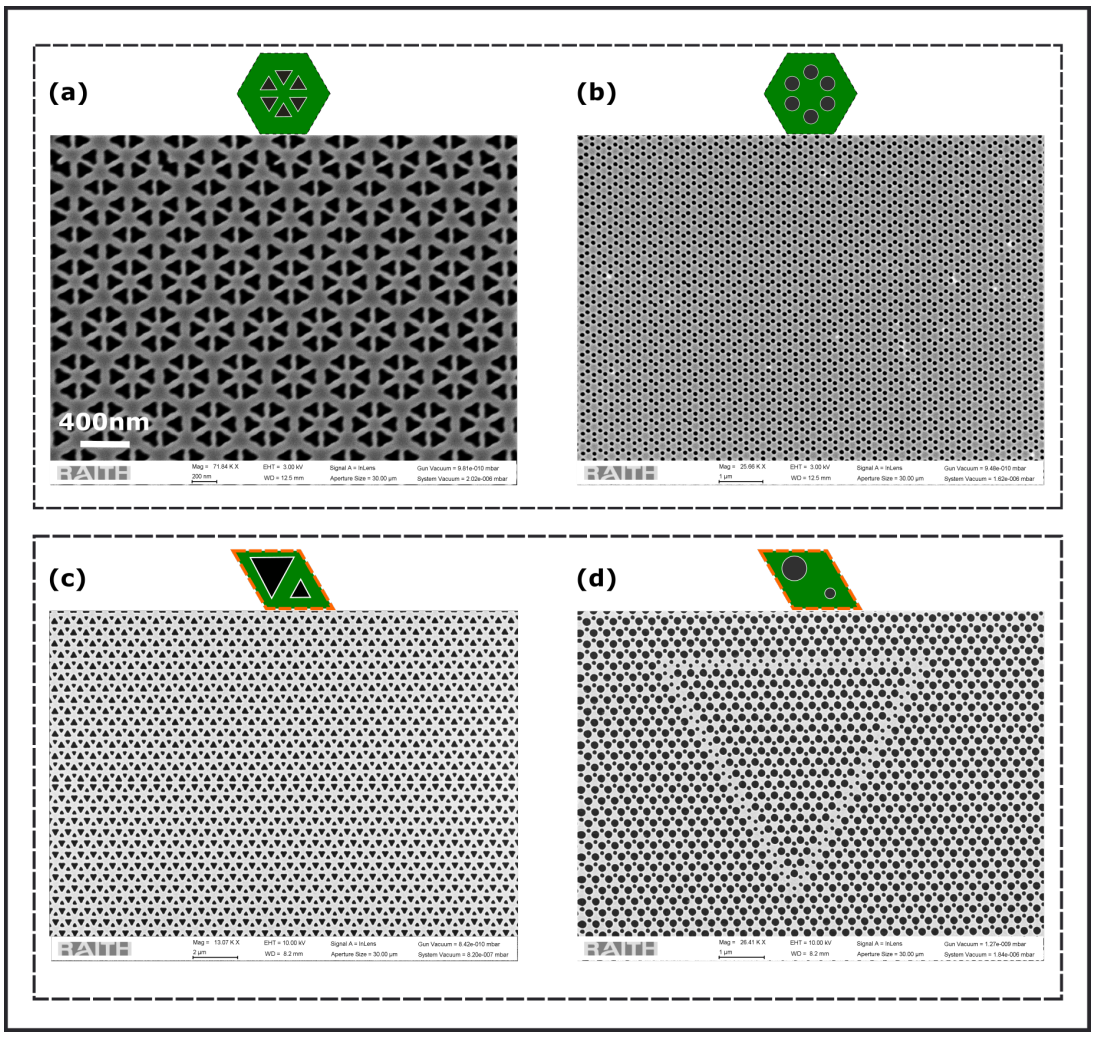

Figure 2.18: Example of a optimised and uniform fabricated QSH PhC with triangles (a) and (b) circles, as well as QVH PhC with (c) triangles and (d) circles.

and investigate the impact of different length on device functionalities. This is shown in Figure 2.16 b.

To ensure that the holes fully etched through the nominally 170nm thick GaAs membrane, several of these devices were scribed in the middle of the PhCs, and side-view SEMs were taken to estimate the etch depth of the holes with different shapes and sizes. As seen in Figure 2.17, measuring the etch depth demonstrates that the holes are deep enough to go all the way through the sacrificial layer.

Eventually parameters such as hole size, base dose and corner sharpness were optimised and desired PhC were achieved for the lattices considered in this thesis. An example of four optimised PhC are shown in Figure 2.18, including a QSH PhC with (a) triangular and (b) circular apertures, and a QVH PhC with (c) triangular and (d) circular apertures. The high-quality fabrication achieved for

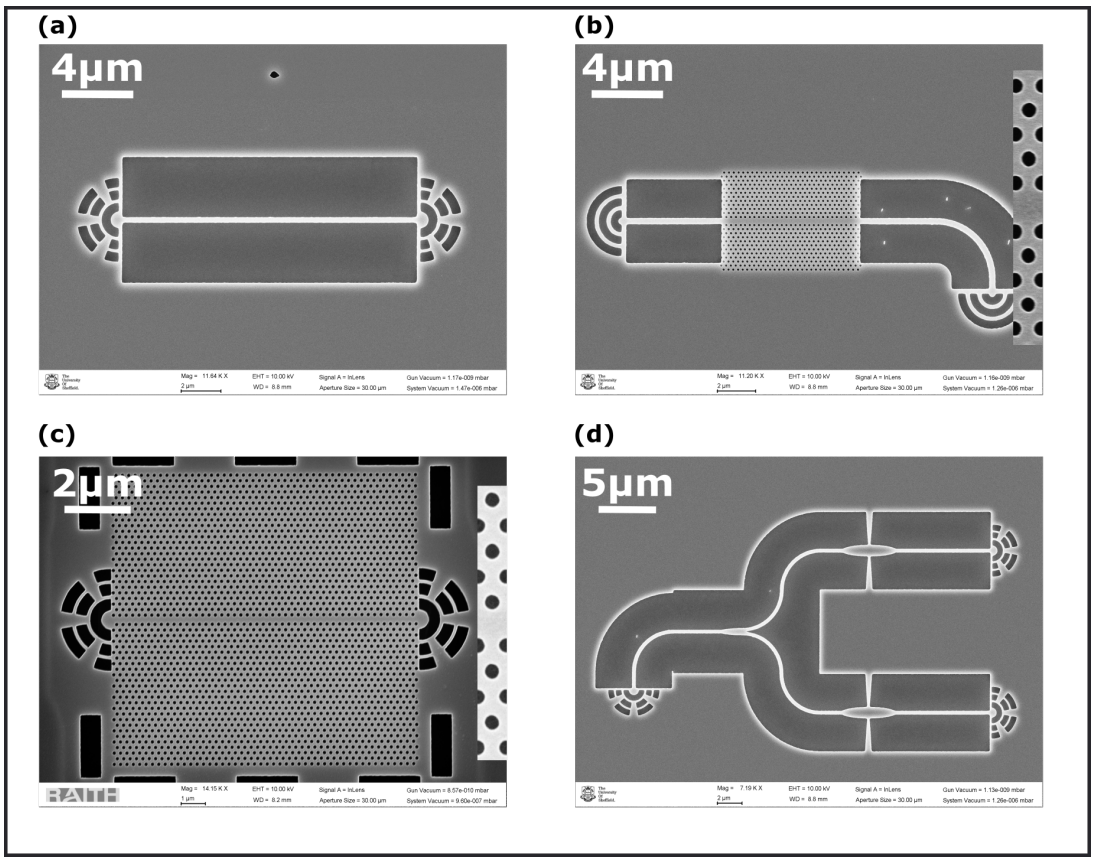

Figure 2.19: SEM images of (a) nano-beam, (b) W1 PhC, (c) glide plane and (d) nano-beam beam splitter waveguide. These devices were used for comparison of topological waveguides with conventional structures.

these PhC was crucial in making it possible to observe the simulated and predicted topological effects in designed devices.

In addition to topological photonic devices, a series of conventional (topologically trivial) devices were also designed and fabricated on the same sample to allow a comparison in terms of optical performances. These devices include standard waveguides such as a nano-beam, a W1 PhC and a glide plane waveguide, and can be seen in Figure 2.19.

Finally, additional photonic structures were also also developed, for instance to enable efficient off-chip collection of light from a PhC chip, or to support long suspended structures. Figure 2.20 shows some of these structures. (a) Shows an SEM image of a transmission device, where light injected into the input port (output coupler 1) is 50/50 split, half travelling through a topological PhC waveguide and exiting through an exit port (OC 8, top). The other half travelled through a nano-beam to a different port (OC 8, bottom). This device helped to measure and compare the transmission of light through a topological PhC compared to a standard nano-beam waveguide. The main components of this device include (d) a nanobeam splitter, used to split incoming light into two equal fractions,

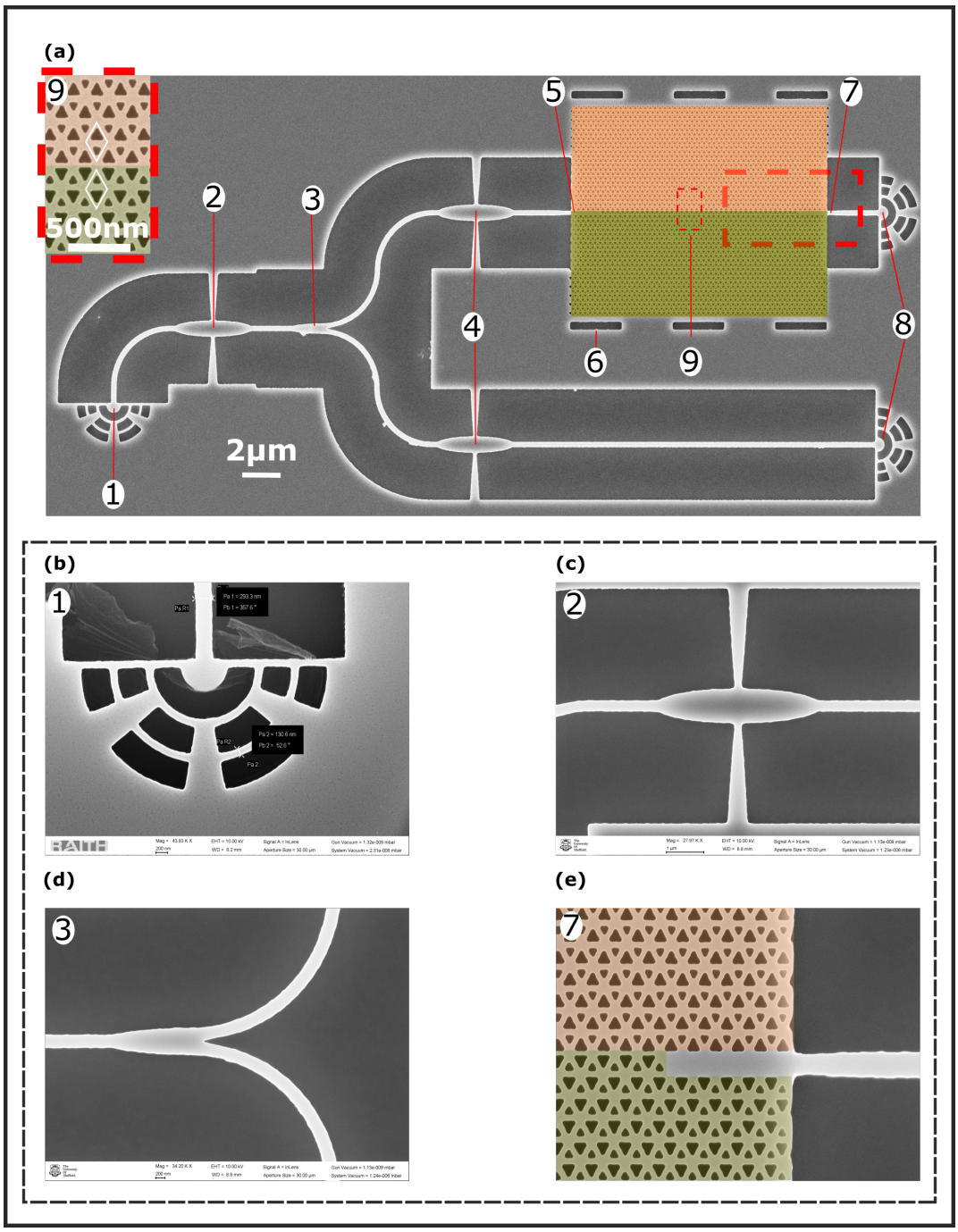

Figure 2.20: (a) SEM of a transmission device, with an input OC (1) and two output OCs (8), used to compare the transmission through a topological PhC waveguide (top WG) to that of a standard nano-beam (bottom WG). (b) Grating output coupler for collection of light into an optical fibre. (c) A support strut for the suspended nano-beam WGs. (d) A 50/50 nano-beam beam splitter. (e) Tapered nano-beam into a topological PhC WG for efficient input/output coupling of light.

and (c) support struts used to ensure that the long WGs do not collapse or bend after remove of the sacrificial layer. (e) Shows a nano-beam gradually tapered into a topological PhC for more efficient light coupling of light into and out of the PhC. Figure 2.20 b is a nano-beam coupled to a grating coupler. The latter scatters the incoming light from the nano-beam in an out-of-plane direction, to be collected into an optical fibre for signal processing.

The main chapters of this thesis are the papers either published or drafted (reprinted with permission from the publishers and authors) based on these designed, simulated, fabricated and experimentally investigated topological devices.

Bibliography

[1] Richard P. Feynman. "Simulating physics with computers". In: *International Journal of Theoretical Physics* 21 (6-7 June 1982), pp. 467–488. ISSN: 00207748. DOI: 10.1007/BF02650179. URL: https://link.springer.com/article/10.1007/BF02650179.

[2] P. Shor. "Algorithms for quantum computation: Discrete logarithms and factoring". In: *Proceedings of the 35th Annual IEEE Symposium on Foundations of Computer Science* 0 (1994). URL: https://philpapers.org/rec/SHOAFQ.

[3] Steven R. White. "Density-matrix algorithms for quantum renormalization groups". In: *Physical Review B* 48 (14 Oct. 1993), pp. 10345–10356. ISSN: 01631829. DOI: 10.1103/PhysRevB.48.10345. URL: https://journals.aps.org/prb/abstract/10.1103/PhysRevB.48.10345.

[4] H. J. Kimble. "The quantum internet". In: *Nature* 453 (7198 June 2008), pp. 1023–1030. ISSN: 14764687. DOI: 10.1038/nature07127.

[5] Michael A. Nielsen and Isaac L. Chuang. *Quantum Computation and Quantum Information: 10th Anniversary Edition*. 10th. USA: Cambridge University Press, 2011. ISBN: 1107002176.

[6] David P. DiVincenzo. "The Physical Implementation of Quantum Computation". In: *Fortschritte der Physik* 48 (9-11 Sept. 2000), pp. 771–783. ISSN: 00158208. DOI: 10.1002/1521-3978(200009)48:9/11<771::AID-PROP771>3.0.CO;2-E. URL: https://onlinelibrary.wiley.com/doi/10.1002/1521-3978(200009)48:9/11%3C771::AID-PROP771%3E3.0.CO;2-E.

[7] Michael A. Nielsen. "Optical quantum computation using cluster states". In: *Physical Review Letters* 93 (4 July 2004), p. 040503. ISSN: 00319007. DOI: 10.1103/PhysRevLett.93.040503. URL: https://journals.aps.org/prl/abstract/10.1103/PhysRevLett.93.040503.

[8] Richard J. Warburton. "Single spins in self-assembled quantum dots". In: *Nature Materials* 12 (6 May 2013), pp. 483–493. ISSN: 14764660. DOI: 10.1038/nmat3585. URL: www.nature.com/naturematerials.

[9] A. J. Ramsay. "A review of the coherent optical control of the exciton and spin states of semiconductor quantum dots". In: *Semiconductor Science and Technology* 25 (10 Oct. 2010), p. 23. ISSN: 02681242. DOI: 10.1088/0268-1242/25/10/103001. URL: https://iopscience.iop.org/article/10.1088/0268-1242/25/10/103001%20https://iopscience.iop.org/article/10.1088/0268-1242/25/10/103001/meta.

[10] Christof P Dietrich et al. "GaAs integrated quantum photonics : Towards compact and multi-functional quantum photonic integrated circuits". In: 894.6 (2016), pp. 870–894. DOI: 10.1002/lpor.201500321.

[11] Zhaoju Yang et al. "Topological Acoustics". In: *Phys. Rev. Lett.* 114 (11 Mar. 2015), p. 114301. DOI: 10.1103/PhysRevLett.114.114301. URL: https://link.aps.org/doi/10.1103/PhysRevLett.114.114301.

[12] Lifa Zhang et al. "Topological Nature of the Phonon Hall Effect". In: *Phys. Rev. Lett.* 105 (22 Nov. 2010), p. 225901. DOI: 10.1103/PhysRevLett.105.225901. URL: https://link.aps.org/doi/10.1103/PhysRevLett.105.225901.

[13] Jia Ningyuan et al. "Time- and Site-Resolved Dynamics in a Topological Circuit". In: *Phys. Rev. X* 5 (2 June 2015), p. 021031. DOI: 10.1103/PhysRevX.5.021031. URL: https://link.aps.org/doi/10.1103/PhysRevX.5.021031.

[14] Sebastian D. Huber. "Topological mechanics". In: *Nature Physics* 12 (7 June 2016), pp. 621–623. ISSN: 17452481. DOI: 10.1038/nphys3801. URL: http://arxiv.org/abs/1407.2890.

[15] Alexander B. Khanikaev et al. "Photonic topological insulators". In: *Nature Materials* 12 (3 Mar. 2013), pp. 233–239. ISSN: 14761122. DOI: 10.1038/nmat3520. URL: www.nature.com/naturematerials.

[16] K. v. Klitzing, G. Dorda and M. Pepper. "New Method for High-Accuracy Determination of the Fine-Structure Constant Based on Quantized Hall Resistance". In: *Phys. Rev. Lett.* 45 (6 Aug. 1980), pp. 494–497. DOI: 10.1103/PhysRevLett.45.494. URL: https://link.aps.org/doi/10.1103/PhysRevLett.45.494.

[17] R. B. Laughlin. "Quantized Hall conductivity in two dimensions". In: *Phys. Rev. B* 23 (10 May 1981), pp. 5632–5633. DOI: 10.1103/PhysRevB.23.5632. URL: https://link.aps.org/doi/10.1103/PhysRevB.23.5632.

[18] D. J. Thouless. "Quantization of particle transport". In: *Phys. Rev. B* 27 (10 May 1983), pp. 6083–6087. DOI: 10.1103/PhysRevB.27.6083. URL: https://link.aps.org/doi/10.1103/PhysRevB.27.6083.

[19] F. D. M. Haldane. "Model for a Quantum Hall Effect without Landau Levels: Condensed-Matter Realization of the "Parity Anomaly"". In: *Phys. Rev. Lett.* 61 (18 Oct. 1988), pp. 2015–2018. DOI: 10.1103/PhysRevLett.61.2015. URL: https://link.aps.org/doi/10.1103/PhysRevLett.61.2015.

[20] Michael Berry. "Quantal phase factors accompanying adiabatic changes". In: *Proceedings of the Royal Society of London. A. Mathematical and Physical Sciences* 392 (1802 Mar. 1984), pp. 45–57. ISSN: 2053-9169. DOI: 10.1098/rspa.1984.0023. URL: https://royalsocietypublishing.org/.

[21] Shiing-shen Chern. "Characteristic Classes of Hermitian Manifolds". In: *The Annals of Mathematics* 47 (1 Jan. 1946), p. 85. ISSN: 0003486X. DOI: 10.2307/1969037.

[22] Ling Lu, John D. Joannopoulos and Marin Soljačić. "Topological photonics". In: *Nature Photonics* 8 (11 Nov. 2014), pp. 821–829. ISSN: 1749-4885. DOI: 10.1038/nphoton.2014.248. URL: http://www.nature.com/articles/nphoton.2014.248.

[23] Chenyang Wang et al. "Universal numerical calculation method for the Berry curvature and Chern numbers of typical topological photonic crystals". In: *Frontiers of Optoelectronics* 13.1 (Mar. 2020), pp. 73–88. ISSN: 2095-2759. DOI: 10.1007/s12200-019-0963-9. URL: http://link.springer.com/10.1007/s12200-019-0963-9.

[24] Lan Feng Liu, Bo Lun Chen and Su Peng Kou. "Classification of topological insulators with time-reversal and inversion symmetry". In: *Communications in Theoretical Physics* 55 (5 May 2011), pp. 904–912. ISSN: 02536102. DOI: 10.1088/0253-6102/55/5/31. URL: http://ctp.itp.ac.cn.

[25] C. L. Kane and E. J. Mele. "Quantum Spin Hall Effect in Graphene". In: *Phys. Rev. Lett.* 95 (22 Nov. 2005), p. 226801. DOI: 10.1103/PhysRevLett.95.226801. URL: https://link.aps.org/doi/10.1103/PhysRevLett.95.226801.

[26] C. L. Kane and E. J. Mele. "Z_2 Topological Order and the Quantum Spin Hall Effect". In: *Phys. Rev. Lett.* 95 (14 Sept. 2005), p. 146802. DOI: 10.1103/PhysRevLett.95.146802. URL: https://link.aps.org/doi/10.1103/PhysRevLett.95.146802.

[27] B. Andrei Bernevig and Shou-Cheng Zhang. "Quantum Spin Hall Effect". In: *Phys. Rev. Lett.* 96 (10 Mar. 2006), p. 106802. DOI: 10.1103/PhysRevLett.96.106802. URL: https://link.aps.org/doi/10.1103/PhysRevLett.96.106802.

[28] B. Andrei Bernevig, Taylor L. Hughes and Shou Cheng Zhang. "Quantum spin hall effect and topological phase transition in HgTe quantum wells". In: *Science* 314 (5806 Dec. 2006), pp. 1757–1761. ISSN: 00368075. DOI: 10.1126/science.1133734. URL: www.sciencemag.org/cgi/content/full/314/5806/1754/DC1www.sciencemag.orgSCIENCEVOL31415DECEMBER2006http://science.sciencemag.org/.

[29] Markus König et al. "Quantum spin hall insulator state in HgTe quantum wells". In: *Science* 318 (5851 Nov. 2007), pp. 766–770. ISSN: 00368075. DOI: 10.1126/science.1148047. URL: http://science.sciencemag.org/.

[30] Di Xiao, Wang Yao and Qian Niu. "Valley-Contrasting Physics in Graphene: Magnetic Moment and Topological Transport". In: *Phys. Rev. Lett.* 99 (23 Dec. 2007), p. 236809. DOI: 10.1103/PhysRevLett.99.236809. URL: https://link.aps.org/doi/10.1103/PhysRevLett.99.236809.

[31] Menglin L. N. Chen et al. "Coexistence of pseudospin- and valley-Hall-like edge states in a photonic crystal with C_{3v} symmetry". In: *Phys. Rev. Research* 2 (4 Oct. 2020), p. 043148. DOI: 10.1103/PhysRevResearch.2.043148. URL: https://link.aps.org/doi/10.1103/PhysRevResearch.2.043148.

[32] Jeffrey C.Y. Teo and Taylor L. Hughes. "Topological defects in symmetry-protected topological phases". In: *Annual Review of Condensed Matter Physics* 8 (Mar. 2017), pp. 211–237. ISSN: 19475462. DOI: 10.1146/annurev-conmatphys-031016-025154. URL: https://ui.adsabs.harvard.edu/abs/2017ARCMP...8..211T/abstract.

[33] Yuanchen Deng, Minghui Lu and Yun Jing. "A comparison study between acoustic topological states based on valley Hall and quantum spin Hall effects". In: *The Journal of the Acoustical Society of America* 146 (1 July 2019), pp. 721–728. ISSN: 0001-4966. DOI: 10.1121/1.5115017. URL: http://asa.scitation.org/doi/10.1121/1.5115017.

[34] Bakhtiyar Orazbayev and Romain Fleury. "Quantitative robustness analysis of topological edge modes in C6 and valley-Hall metamaterial waveguides". In: *Nanophotonics* 8 (8 Aug. 2019), pp. 1433–1441. ISSN: 21928614. DOI: 10.1515/nanoph-2019-0137. URL: https://doi.org/10.1515/nanoph-2019-0137.

[35] Weijian Chen et al. "Nonreciprocity in synthetic photonic materials with nonlinearity". In: *MRS Bulletin* 43 (6 June 2018), pp. 443–451. ISSN: 08837694. DOI: 10.1557/mrs.2018.124. URL: https://www.cambridge.org/core/terms.https://doi.org/10.1557/mrs.2018.124Downloadedfromhttps://www.cambridge.org/core..

[36] F. D. M. Haldane and S. Raghu. "Possible Realization of Directional Optical Waveguides in Photonic Crystals with Broken Time-Reversal Symmetry". In: *Phys. Rev. Lett.* 100 (1 Jan. 2008), p. 013904. DOI: 10.1103/PhysRevLett.100.013904. URL: https://link.aps.org/doi/10.1103/PhysRevLett.100.013904.

[37] S. Raghu and F. D. M. Haldane. "Analogs of quantum-Hall-effect edge states in photonic crystals". In: *Phys. Rev. A* 78 (3 Sept. 2008), p. 033834. DOI: 10.1103/PhysRevA.78.033834. URL: https://link.aps.org/doi/10.1103/PhysRevA.78.033834.

[38] Zheng Wang et al. "Reflection-Free One-Way Edge Modes in a Gyromagnetic Photonic Crystal". In: *Phys. Rev. Lett.* 100 (1 Jan. 2008), p. 013905. DOI: 10.1103/PhysRevLett.100.013905. URL: https://link.aps.org/doi/10.1103/PhysRevLett.100.013905.

[39] Zheng Wang et al. "Observation of unidirectional backscattering-immune topological electromagnetic states". In: *Nature* 461 (7265 Oct. 2009), pp. 772–775. ISSN: 00280836. DOI: 10.1038/nature08293. URL: https://www.nature.com/articles/nature08293.

[40] Mohammad Hafezi et al. "Robust optical delay lines with topological protection". In: *Nature Physics* 7 (11 Nov. 2011), pp. 907–912. ISSN: 17452473. DOI: 10.1038/nphys2063. URL: www.nature.com/naturephysics.

[41] M. Hafezi et al. "Imaging topological edge states in silicon photonics". In: *Nature Photonics* 7 (12 Dec. 2013), pp. 1001–1005. ISSN: 17494885. DOI: 10.1038/nphoton.2013.274. URL: www.nature.com/naturephotonics.

[42] S. Mittal et al. "Topologically Robust Transport of Photons in a Synthetic Gauge Field". In: *Phys. Rev. Lett.* 113 (8 Aug. 2014), p. 087403. DOI: 10.1103/PhysRevLett.113.087403. URL: https://link.aps.org/doi/10.1103/PhysRevLett.113.087403.

[43] R. O. Umucal ılar and I. Carusotto. "Artificial gauge field for photons in coupled cavity arrays". In: *Phys. Rev. A* 84 (4 Oct. 2011), p. 043804. DOI: 10.1103/PhysRevA.84.043804. URL: https://link.aps.org/doi/10.1103/PhysRevA.84.043804.

[44] Mikael C. Rechtsman et al. "Photonic Floquet topological insulators". In: *Nature* 496 (7444 Apr. 2013), pp. 196–200. ISSN: 00280836. DOI: 10.1038/nature12066. URL: https://www.nature.com/articles/nature12066.

[45] Gal Harari et al. "Topological insulator laser: Theory". In: *Science* 359 (6381 Mar. 2018). ISSN: 10959203. DOI: 10.1126/science.aar4003. URL: http://science.sciencemag.org/.

[46] Miguel A. Bandres et al. "Topological insulator laser: Experiments". In: *Science* 359 (6381 Mar. 2018). ISSN: 10959203. DOI: 10.1126/science.aar4005. URL: http://science.sciencemag.org/.

[47] Yasutomo Ota et al. "Topological photonic crystal nanocavity laser". In: *Communications Physics* 1 (1 Dec. 2018), pp. 1–8. ISSN: 23993650. DOI: 10.1038/s42005-018-0083-7. URL: https://www.nature.com/articles/s42005-018-0083-7.

[48] Sabyasachi Barik et al. "A topological quantum optics interface". In: *Science* 359.6376 (2018), pp. 666–668. ISSN: 0036-8075. DOI: 10.1126/science.aaq0327. eprint: https://science.sciencemag.org/content/359/6376/666.full.pdf. URL: https://science.sciencemag.org/content/359/6376/666.

[49] Alexey Slobozhanyuk et al. "Three-dimensional all-dielectric photonic topological insulator". In: *Nature Photonics 2016 11:2* 11 (2 Dec. 2016), pp. 130–136. ISSN: 1749-4893. DOI: 10.1038/nphoton.2016.253. URL: https://www.nature.com/articles/nphoton.2016.253.

[50] Yihao Yang et al. "Realization of a three-dimensional photonic topological insulator". In: *Nature* 565 (7741 Jan. 2019), pp. 622–626. ISSN: 14764687. DOI: 10.1038/s41586-018-0829-0. URL: https://doi.org/10.1038/s41586-018-0829-0.

[51] Long-Hua Wu and Xiao Hu. "Scheme for Achieving a Topological Photonic Crystal by Using Dielectric Material". In: *Physical Review Letters* 114 (22 June 2015), p. 223901. ISSN: 0031-9007. DOI: 10.1103/PhysRevLett.114.223901. URL: https://link.aps.org/doi/10.1103/PhysRevLett.114.223901.

[52] Erik Sauer, Juan Pablo Vasco and Stephen Hughes. "Theory of intrinsic propagation losses in topological edge states of planar photonic crystals". In: *Phys. Rev. Research* 2 (4 Oct. 2020), p. 043109. DOI: 10.1103/PhysRevResearch.2.043109. URL: https://link.aps.org/doi/10.1103/PhysRevResearch.2.043109.

[53] Tzuhsuan Ma and Gennady Shvets. "All-Si valley-Hall photonic topological insulator". In: *New Journal of Physics* 18 (2 Feb. 2016). ISSN: 13672630. DOI: 10.1088/1367-2630/18/2/025012.

[54] Mahmoud Jalali Mehrabad et al. "Chiral topological photonics with an embedded quantum emitter". In: *Optica* 7.12 (Dec. 2020), pp. 1690–1696. DOI: 10.1364/OPTICA.393035. URL: http://www.osapublishing.org/optica/abstract.cfm?URI=optica-7-12-1690.

[55] Long-Hua Wu and Xiao Hu. "Scheme for Achieving a Topological Photonic Crystal by Using Dielectric Material". In: *Phys. Rev. Lett.* 114 (22 June 2015), p. 223901. DOI: 10.1103/PhysRevLett.114.223901. URL: https://link.aps.org/doi/10.1103/PhysRevLett.114.223901.

[56] Yongquan Zeng et al. "Electrically pumped topological laser with valley edge modes". In: *Nature* 578.April 2019 (2020). ISSN: 1476-4687. DOI: 10.1038/s41586-020-1981-x. URL: http://dx.doi.org/10.1038/s41586-020-1981-x.

[57] Sabyasachi Barik et al. "Two-dimensionally confined topological edge states in photonic crystals". In: *New Journal of Physics* 18.11 (Nov. 2016), p. 113013. ISSN: 13672630. DOI: 10.1088/1367-2630/18/11/113013. arXiv: 1605.08822. URL: https://iopscience.iop.org/article/10.1088/1367-2630/18/11/113013%20https://iopscience.iop.org/article/10.1088/1367-2630/18/11/113013/meta.

[58] Hongbo Huang, Shaoyong Huo and Jiujiu Chen. "Reconfigurable Topological Phases in Two-Dimensional Dielectric Photonic Crystals". In: *Crystals* 9.4 (2019). ISSN: 2073-4352. DOI: 10.3390/cryst9040221. URL: https://www.mdpi.com/2073-4352/9/4/221.

[59] Zhongfu Li, Hsun-Chi Chan and Yuanjiang Xiang. "Fragile topology based helical edge states in two-dimensional moon-shaped photonic crystals". In: *Phys. Rev. B* 102 (24 Dec. 2020), p. 245149. DOI: 10.1103/PhysRevB.102.245149. URL: https://link.aps.org/doi/10.1103/PhysRevB.102.245149.

[60] Mikhail I. Shalaev et al. "Robust topologically protected transport in photonic crystals at telecommunication wavelengths". In: *Nature Nanotechnology* 14 (1 Jan. 2019), pp. 31–34. ISSN: 1748-3387. DOI: 10.1038/s41565-018-0297-6. URL: http://www.nature.com/articles/s41565-018-0297-6.

[61] YuHui Han et al. "Design of broadband all-dielectric valley photonic crystals at telecommunication wavelength". In: *Optics Communications* 488 (2021), p. 126847. ISSN: 0030-4018. DOI: https://doi.org/10.1016/j.optcom.2021.126847. URL: https://www.sciencedirect.com/science/article/pii/S0030401821000973.

[62] Hironobu Yoshimi et al. "Slow light waveguides in topological valley photonic crystals". In: *Optics Letters* 45.9 (2020), p. 2648. ISSN: 0146-9592. DOI: 10.1364/ol.391764.

[63] Hironobu Yoshimi et al. "Experimental demonstration of topological slow light waveguides in valley photonic crystals". In: *arXiv* (Feb. 2021). URL: http://arxiv.org/abs/2102.09252.

[64] M. A. Reed et al. "Observation of discrete electronic states in a zero-dimensional semiconductor nanostructure". In: *Phys. Rev. Lett.* 60 (6 Feb. 1988), pp. 535–537. DOI: 10.1103/PhysRevLett.60.535. URL: https://link.aps.org/doi/10.1103/PhysRevLett.60.535.

[65] D. Leonard et al. "Direct formation of quantum-sized dots from uniform coherent islands of InGaAs on GaAs surfaces". In: *Applied Physics Letters* 63.23 (1993), pp. 3203–3205. DOI: 10.1063/1.110199. eprint: https://doi.org/10.1063/1.110199. URL: https://doi.org/10.1063/1.110199.

[66] Clemens Matthiesen, Anthony Nickolas Vamivakas and Mete Atatüre. "Subnatural Linewidth Single Photons from a Quantum Dot". In: *Phys. Rev. Lett.* 108 (9 Feb. 2012), p. 093602. DOI: 10.1103/PhysRevLett.108.093602. URL: https://link.aps.org/doi/10.1103/PhysRevLett.108.093602.

[67] Kathryn E. Sautter, Kevin D. Vallejo and Paul J. Simmonds. "Strain-driven quantum dot self-assembly by molecular beam epitaxy". In: *Journal of Applied Physics* 128.3 (2020), p. 031101. DOI: 10.1063/5.0012066. eprint: https://doi.org/10.1063/5.0012066. URL: https://doi.org/10.1063/5.0012066.

[68] S. Franchi et al. "Quantum dot nanostructures and molecular beam epitaxy". In: *Progress in Crystal Growth and Characterization of Materials* 47 (2-3 Jan. 2003), pp. 166–195. ISSN: 09608974. DOI: 10.1016/j.pcrysgrow.2005.01.002.

[69] Christof P. Dietrich et al. "GaAs integrated quantum photonics: Towards compact and multi-functional quantum photonic integrated circuits". In: *Laser & Photonics Reviews* 10.6 (2016), pp. 870–894. DOI: https://doi.org/10.1002/lpor.201500321. eprint: https://onlinelibrary.wiley.com/doi/pdf/10.1002/lpor.201500321. URL: https://onlinelibrary.wiley.com/doi/abs/10.1002/lpor.201500321.

[70] K. Hennessy et al. "Quantum nature of a strongly coupled single quantum dot-cavity system". In: *Nature* 445 (7130 Feb. 2007), pp. 896–899. ISSN: 14764687. DOI: 10.1038/nature05586. URL: https://www.nature.com/articles/nature05586.

[71] T. Yoshle et al. "Vacuum Rabi splitting with a single quantum dot in a photonic crystal nanocavity". In: *Nature* 432 (7014 Nov. 2004), pp. 200–203. ISSN: 00280836. DOI: 10.1038/nature03119. URL: www.nature.com/nature..

[72] A. Dousse et al. "Controlled Light-Matter Coupling for a Single Quantum Dot Embedded in a Pillar Microcavity Using Far-Field Optical Lithography". In: *Phys. Rev. Lett.* 101 (26 Dec. 2008), p. 267404. DOI: 10.1103/PhysRevLett.101.267404. URL: https://link.aps.org/doi/10.1103/PhysRevLett.101.267404.

[73] Biswarup Guha et al. "Surface-enhanced gallium arsenide photonic resonator with quality factor of 6 × 106". In: *Optica* 4.2 (Feb. 2017), pp. 218–221. DOI: 10.1364/OPTICA.4.000218. URL: http://www.osapublishing.org/optica/abstract.cfm?URI=optica-4-2-218.

[74] Si Chen et al. "Quality Factor Control in Laterally-Coupled Vertical Cavities". In: *2018 IEEE International Conference on Manipulation, Manufacturing and Measurement on the Nanoscale (3M-NANO)*. 2018, pp. 60–64. DOI: 10.1109/3M-NANO.2018.8552229.

[75] Babak Bahari et al. "Photonic quantum Hall effect and multiplexed light sources of large orbital angular momenta". In: *Nature Physics 2021 17:6* 17 (6 Feb. 2021), pp. 700–703. ISSN: 1745-2481. DOI: 10.1038/s41567-021-01165-8. URL: https://www.nature.com/articles/s41567-021-01165-8.

[76] Himadri S. Dhar et al. "Quest for vortices in photon condensates". In: *Phys. Rev. A* 104 (3 Sept. 2021), p. L031505. DOI: 10.1103/PhysRevA.104.L031505. URL: https://link.aps.org/doi/10.1103/PhysRevA.104.L031505.

[77] S. Dufferwiel et al. "Spin Textures of Exciton-Polaritons in a Tunable Microcavity with Large TE-TM Splitting". In: *Phys. Rev. Lett.* 115 (24 Dec. 2015), p. 246401. DOI: 10.1103/PhysRevLett.115.246401. URL: https://link.aps.org/doi/10.1103/PhysRevLett.115.246401.

Chapter 3

A semiconductor topological photonic ring resonator

Applied Physics Letters ARTICLE scitation.org/journal/apl

A semiconductor topological photonic ring resonator

Cite as: Appl. Phys. Lett. **116**, 061102 (2020); doi: 10.1063/1.5131846
Submitted: 16 October 2019 · Accepted: 4 February 2020 ·
Published Online: 11 February 2020

M. Jalali Mehrabad,[1,a)] A. P. Foster,[1,b)] R. Dost,[1] E. Clarke,[2] P. K. Patil,[2] I. Farrer,[3] J. Heffernan,[3] M. S. Skolnick,[1] and L. R. Wilson[1]

AFFILIATIONS

[1]Department of Physics and Astronomy, University of Sheffield, Sheffield S3 7RH, United Kingdom
[2]EPSRC National Epitaxy Facility, University of Sheffield, Sheffield S1 4DE, United Kingdom
[3]Department of Electronic and Electrical Engineering, University of Sheffield, Sheffield S1 4DE, United Kingdom

[a)]mjalalimehrabad1@sheffield.ac.uk
[b)]andrew.foster@sheffield.ac.uk

ABSTRACT

Unidirectional photonic edge states arise at the interface between two topologically distinct photonic crystals. Here, we demonstrate a micrometer-scale GaAs photonic ring resonator, created using a spin Hall-type topological photonic crystal waveguide. Embedded InGaAs quantum dots are used to probe the mode structure of the device. We map the spatial profile of the resonator modes and demonstrate the control of the mode confinement through tuning of the photonic crystal lattice parameters. The intrinsic chirality of the edge states makes them of interest for applications in integrated quantum photonics, and the resonator represents an important building block toward the development of such devices with embedded quantum emitters.

The integration of quantum photonic elements on chip presents a highly promising route to the realization of scalable quantum devices. A key requirement of such an approach is the development of optical waveguides exhibiting low loss and negligible backscatter.[1] Recently, topological waveguides have emerged as a new class of photonic devices enabling the robust propagation of light on chip.[2–10] At the interface between two topologically distinct photonic crystals (PhCs), counterpropagating edge states of opposing helicity arise, which are ideal for optical waveguiding.[5,10–13] Significant developments in this field include the demonstration of efficient guiding of light around tight corners,[4,14–16] robust transport despite the presence of defects,[17] and integration with passive optical elements including nanobeam waveguides[15] and grating couplers.[4] Compatibility with embedded quantum emitters such as quantum dots (QDs) has been demonstrated and used to probe the waveguide transmission.[4,14] Recently, chiral coupling of a QD to a topological waveguide was demonstrated.[4,18,19] This is a result of the intrinsic helicity of the edge states and is of great interest for chiral quantum optics.[20]

Here, we use a spin Hall-type topological waveguide to create a GaAs topological photonic ring resonator and probe its mode structure using embedded InGaAs QDs. We map the spatial dependence of the confined modes of the resonator and demonstrate that the perturbation of the PhC lattice can be used to tune the lateral confinement of the modes.

A schematic of the PhC forming the basis of our topological ring resonator is shown in Fig. 1(a). The unit cell of the PhC consists of six triangular air holes of side length s, etched into a GaAs membrane of thickness h. A two-dimensional PhC lattice is created using a hexagonal array of unit cells with period $a = s/0.31$. A key parameter of the lattice is the distance R from the origin of the unit cell to the center of each triangular aperture, with a graphene-like structure formed when $R = R_0 = a/3$. We model the structure using a commercially available 3D finite-difference time-domain (FDTD) electromagnetic simulator[21] and show that in this case the PhC band structure exhibits a Dirac cone at the Γ point, as shown in Fig. 1(b).

However, when a perturbation is introduced such that $R \neq a/3$, a bandgap is opened at the Γ point. This is shown for the case of PhCs formed using either expanded ($R_e > R_0$) or shrunken ($R_s < R_0$) unit cells in Figs. 1(c) and 1(d). Using FDTD, we determine the bandwidth of the PhC bandgap for a perturbation of either $R_e/R_0 = 1.05$ or $R_s/R_0 = 0.94$ to be ∼20 THz (∼55 nm), centered at ∼330 THz (∼908 nm). For the simulations, we took $h = 170$ nm and $s = 140$ nm. It is instructive to consider the nature of the bands in this case. For a shrunken (expanded) unit cell, the higher energy band has d-(p-) like

Applied Physics Letters ARTICLE scitation.org/journal/apl

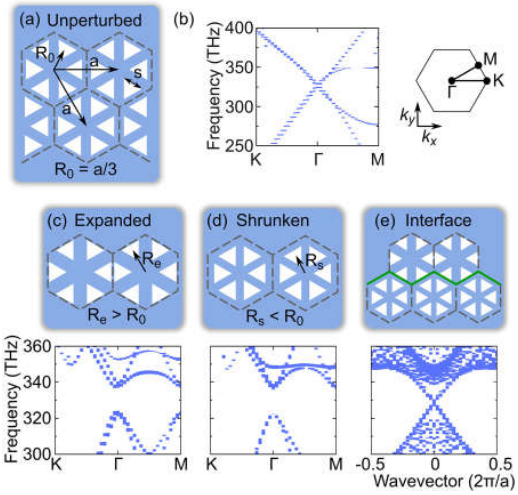

FIG. 1. (a) Schematic showing the unperturbed photonic crystal (PhC). The triangles represent air holes. A two-dimensional PhC is formed using a triangular lattice of unit cells, with pitch a. (b) Band structure of the unperturbed lattice, revealing a Dirac cone at the Γ point. Points of high symmetry in the Brillouin zone are shown in the accompanying schematic. (c) and (d) Schematic of (c) expanded and (d) shrunken unit cells. The band structure for a PhC formed from such a unit cell is also shown. In each case, a bandgap is opened at the Γ point. (e) Schematic of an interface formed between expanded and shrunken unit cells. Edge modes are seen to cross the bandgap in this case. The parameters used for the band structure calculations are as follows: refractive index = 3.4, $h = 170$ nm, $s = 140$ nm, $a = 445$ nm, $R_e = 156$ nm, and $R_s = 141$ nm.

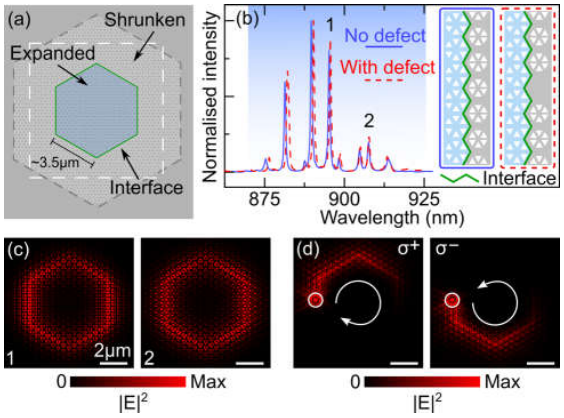

FIG. 2. (a) Schematic of the ring resonator. The topological interface is indicated by the green line. (b) Mode spectrum at the resonator interface (blue solid line), determined using FDTD simulation. Resonator modes can be seen within the topological bandgap (shaded). The mode spectrum is also shown for a resonator containing a defect in the form of a single unit cell omitted from the interface (red dashed line). The inset shows a schematic of one side of the resonator, with and without the defect. (c) Spatially resolved electric field intensity (linear scale) in the plane of the device, for the two modes numbered in (b) (without a defect). Confinement of light at the interface is clearly seen. The electric field intensity is evaluated within the white dashed region in (a). (d) Spatially resolved electric field intensity (linear scale) in the plane of the device, for a (left) σ^+ or (right) σ^- polarized dipole source (position given by the open circle). The field intensity is averaged over the first 200 fs of simulation time. Chiral emission is observed, with the direction of propagation (arrows) dependent on the dipole polarization. The dipole is coupled to mode 1, as labeled in (b).

character, and the lower energy band is p-(d-) like.[3] This difference in character has an important consequence when an interface is realized between the two unit cells [see Fig. 1(e)]. The change in character of adjacent bands necessitates the formation of edge states, connecting bands of the same character across the interface. These can be clearly seen in the interface band structure shown in Fig. 1(e). The edge states exist within the bandgap, and the interface therefore supports confined modes, which form the basis of a topological photonic waveguide.[22]

We harness the interface edge modes to create a photonic ring resonator. A hexagonal array of expanded unit cells ($R_e/R_0 = 1.05$) is embedded within a host array of shrunken unit cells ($R_s/R_0 = 0.94$), as shown schematically in Fig. 2(a). (In the following, this corresponds to an average perturbation of 5.5%.) Internally, each side of the resonator is 8 unit cells in length such that the total path length of the interface is ∼21 μm. The hexagonal host array has an internal side length of 31 unit cells. FDTD simulations of the resonator reveal a characteristic spectral mode structure [Fig. 2(b)], which lies within the topological bandgap (determined by monitoring the power radiated by a dipole source in an expanded-unit-cell PhC). The three most prominent modes have an average quality factor (Q factor) of 1760 (range 1600–1900). Spatial intensity profiles for two different modes [Fig. 2(c)] confirm that they are confined to the topological interface.

The topological character of the resonator modes can be seen in protection against certain defects and in the helical nature of the modes. We consider a defect in the form of a single unit cell missing from the resonator interface. This is seen to have little effect on the mode spectrum [dashed line in Fig. 2(b)] and does not affect the mode Q factors. To demonstrate the helicity of the modes, we position a circularly polarized dipole at the center of a unit cell adjacent to the interface and show that the propagation direction of the dipole emission is dependent on the handedness of the dipole polarization [see Fig. 2(d)]. This highlights the potential of the resonator for chiral quantum optics[20] and spin–photon interfaces.[23,24]

Next, we investigate the theoretical dependence of the resonator Q factor, first on the device dimensions and then on the PhC perturbation. Figure 3(a) shows the mode spectra for five different resonators with an internal side length between 4 and 8 unit cells. The host PhC has a side length of 31 unit cells, and the perturbation is 5.5%. The number of modes (mode spacing) increases (decreases) with the increasing resonator size, as is expected for a Fabry–Pérot-type resonator.[25] In each case, the Q factor of a mode near the center of the distribution (marked with a star) is calculated. The Q factor is greater than 2000 for the smallest resonator and decreases slightly with the increasing resonator size. Fixing the internal size of the ring at 4 unit cells, we then vary the perturbation and see that the Q factor increases with decreasing perturbation, down to 3.5% perturbation [blue circles in Fig. 3(b)]. The dependence of the Q factor on both the resonator size and perturbation can be understood as the result of the finite propagation length of the waveguide. This is due to the scattering of the mode at the Γ point and subsequent coupling to free-space modes, the probability of which increases with increasing perturbation.[3,22] For the smallest perturbation of 2.5%, we find that the size of the host PhC

Applied Physics Letters ARTICLE scitation.org/journal/apl

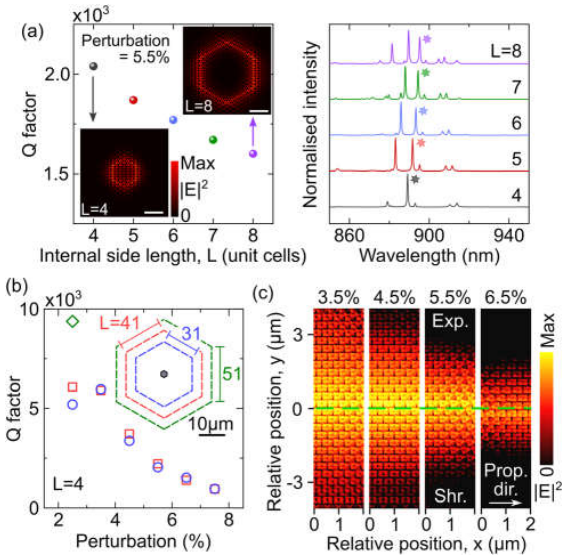

FIG. 3. (a) Simulated resonator Q factor vs side length L (the number of internal unit cells at the interface) for a PhC perturbation of 5.5%. The size of the host PhC is fixed at 31 unit cells. Electric field intensity profiles (linear scale) for $L = 4$ and $L = 8$ are shown as insets (scale bar, 2 μm). Mode spectra for each case are shown on the right. The Q factor is evaluated for the mode marked with a star. (b) Simulated Q factor vs perturbation for a resonator with $L = 4$. Blue circles (red squares, green diamond) correspond to a host PhC size of 31 (41, 51) unit cells. The inset shows the relative size of the resonator (black hexagon) and the host PhC in each case. (c) Simulated spatially resolved electric field intensity for waveguides with perturbations of 3.5%–6.5%, on a logarithmic intensity scale. The mode propagates in the x direction (prop. dir.). The unit cell is expanded (Exp.) above and shrunken (Shr.) below the interface, which is highlighted by the dashed green line.

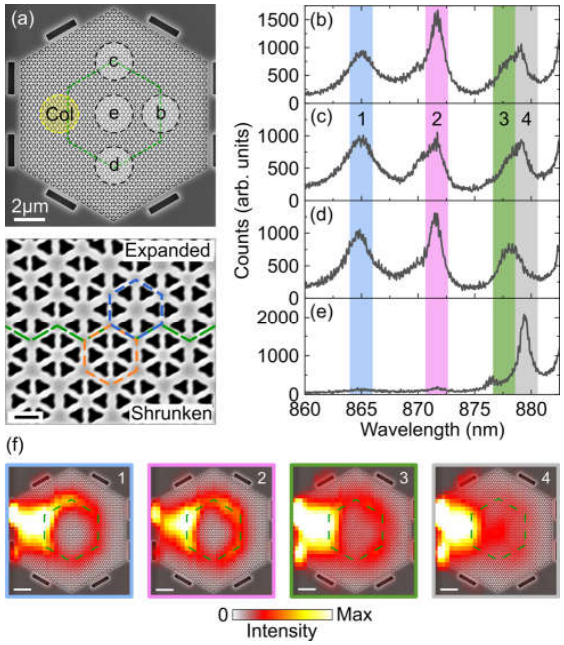

FIG. 4. (a) SEM overview of the ring resonator (top) and close up of the waveguide interface (bottom; scale bar, 200 nm). (b)–(e) High power PL spectra for four different excitation locations on the device, as labeled in (a). In each case, the collection spot was fixed on the left hand side of the resonator [yellow circle labeled Col in (a)]. (f) Spatially resolved, integrated PL intensity maps for four different bandwidths, as numbered and color-coded in (b)–(e). The zero of the linear color scale is transparent. A SEM image of the device is positioned under each map, and the interface is highlighted with a dashed green line. Scale bar, 2 μm.

must be increased to obtain the largest Q factor. Increasing the internal side length of the host initially to 41 unit cells [red squares in Fig. 3(b)] has little effect for perturbations greater than 2.5%, indicating that in this case the host PhC is already sufficiently large. However, for a host PC size of 51 unit cells (green diamond), a higher Q factor of ~9400 is obtained for a perturbation of 2.5%. This is due to the mode confinement weakening as the perturbation decreases such that the host PhC must be larger to prevent in-plane loss into the membrane surrounding the device [see Fig. 3(c)].

Experimentally, we fabricate topological ring resonators in a nominally 170 nm-thick GaAs membrane, using standard electron beam lithography and dry etching techniques. A scanning electron microscopy (SEM) image of a representative ring resonator is shown in Fig. 4(a). The resonator has an internal side length of 8 unit cells and is embedded in a host PhC with a side length restricted to 16 unit cells due to experimental limitations. The simulated Q factor in this case is reduced to a maximum of ~870 for a perturbation of 5.5% due to additional loss into the membrane. Devices are fabricated with perturbation between 2.5% ($R_e/R_0 = 1.02$, $R_s/R_0 = 0.97$) and 5.5% ($R_e/R_0 = 1.05$, $R_s/R_0 = 0.94$).

To characterize the devices, the sample is mounted in an exchange gas cryostat, and the waveguide modes of the resonator are probed using micro-photoluminescence (μ-PL) spectroscopy. We use an excitation wavelength of 808 nm and focus the laser to a spot size of ~2μm. High power excitation is used to generate broadband emission from the QD ensemble. Mirrors in the collection path, with motorized adjusters, enable the collection of PL emission from a location either coincident with, or spatially distinct from, the excitation spot. We first position the excitation laser spot on one side of the ring [region "b" in Fig. 4(a)] and detect light emitted from a location on the opposite side of the resonator [region "Col" in Fig. 4(a)]. This enables us to detect light coupled to the interface, while rejecting PL that is emitted into free-space modes. The PL spectrum for a ring resonator with a unit cell perturbation of 5.5% is shown in Fig. 4(b). Resonator modes with a period of ~7 nm are observed, consistent with simulation. The modes have Q factors in the range of 200–500, possibly limited by dopant-related absorption in the GaAs membrane. The wavelength range in which the modes are observed is slightly shorter than in simulation, an effect we attribute to larger fabricated hole sizes than designed. The short wavelength edge of the bandgap therefore lies at a wavelength outside the bandwidth of the QD emission such that the bandwidth of the topological bandgap cannot be determined precisely.

We next excite PL at several other positions on the resonator interface while collecting from the same location as previously and observe that the mode structure remains unchanged [see Figs. 4(c)

Applied Physics Letters ARTICLE scitation.org/journal/apl

and 4(d)]. However, when the excitation location is distinct from the interface (for instance, at the very center of the resonator), the PL spectrum is quite different, and the modes observed previously at the interface are absent [Fig. 4(e)]. This is strong evidence that the modes are confined to the interface. [A different peak is seen in Fig. 4(e). We show below that this is distinct from the resonator modes.]

To visualize the modes more clearly, we raster scan the excitation laser across the device, simultaneously acquiring PL spectra from the same (fixed) collection spot used above. For each excitation position on the device, we sum the measured PL intensity over three different bandwidths corresponding to different resonator modes seen in Figs. 4(b)–4(d). The resulting PL intensity maps are shown in Fig. 4(f). Several features are apparent in the data. Most significantly, PL emission is observed from all positions along the resonator interface, with a clear node in the center of the resonator, showing that light is guided along the interface. A secondary feature is the bright region on the left of each intensity map, which corresponds to the PL collection location. This is the result of a fraction of the QD PL emission coupling to free-space modes. Such emission is collected only when the excitation laser is positioned close to the collection spot. The PL maps also serve to highlight the location of trenches used to aid fabrication of the device (for instance, the two bright regions to the left of the collection location). These were used to accurately position the device schematic under each PL map. In Fig. 4(f), we also show an intensity map integrated over the single peak seen in the PL spectrum from the center of the device. The map is quite different to those for the resonator modes seen at the interface, as this peak is not related to guided modes at the interface.

Finally, we investigate the effect of the unit cell perturbation on the spatial confinement of the resonator modes. Figure 5(a) shows an integrated PL intensity map for each of four different ring resonators, with unit cell perturbation increasing from 2.5% to 5.5%. In each case, the intensity map corresponds to a single resonator mode, centered at ∼865 nm. A clear trend is observed, with the mode confinement being the strongest for the largest perturbation and weakening with decreasing perturbation. For a perturbation of 5.5%, the mode decays over a distance of $2.7 \pm 0.1\,\mu$m, transverse to the propagation direction. This value increases to $4.1 \pm 0.2\,\mu$m for a perturbation of only 2.5%.

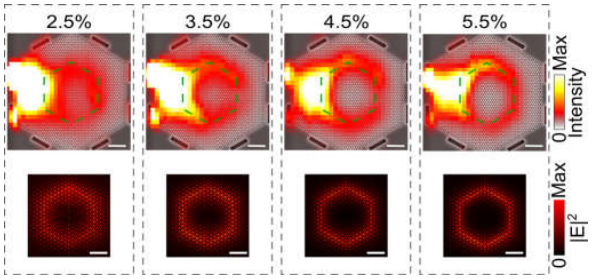

FIG. 5. Dependence of waveguide mode transverse confinement on perturbation. Upper panels: spatially resolved, integrated PL intensity maps for different unit cell perturbations (as labeled). The integration is for a mode centered at ∼865 nm in each case. The zero of the linear color scale is transparent. A SEM image of the device is positioned under each map, and the interface is highlighted with a dashed green line. Lower panels: Simulated spatially resolved electric field intensity (linear scale) of a representative ring resonator mode, for devices with the same perturbations as in the experiment. Scale bar, 2 μm.

The change in confinement is consistent with FDTD simulations [see Figs. 3 and 5(b)], which show that, as the perturbation is decreased, the waveguide mode increasingly extends into the bulk PhC. From the simulations, we estimate that the spatial extent of the mode normal to the propagation direction increases from ∼820 nm for a perturbation of 5.5% to ∼1640 nm for a perturbation of 2.5%. (The discrepancy between the experiment and simulation is due to the convolution of the experimental data with a laser spot size of $\sim 2\,\mu$m). This suggests a robust method to tune the degree of evanescent coupling between the ring resonator and an adjoining bus waveguide, for instance, in an add-drop filter. The perturbation is dependent on the location of the triangular apertures forming the PhC. This is simple to control lithographically, unlike the case of devices that rely on fine tuning of the resonator-waveguide spacing.

In conclusion, we have created a GaAs spin Hall topological photonic ring resonator and used embedded InGaAs QDs to probe the mode structure of the device. Using spatially resolved PL measurements, we demonstrated that the modes were confined to the PhC interface. Furthermore, we showed that by controlling the perturbation of the PhC unit cell, the spatial confinement of the modes could be tuned. The resonator represents an important building block in the development of integrated photonic devices using embedded quantum emitters.

Data supporting this study are openly available from the University of Sheffield repository.[26]

This work was supported by EPSRC Grant No. EP/N031776/1.

REFERENCES

[1]C. P. Dietrich, A. Fiore, M. G. Thompson, M. Kamp, and S. Höfling, "GaAs integrated quantum photonics: Towards compact and multi-functional quantum photonic integrated circuits," Laser Photonics Rev. **10**, 870–894 (2016).
[2]M. C. Rechtsman, J. M. Zeuner, Y. Plotnik, Y. Lumer, D. Podolsky, F. Dreisow, S. Nolte, M. Segev, and A. Szameit, "Photonic Floquet topological insulators," Nature **496**, 196–200 (2013).
[3]S. Barik, H. Miyake, W. DeGottardi, E. Waks, and M. Hafezi, "Two-dimensionally confined topological edge states in photonic crystals," New J. Phys. **18**, 113013 (2016).
[4]S. Barik, A. Karasahin, C. Flower, T. Cai, H. Miyake, W. DeGottardi, M. Hafezi, and E. Waks, "A topological quantum optics interface," Science **359**, 666–668 (2018).
[5]Y. Yang, H. Jiang, and Z. H. Hang, "Topological valley transport in two-dimensional honeycomb photonic crystals," Sci. Rep. **8**, 1588 (2018).
[6]Y. Yang and Z. H. Hang, "Topological whispering gallery modes in two-dimensional photonic crystal cavities," Opt. Express **26**(16), 21235–21241 (2018).
[7]L.-H. Wu and X. Hu, "Scheme for achieving a topological photonic crystal by using dielectric material," Phys. Rev. Lett. **114**, 223901 (2015).
[8]A. B. Khanikaev and G. Shvets, "Two-dimensional topological photonics," Nat. Photonics **11**, 763–773 (2017).
[9]R. E. Christiansen, F. Wang, O. Sigmund, and S. Stobbe, "Designing photonic topological insulators with quantum-spin-Hall edge states using topology optimization," Nanophotonics **8**, 1363–1369 (2019).
[10]P. D. Anderson and G. Subramania, "Unidirectional edge states in topological honeycomb-lattice membrane photonic crystals," Opt. Express **25**, 23293 (2017).
[11]L. Lu, J. D. Joannopoulos, and M. Soljačić, "Topological photonics," Nat. Photonics **8**, 821–829 (2014).
[12]T. Ozawa, H. M. Price, A. Amo, N. Goldman, M. Hafezi, L. Lu, M. C. Rechtsman, D. Schuster, J. Simon, O. Zilberberg, and I. Carusotto, "Topological photonics," Rev. Mod. Phys. **91**, 015006 (2019).

Applied Physics Letters ARTICLE scitation.org/journal/apl

[13]X.-C. Sun and X. Hu, "Topological ring-cavity laser formed by honeycomb photonic crystals," preprint arXiv:1906.02464 (2019).
[14]T. Yamaguchi, Y. Ota, R. Katsumi, K. Watanabe, S. Ishida, A. Osada, Y. Arakawa, and S. Iwamoto, "GaAs valley photonic crystal waveguide with light-emitting InAs quantum dots," Appl. Phys. Express **12**, 062005 (2019).
[15]M. I. Shalaev, W. Walasik, A. Tsukernik, Y. Xu, and N. M. Litchinitser, "Robust topologically protected transport in photonic crystals at telecommunication wavelengths," Nat. Nanotechnol. **14**, 31–34 (2019).
[16]X.-T. He, E.-T. Liang, J.-J. Yuan, H.-Y. Qiu, X.-D. Chen, F.-L. Zhao, and J.-W. Dong, "A silicon-on-insulator slab for topological valley transport," Nat. Commun. **10**, 872 (2019).
[17]M. Hafezi, S. Mittal, J. Fan, A. Migdall, and J. M. Taylor, "Imaging topological edge states in silicon photonics," Nat. Photonics **7**, 1001 (2013).
[18]S. Barik, A. Karasahin, S. Mittal, E. Waks, and M. Hafezi, "Chiral quantum optics using a topological resonator," arXiv:1906.11263 (2019).
[19]M. Jalali Mehrabad, A. P. Foster, R. Dost, A. M. Fox, M. S. Skolnick, and L. R. Wilson, "Chiral topological photonics with an embedded quantum emitter," arXiv:1912.09943 (2019).
[20]P. Lodahl, S. Mahmoodian, S. Stobbe, A. Rauschenbeutel, P. Schneeweiss, J. Volz, H. Pichler, and P. Zoller, "Chiral quantum optics," Nature **541**, 473 (2017).
[21]See https://www.lumerical.com/products/ for "Lumerical Inc." (last accessed September 16, 2019).
[22]N. Parappurath, F. Alpeggiani, L. Kuipers, and E. Verhagen, "Direct observation of topological edge states in silicon photonic crystals: spin, dispersion, and chiral routing," arXiv:1811.10739 (2018).
[23]R. J. Coles, D. M. Price, J. E. Dixon, B. Royall, E. Clarke, P. Kok, M. S. Skolnick, A. M. Fox, and M. N. Makhonin, "Chirality of nanophotonic waveguide with embedded quantum emitter for unidirectional spin transfer," Nat. Commun. **7**, 11183 (2016).
[24]A. Javadi, D. Ding, M. H. Appel, S. Mahmoodian, M. C. Löbl, I. Söllner, R. Schott, C. Papon, T. Pregnolato, S. Stobbe, L. Midolo, T. Schröder, A. D. Wieck, A. Ludwig, R. J. Warburton, and P. Lodahl, "Spin-photon interface and spin-controlled photon switching in a nanobeam waveguide," Nat. Nanotechnol. **13**, 398–403 (2018).
[25]M. Fox, *Quantum Optics: An Introduction* (Oxford University Press, 2006).
[26]M. Jalali Mehrabad, dataset associated with "A semiconductor topological photonic ring resonator" (University of Sheffield Data Repository, 2020), https://doi.org/10.15131/shef.data.9944957.

Chapter 4

Chiral topological photonics with an embedded quantum emitter

1690 Vol. 7, No. 12 / December 2020 / Optica Research Article

optica

Chiral topological photonics with an embedded quantum emitter

Mahmoud Jalali Mehrabad,[1] Andrew P. Foster,[1,*] René Dost,[1] Edmund Clarke,[2] Pallavi K. Patil,[2] A. Mark Fox,[1] Maurice S. Skolnick,[1] and Luke R. Wilson[1]

[1]Department of Physics and Astronomy, University of Sheffield, Sheffield S3 7RH, UK
[2]EPSRC National Epitaxy Facility, University of Sheffield, Sheffield S1 4DE, UK
*Corresponding author: andrew.foster@sheffield.ac.uk

Received 16 March 2020; revised 23 October 2020; accepted 26 October 2020 (Doc. ID 393035); published 30 November 2020

Topological photonic interfaces support topologically nontrivial optical modes with helical character. When combined with an embedded quantum emitter that has a circularly polarized transition dipole moment, a chiral quantum optical interface is formed due to spin-momentum locking. Here, we experimentally realize such an interface by integrating semiconductor quantum dots into a valley-Hall topological photonic crystal waveguide. We harness the robust waveguide transport to create a ring resonator that supports helical modes. Chiral coupling of quantum dot transitions, with directional contrast as high as 75%, is demonstrated. The interface also supports a topologically trivial mode, comparison with which allows us to clearly demonstrate the protection afforded by topology to the nontrivial mode.

https://doi.org/10.1364/OPTICA.393035

1. INTRODUCTION

Nanophotonics concerns the confinement and manipulation of light at the nanoscale. A significant consequence of transverse optical confinement in waveguides at this scale is the presence of an elliptically polarized electric field, which carries spin angular momentum [1]. When a quantum emitter with a circularly polarized transition dipole moment is coupled to the waveguide, a chiral quantum light–matter interface can be realized, in which the photon spin and momentum are locked and photon–emitter interactions become direction-dependent. Such an interface has numerous potential applications, ranging from single-photon routers [2,3] to optical circulators [4] and isolators [5]. Further intriguing prospects include leveraging chirality in quantum spin networks [6] or for entanglement generation [7].

The chiral quantum optical interface was first demonstrated by coupling a semiconductor quantum dot (QD) to a dielectric nanobeam waveguide [8,9]. Subsequent developments extended capabilities to include atomic [10–12] and nanoparticle [13] quantum emitters. More recently, focus has returned to the on-chip nanophotonic platform, using single QDs coupled to dielectric waveguides [14–18]. A notable strength of such an approach lies in harnessing the tightly confined optical waveguide modes common to such a platform. This has the potential to enable highly efficient light–matter interactions at the single-photon level [19,20] and is therefore of great interest for chiral quantum optics applications.

A concurrent development has been the rise of topological photonics as a new paradigm in nanophotonics research [21–25]. Topological photonic interfaces are formed at the boundary between topologically distinct photonic crystals (PhCs) and support the transport of light in counterpropagating waveguide modes that have helical character [26]. This naturally suggests the possibility of a chiral topological photonic interface; the first such device was recently demonstrated using a QD coupled to a spin-Hall topological PhC waveguide [18]. A particularly appealing property of topological waveguides is their predicted robustness against tight bends and certain defects [21], which is attractive for the formation of low-loss, compact photonic elements. As an example, one could augment a chiral ring resonator [27,28] with topological protection, an exciting prospect that would enable chiral coupling with enhanced light–matter interaction strength in a topologically protected system.

It is critical in nanophotonic design that waveguides restrict radiative coupling to free-space modes, which is a notable limitation of recently reported spin-Hall topological waveguides interfaced with QDs [18,29,30]. This can be addressed by instead considering the valley-Hall topological photonic interface, for which the interface modes lie below the light line [31,32]. Here, we realize a chiral quantum optical interface using semiconductor QDs embedded in a valley-Hall topological PhC waveguide. Chiral coupling of single QDs to the nontrivial waveguide mode is demonstrated, with a spin-dependent, averaged directional contrast of up to 0.75 ± 0.02 measured. We investigate the propagation of light around tight bends in the topological interface by creating a compact ring resonator device. Q factors of up to 4000

2334-2536/20/121690-07 Journal © 2020 Optical Society of America

Research Article Vol. 7, No. 12 / December 2020 / Optica 1691

(125,000) are measured (simulated) for a resonator with a circumference of less than 17 μm. Finally, we couple the resonator to a bus waveguide, which enables us to demonstrate chiral coupling of a QD located within the resonator. In addition to a topologically nontrivial mode, the interface also supports a trivial mode, comparison with which enables a clear visualization of the power of topological protection in the device.

2. TOPOLOGICAL WAVEGUIDE DESIGN

Our valley-Hall topological PhC is formed from a honeycomb lattice of circular holes in a dielectric membrane, with the rhombic unit cell of the PhC comprising a pair of holes [see Fig. 1(a)]. Considering first the case of equivalent diameter holes, we plot in Fig. 1(b) the band structure of the PhC for TE polarization, revealing a Dirac cone at the K point (and equivalently at the K' point, not shown). The band structure was calculated using the freely available MPB software package [33]. Next, we shrink one hole and expand the other, and show that the resulting PhC supports a bandgap for TE-polarized light [dashed lines in Fig. 1(b)]. A key feature of the band structure is the opposite sign of the Berry curvature at the K and K' points, as demonstrated in Ref. [32]. At an interface created by an inversion of the rhombic unit cells on one side of the PhC, the difference in Berry curvature leads to the confinement at the interface of counterpropagating edge states with opposing helicity [32]. The band structure of such a waveguide, formed with a bearded interface, is shown in Fig. 1(c). The interface supports two modes, labeled T and NT, and is single mode between ∼925 nm − 986 nm (region T) and ∼1008 nm − 1028 nm (region NT). In the multimode region in which the two modes overlap (∼986 nm − 1008 nm), the bands flatten and slow light is predicted [34]. Using the approach of Ref. [35], we gradually increase the size of the small holes on one side of the interface, transforming the bearded interface into a zigzag interface, consisting of two large holes facing one another. During this transformation, we find that mode NT is always present in the bandgap, whereas mode T disappears (see Supplement 1). We also observe in simulations that mode NT propagates smoothly around corners, while mode T is prone to backscatter [see Figs. 1(f)–1(g) and Figs. 3(c)–3(d). We therefore conclude that mode NT (T) is topologically nontrivial (trivial).

Using finite-difference time-domain (FDTD) simulations [36] we show in Fig. 1(d) that the normalized transmission for a 10-μm-long section of the waveguide is approximately unity across the full spectral window covered by modes T and NT. A clear difference is observed, however, when waveguide bends are introduced. In Figs. 1(e)–1(g), we show the simulated transmission of light through a waveguide containing four 120-deg bends.

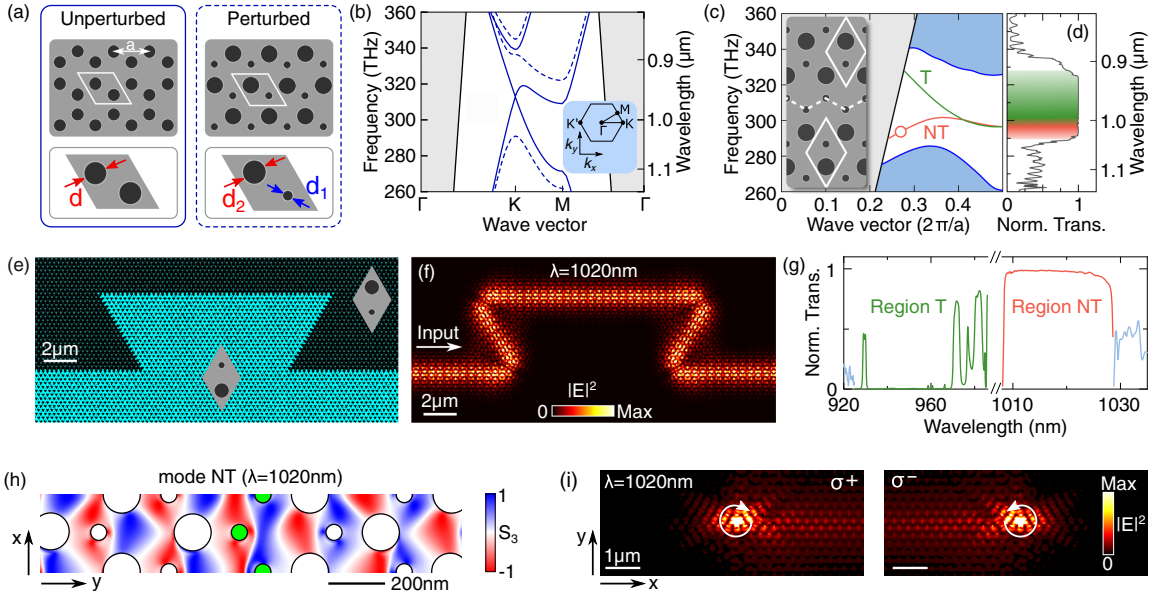

Fig. 1. (a) Schematic of a (left) unperturbed and (right) perturbed honeycomb lattice, formed from air holes in a thin dielectric membrane. The rhombic unit cell, comprising two holes, is outlined below in each case. (b) Band diagram for a honeycomb PhC formed using an unperturbed (solid lines) or perturbed (dashed lines) unit cell of the type shown in (a), in a 170 nm-thick membrane (dielectric constant $\epsilon = 11.6$). The inset shows the first Brillouin zone of the PhC. Hole diameters are $d = 97$ nm, $d_1 = 56$ nm, and $d_2 = 125$ nm. The pitch of the PhC in each case is $a = 266$ nm. (c) Projected band diagram for the interface between topologically distinct perturbed PhCs (see schematic in inset, with the interface denoted by a dashed line); hole sizes are the same as in (b). The interface supports two modes, labeled T (topologically trivial; see text) and NT (nontrivial). (d) FDTD-simulated normalized transmission coefficient (Norm. Trans.) for a 10 μm length of the interface. (e) Schematic of a waveguide containing four 120-deg bends. Regions of opposite unit cell orientation are shaded light and dark, respectively. (f) Simulated time-averaged electric field intensity in the plane of the waveguide for mode NT ($\lambda = 1020$ nm), when light is injected from the left; (g) normalized transmission through the waveguide in (f), color-coded by spectral window [c.f. (c)]. The abscissa break corresponds to the multimode region of the waveguide dispersion (∼986 nm − 1008 nm), which is not considered here. (h) Position-dependence of the normalized Stokes S_3 parameter at the interface, evaluated for mode NT at $\lambda = 1020$ nm [red circle in (c)]. Circles represent the holes of the PhC. Those with green fill show the position of the holes at the interface. Note that the waveguide is rotated 90 deg compared to the schematic in (c). (i) Time-averaged electric field intensity resulting from a (left) σ^+ or (right) σ^- circularly polarized dipole ($\lambda = 1020$ nm) placed at a chiral point of the waveguide corresponding to (left) $S_3 \sim 1$ or (right) $S_3 \sim -1$.

Research Article Vol. 7, No. 12 / December 2020 / Optica 1692

Transmission of the topologically protected nontrivial mode is near unity within region NT. In contrast, transmission within region T is both significantly less than unity and wavelength-dependent, due to backscatter of the trivial mode at each corner. This provides direct evidence of the topological protection afforded to mode NT.

Next, we demonstrate the potential of mode NT to form a chiral quantum optical interface. We evaluate the Stokes S_3 parameter (degree of circular polarization) in the vicinity of the interface using FDTD simulations, revealing large areas in which $|S_3| \to 1$ [see Fig. 1(h)]. Then, we position a circularly polarized dipole source at a point of maximum chirality ($|S_3| \sim 1$) and monitor the waveguide transmission [Fig. 1(i)]. Unidirectional emission with a direction dependent on the dipole polarization is clearly predicted. Note that the same holds true for the trivial mode, in that case due to the breaking of mirror symmetry in the waveguide (see Supplement 1).

3. EXPERIMENTAL RESULTS

A. Waveguide Operation and Chiral Coupling

Topological PhC devices are fabricated in a nominally 170-nm-thick GaAs $p-i-n$ membrane, which contains a layer of embedded InGaAs QDs. A scanning electron microscope (SEM) image of a representative topological waveguide is shown in Fig. 2(a). The waveguide is coupled at either end to nanobeam waveguides, which are terminated with grating outcouplers (OCs) to enable coupling of light to and from free space. Simulations show that the nanobeam–topological waveguide interface is efficient in region T (>87% transmission) but limited to an average of 31% transmission in region NT (see Supplement 1), likely due to spatial mismatch between mode NT and the fundamental nanobeam TE mode. This is sufficient for optical readout of mode NT in the present experiment. It remains an outstanding challenge to create a highly efficient interface between trivial and topological waveguides, but encouraging progress has been reported elsewhere [32].

To demonstrate confinement of the optical mode at the topological interface, we collect photoluminescence (PL) from one OC while rastering the excitation laser across the device. After integrating the PL intensity spectrally over region NT, we show the signal as a function of excitation position in Fig. 2(b), revealing that transmission of QD PL only occurs when the QD is in close proximity to the interface. Furthermore, we subsequently show (see Supplement 1) that QDs at the interface emit single photons and can be electrically Stark-tuned to control the wavelength of individual QD transitions. The latter is of particular interest for extending recent demonstrations of few-QD interactions in waveguide quantum electrodynamics [37,38] to the chiral regime supported by topological interfaces.

Next, we probe the helicity intrinsic to the topologically nontrivial mode by investigating chiral coupling of QDs located at the interface. We first spectrally locate region NT of the waveguide under investigation (see Supplement 1). QDs emitting spectrally within this region are then optically excited in the presence of a magnetic field, which is applied in the Faraday geometry (normal to the sample plane). At the same time, PL is collected from both OCs. The magnetic field lifts the degeneracy of QD transitions via the Zeeman effect, allowing PL emission from states with opposite circular polarization to be spectrally resolved [see Fig. 2(c), for the case of a neutral exciton]. The chiral contrast (C) is then evaluated independently for emission from either OC using the expression [14] $C = (I_{\sigma+} - I_{\sigma-})/(I_{\sigma+} + I_{\sigma-})$, where $I_{\sigma+}$ and $I_{\sigma-}$ refer to the PL intensity for σ^+ and σ^- polarized emission, respectively. By considering each OC separately, any variance in collection efficiency is negated [17].

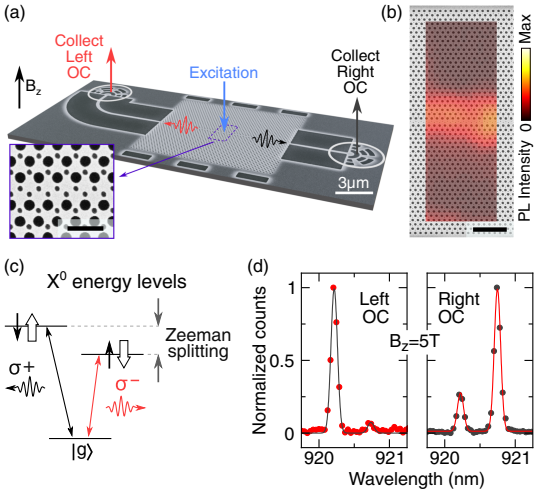

Fig. 2. (a) SEM image of a topological waveguide. A higher magnification image of the interface is shown in the inset (scale bar 500 nm). (b) PL intensity collected from one OC and integrated spectrally over region NT as a function of the excitation position on the waveguide. The resulting map is overlaid on an SEM image of the device (scale bar 2 μm). The spatial resolution is limited by that of our optical microscope (∼2 μm). (c) Energy levels for the X_0 (neutral) exciton under nonzero magnetic field; (d) normalized PL spectra at $B_z = 5$ T for a QD coupled chirally to mode NT, with a chiral contrast of 0.92 ± 0.02 (0.57 ± 0.03) measured from the left (right) OC, respectively. Solid lines are the result of Gaussian fitting to the data (points).

The resulting PL spectra for the emission from a single representative QD, for a magnetic field of B = 5 T, are shown in Fig. 2(d). Two Zeeman-split states are observed, with asymmetric intensity for the σ^+ and σ^- polarized transitions. The asymmetry in the intensities is seen to reverse when PL is collected from the other OC. The emission is therefore directional, with the intensity dependent on the handedness of the circular polarization of the emitter (i.e., chiral coupling). The chiral contrast is as high as 0.92 ± 0.02 measured from the left OC. The contrast measured at the right OC is 0.57 ± 0.03, giving an average contrast of 0.75 ± 0.02. Asymmetry in the contrast measured in either direction is commonly observed in experiments such as this, an effect which as yet is not fully understood. Due to spatial symmetry-breaking, chiral coupling is also observed for QDs coupled to trivial mode T (see Supplement 1).

B. Chiral Topological Ring Resonator

The combination of chiral coupling and an enhanced light–matter interaction strength is appealing for quantum optical device applications [27,28,39]. With this in mind, we now leverage the topological protection of mode NT against scattering at tight bends to create a compact photonic ring resonator and demonstrate chiral coupling of a QD embedded within the device. The

Research Article Vol. 7, No. 12 / December 2020 / Optica 1693

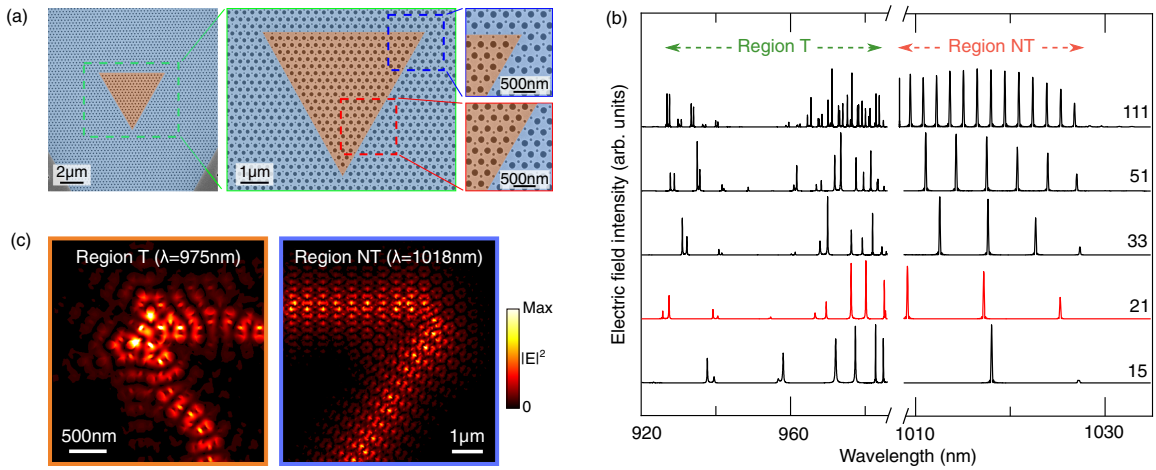

Fig. 3. (a) False-color SEM images of a topological resonator, the center of which is shaded orange. (b) Simulated longitudinal mode spectra as a function of resonator side length (spectra offset for clarity and labeled with the number of unit cells per side). The trace in red (21 unit cell side length) corresponds to the resonator size shown in (a). The abscissa break covers the multimode region of the waveguide dispersion. (c) Electric field intensity spatial profile in the corner of a resonator for (left) region T (975 nm) and (right) region NT (1018 nm).

resonator takes the form of a triangle with three 120-deg corners [see Fig. 3(a)] and is created by embedding a triangular array of rhombic unit cells inside a larger array of inverted unit cells.

We first investigate the optical characteristics of the resonator using FDTD simulations. Longitudinal mode spectra as a function of the resonator side length are shown in Fig. 3(b). A clear distinction is seen in the resonator behavior within the topologically nontrivial region NT and the trivial region T. In the latter, the longitudinal modes are split into multiple closely spaced resonances, which furthermore are strongly suppressed in the middle of the spectral range. These effects can both be understood as originating from backscattering of the trivial mode at the resonator corners. Simulation of a single 120-deg corner reveals a transmission minimum (i.e., strong backscatter) at ∼950 nm, resulting in the suppression of the resonator modes (see Supplement 1). The simulated resonator mode quality factors (Q factors) for region T are limited by backscatter, with a maximum value less than 10,000 obtained for a device with a side length of ∼5.5 μm (21 unit cells).

The spectrum corresponding to the nontrivial region NT stands in stark contrast. Here, the single corner transmission approaches unity across the full bandwidth. This finding is supported by a simulation of the mode profile in region NT, in which the corner is seen to be smoothly navigated, unlike the case in region T [see Fig. 3(c)]. The mode spacing in region NT reduces with increasing resonator size, characteristic of a ring-type resonator. For the device with a side length of 21 unit cells, the Q factor is as high as 125,000, an order of magnitude improvement on the trivial case. (Note that a simulated Q factor of greater than one million is obtained for a resonator with a side length of 111 unit cells.) This is direct evidence of the topological protection granted to mode NT.

Experimentally, we consider a resonator with a side length of 21 unit cells. We nonresonantly excite the ensemble of QDs on one side of the resonator at high power, creating a broadband internal light source, and collect PL emitted from the same location. A representative PL spectrum is shown in Fig. 4(a). The discrete modes of the resonator can be clearly resolved in both regions T and NT. The modes are observed at a shorter wavelength than that predicted by simulation, most likely due to an increase in fabricated hole sizes compared with design. Q factors up to ∼2700 (∼4000) are measured in region T (NT). Higher Q factors in region NT compared to those in region T are consistent with topological protection of the former. The measured Q factors are considerably lower than those determined using simulations. This is commonly observed for GaAs devices operating in the 900–950 nm wavelength range and is likely due in part to surface-state-related absorption losses against which there is no topological protection. Surface passivation approaches have been shown to help mitigate this effect in GaAs PhC devices [40].

We demonstrate confinement of the modes at the resonator interface by collecting PL emission from one corner of the resonator, while rastering the excitation laser across the device. At each excitation position, the PL spectrum is integrated over two different bandwidths corresponding to single longitudinal modes in regions T and NT, respectively. The resulting spatially resolved PL maps are shown in Fig. 4(b), accompanied by simulated mode profiles. Correspondence between experiment and simulation is most easily seen by examining the corners of the resonator. In region T, strong scattering is predicted by simulation at the resonator corners, and the resulting experimental PL map reveals the distinct triangular shape of the full waveguide. In contrast, simulation shows that in region NT, scattering is suppressed at the resonator corners (see Supplement 1). This effect can be seen clearly in the corresponding PL map, in which scattering at the resonator corners is very weak. To show that the mode spectra are consistent across the device, we plot in Fig. 4(c) the PL spectrum acquired at the midpoint of each side of the resonator in region NT. The similarity in the spectra confirms that the mode is distributed along the interface.

Finally, we couple the topological resonator to an adjacent bus waveguide [see Fig. 5(a)]. This enables us to demonstrate chiral coupling of a QD located within the resonator. (Similar coupling to a bus waveguide has been reported recently by Barik

Research Article Vol. 7, No. 12 / December 2020 / Optica 1694

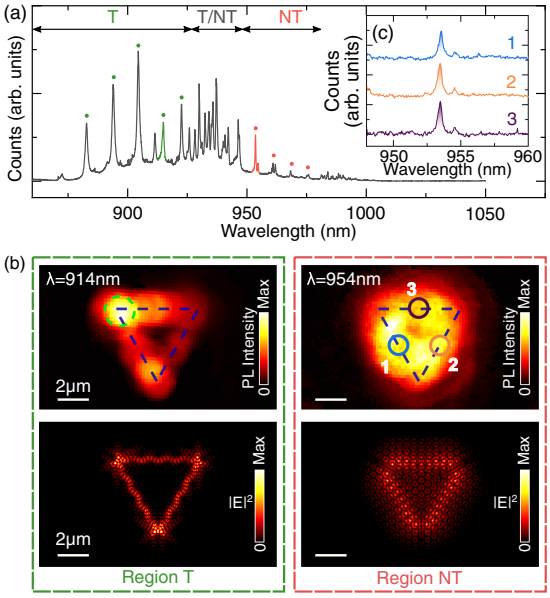

Fig. 4. (a) PL spectrum measured from above the resonator, with longitudinal modes visible (indicated in regions T and NT by filled circles). The different regions of the interface mode structure (T, T/NT, and NT) are labeled. (b) (Upper panels) Spatially resolved, integrated PL for two different modes of the same resonator, for wavelengths corresponding to regions T and NT, respectively [color-coded in (a)]. PL was collected from the top left corner of the resonator (green dashed circle in the left-hand panel). The excitation spot size was ∼2 μm. (Lower panels) Simulated electric field intensity spatial profiles for modes in the same regions of the band structure considered in experiment. (c) PL spectra for a single longitudinal mode of the resonator in region NT, acquired at the midpoint of each of the three sides of the resonator, respectively [as labeled in (b)]. The background has been removed from each of the spectra, which are offset for clarity.

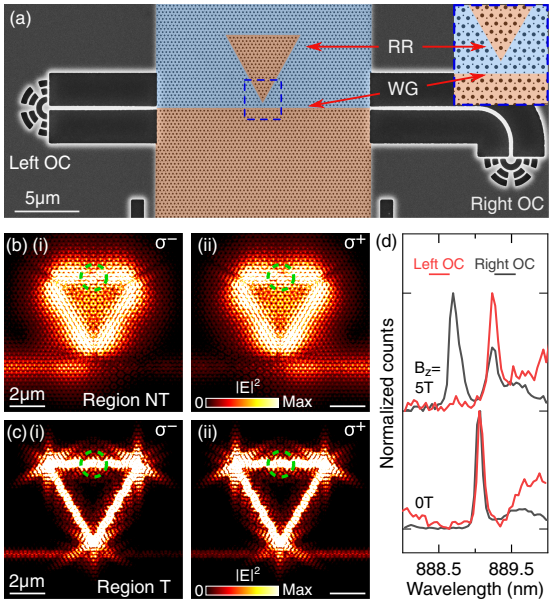

Fig. 5. (a) False-color SEM image of a representative ring resonator (RR) coupled to a bus waveguide (WG), with nanobeam waveguides at either end. The inset shows a schematic of the RR–WG interface (dashed blue region in the SEM image). (b) FDTD simulated electric field intensity in the plane of the device for a (i) σ^- and (ii) σ^+ polarized dipole source, located at a chiral point on the ring resonator interface (dashed green circle). The dipole emission wavelength corresponds to region NT of the waveguide dispersion. The color scale is saturated to increase the visibility of the waveguide-coupled emission. (c) Same as in (b), but for an emission wavelength corresponding to mode T; (d) low power, normalized PL spectra as a function of applied magnetic field when the resonator is excited from above and PL is collected independently from both OCs. A single chirally coupled transition can be seen, with chiral contrast of 0.93 ± 0.07 (0.54 ± 0.06) from the left (right) OC. The emission wavelength corresponds to region NT. The shorter wavelength compared with elsewhere in the paper is due to larger hole sizes in this device.

et al. [41].) We first use FDTD simulations to demonstrate the principle of operation of the device. A circularly polarized dipole is positioned at a highly chiral point on the resonator interface, such that it emits unidirectionally. The optical field in the resonator subsequently couples evanescently to the bus waveguide. In the case of a wavelength within region NT, the direction of emission into the waveguide is seen to depend on the handedness of the dipole polarization [Fig. 5(b)], therefore enabling readout of the chiral contrast. For the trivial mode T, this technique is hindered by backscatter at the resonator corners, and the maximum chiral contrast that can be measured is therefore reduced [Fig. 5(c)]. We also find the chirality in this case to be sensitive to the position of the dipole along the interface (even when still positioned at one of the many highly chiral positions), unlike for the topologically protected mode NT. Experimentally, we excite QDs located at the resonator interface at low power and measure the PL signal from the OCs at either end of the bus waveguide. Chiral coupling is shown in Fig. 5(d) for a QD transition at a wavelength corresponding to mode NT of the waveguide dispersion. The transition exhibits an average chiral contrast of 0.74 ± 0.06, demonstrating promising chiral characteristics for a topologically protected ring resonator mode.

4. CONCLUSION

We have demonstrated a chiral quantum optical interface using semiconductor QDs embedded in a valley-Hall topological waveguide. An average chiral contrast of up to 0.75 was measured for a QD coupled to a topologically nontrivial mode confined to the interface. Propagation of light around tight bends in the waveguide was subsequently demonstrated by fabrication of a topological photonic ring resonator, the modes of which have simulated Q factors up to 125,000 (experimental values up to 4000). Coupling of the structure to a bus waveguide enabled the observation of chiral coupling of a QD within the resonator. Comparison with a topologically trivial mode in the same waveguide enabled us to clearly highlight the benefits of the topological protection that is afforded to the nontrivial mode.

The topological nanophotonic platform demonstrated here has significant potential to form the basis of scalable chiral quantum optical circuits protected against backscatter. Combining our approach with either QD registration [14,42–44] or site-controlled growth [45,46] techniques would enable deterministic positioning of QDs at highly chiral points in the waveguide,

addressing the scalability challenge. Furthermore, the chiral nature of the interface allows for the realization of separation-independent QD–QD interactions [1,7], in contrast to the nonchiral case. Exciting future prospects include the realization of superradiant many-body states [38,47] and the formation of large-scale chiral spin networks [6] using a topologically protected photonic platform.

Data supporting this publication can be freely downloaded from the University of Sheffield Research Data Repository at [48] under the terms of the Creative Commons Attribution (CC-BY) license.

Funding. Engineering and Physical Sciences Research Council (EP/N031776/1).

Acknowledgment. The authors would like to thank David Whittaker for valuable discussions. M. J. M. designed the photonic structures, which were fabricated by R. D. E. C. and P. K. P. grew the sample. M. J. M. and A. P. F. carried out the measurements and simulations. L. R. W., M. S. S., and A. M. F. provided supervision and expertise. A. P. F. wrote the paper, with input from all authors.

Disclosures. The authors declare no conflicts of interest.

See Supplement 1 for supporting content.

REFERENCES AND NOTES

1. P. Lodahl, S. Mahmoodian, S. Stobbe, A. Rauschenbeutel, P. Schneeweiss, J. Volz, H. Pichler, and P. Zoller, "Chiral quantum optics," Nature **541**, 473–480 (2017).
2. C. Gonzalez-Ballestero, E. Moreno, F. J. Garcia-Vidal, and A. Gonzalez-Tudela, "Nonreciprocal few-photon routing schemes based on chiral waveguide-emitter couplings," Phys. Rev. A **94**, 063817 (2016).
3. C.-H. Yan, Y. Li, H. Yuan, and L. F. Wei, "Targeted photonic routers with chiral photon-atom interactions," Phys. Rev. A **97**, 023821 (2018).
4. M. Scheucher, A. Hilico, E. Will, J. Volz, and A. Rauschenbeutel, "Quantum optical circulator controlled by a single chirally coupled atom," Science **354**, 1577–1580 (2016).
5. K. Xia, G. Lu, G. Lin, Y. Cheng, Y. Niu, S. Gong, and J. Twamley, "Reversible nonmagnetic single-photon isolation using unbalanced quantum coupling," Phys. Rev. A **90**, 043802 (2014).
6. H. Pichler, T. Ramos, A. J. Daley, and P. Zoller, "Quantum optics of chiral spin networks," Phys. Rev. A **91**, 042116 (2015).
7. C. Gonzalez-Ballestero, A. Gonzalez-Tudela, F. J. Garcia-Vidal, and E. Moreno, "Chiral route to spontaneous entanglement generation," Phys. Rev. B **92**, 155304 (2015).
8. I. J. Luxmoore, N. A. Wasley, A. J. Ramsay, A. C. T. Thijssen, R. Oulton, M. Hugues, S. Kasture, V. G. Achanta, A. M. Fox, and M. S. Skolnick, "Interfacing spins in an InGaAs quantum dot to a semiconductor waveguide circuit using emitted photons," Phys. Rev. Lett. **110**, 037402 (2013).
9. I. J. Luxmoore, N. A. Wasley, A. J. Ramsay, A. C. T. Thijssen, R. Oulton, M. Hugues, A. M. Fox, and M. S. Skolnick, "Optical control of the emission direction of a quantum dot," Appl. Phys. Lett. **103**, 241102 (2013).
10. C. Junge, D. O'Shea, J. Volz, and A. Rauschenbeutel, "Strong coupling between single atoms and nontransversal photons," Phys. Rev. Lett. **110**, 213604 (2013).
11. R. Mitsch, C. Sayrin, B. Albrecht, P. Schneeweiss, and A. Rauschenbeutel, "Quantum state-controlled directional spontaneous emission of photons into a nanophotonic waveguide," Nat. Commun. **5**, 5713 (2014).
12. I. Shomroni, S. Rosenblum, Y. Lovsky, O. Bechler, G. Guendelman, and B. Dayan, "All-optical routing of single photons by a one-atom switch controlled by a single photon," Science **345**, 903–906 (2014).
13. J. Petersen, J. Volz, and A. Rauschenbeutel, "Chiral nanophotonic waveguide interface based on spin-orbit interaction of light," Science **346**, 67–71 (2014).
14. R. J. Coles, D. M. Price, J. E. Dixon, B. Royall, E. Clarke, P. Kok, M. S. Skolnick, A. M. Fox, and M. N. Makhonin, "Chirality of nanophotonic waveguide with embedded quantum emitter for unidirectional spin transfer," Nat. Commun. **7**, 11183 (2016).
15. R. J. Coles, D. M. Price, B. Royall, E. Clarke, M. S. Skolnick, A. M. Fox, and M. N. Makhonin, "Path-dependent initialization of a single quantum dot exciton spin in a nanophotonic waveguide," Phys. Rev. B **95**, 121401 (2017).
16. P. Mrowiński, P. Schnauber, P. Gutsche, A. Kaganskiy, J. Schall, S. Burger, S. Rodt, and S. Reitzenstein, "Directional emission of a deterministically fabricated quantum dot–Bragg reflection multimode waveguide system," ACS Photon. **6**, 2231–2237 (2019).
17. I. Söllner, S. Mahmoodian, S. L. Hansen, L. Midolo, A. Javadi, G. Kirsanske, T. Pregnolato, H. El-Ella, E. H. Lee, J. D. Song, S. Stobbe, and P. Lodahl, "Deterministic photon-emitter coupling in chiral photonic circuits," Nat. Nanotechnol. **10**, 775–778 (2015).
18. S. Barik, A. Karasahin, C. Flower, T. Cai, H. Miyake, W. DeGottardi, M. Hafezi, and E. Waks, "A topological quantum optics interface," Science **359**, 666–668 (2018).
19. M. Arcari, I. Söllner, A. Javadi, S. Lindskov Hansen, S. Mahmoodian, J. Liu, H. Thyrrestrup, E. H. Lee, J. D. Song, S. Stobbe, and P. Lodahl, "Near-unity coupling efficiency of a quantum emitter to a photonic crystal waveguide," Phys. Rev. Lett. **113**, 093603 (2014).
20. L. Scarpelli, B. Lang, F. Masia, D. M. Beggs, E. A. Muljarov, A. B. Young, R. Oulton, M. Kamp, S. Höfling, C. Schneider, and W. Langbein, "99% beta factor and directional coupling of quantum dots to fast light in photonic crystal waveguides determined by spectral imaging," Phys. Rev. B **100**, 035311 (2019).
21. F. D. M. Haldane and S. Raghu, "Possible realization of directional optical waveguides in photonic crystals with broken time-reversal symmetry," Phys. Rev. Lett. **100**, 013904 (2008).
22. M. Hafezi, S. Mittal, J. Fan, A. Migdall, and J. M. Taylor, "Imaging topological edge states in silicon photonics," Nat. Photonics **7**, 1001–1005 (2013).
23. M. C. Rechtsman, J. M. Zeuner, Y. Plotnik, Y. Lumer, D. Podolsky, F. Dreisow, S. Nolte, M. Segev, and A. Szameit, "Photonic Floquet topological insulators," Nature **496**, 196–200 (2013).
24. T. Ozawa, H. M. Price, A. Amo, N. Goldman, M. Hafezi, L. Lu, M. C. Rechtsman, D. Schuster, J. Simon, O. Zilberberg, and I. Carusotto, "Topological photonics," Rev. Mod. Phys. **91**, 015006 (2019).
25. O. Yasutomo, T. Kenta, O. Tomoki, A. Alberto, J. Zhetao, K. Boubacar, N. Masaya, A. Yasuhiko, and I. Satoshi, "Active topological photonics," Nanophotonics **9**, 547–567 (2020).
26. L.-H. Wu and X. Hu, "Scheme for achieving a topological photonic crystal by using dielectric material," Phys. Rev. Lett. **114**, 223901 (2015).
27. D. Martin-Cano, H. R. Haakh, and N. Rotenberg, "Chiral emission into nanophotonic resonators," ACS Photon. **6**, 961–966 (2019).
28. L. Tang, J. Tang, W. Zhang, G. Lu, H. Zhang, Y. Zhang, K. Xia, and M. Xiao, "On-chip chiral single-photon interface: isolation and unidirectional emission," Phys. Rev. A **99**, 043833 (2019).
29. M. J. Mehrabad, A. P. Foster, R. Dost, E. Clarke, P. K. Patil, I. Farrer, J. Heffernan, M. S. Skolnick, and L. R. Wilson, "A semiconductor topological photonic ring resonator," Appl. Phys. Lett. **116**, 061102 (2020).
30. E. Sauer, J. P. Vasco, and S. Hughes, "Theory of intrinsic propagation losses in topological edge states of planar photonic crystals," Phys. Rev. Res. **2**, 043109 (2020).
31. M. I. Shalaev, W. Walasik, A. Tsukernik, Y. Xu, and N. M. Litchinitser, "Robust topologically protected transport in photonic crystals at telecommunication wavelengths," Nat. Nanotechnol. **14**, 31–34 (2019).
32. X.-T. He, E.-T. Liang, J.-J. Yuan, H.-Y. Qiu, X.-D. Chen, F.-L. Zhao, and J.-W. Dong, "A silicon-on-insulator slab for topological valley transport," Nat. Commun. **10**, 872 (2019).
33. S. G. Johnson and J. D. Joannopoulos, "Block-iterative frequency-domain methods for Maxwell's equations in a planewave basis," Opt. Express **8**, 173–190 (2001).
34. During review of this article, it was shown elsewhere [35] that replacing the circular holes of the unit cell with triangles allows for single-mode topological slow light.
35. H. Yoshimi, T. Yamaguchi, Y. Ota, Y. Arakawa, and S. Iwamoto, "Slow light waveguides in topological valley photonic crystals," Opt. Lett. **45**, 2648–2651 (2020).
36. ANSYS Lumerical, 2019, https://www.lumerical.com/products/.

Research Article Vol. 7, No. 12 / December 2020 / Optica 1696

37. J.-H. Kim, S. Aghaeimeibodi, C. J. K. Richardson, R. P. Leavitt, and E. Waks, "Super-radiant emission from quantum dots in a nanophotonic waveguide," Nano Lett. **18**, 4734–4740 (2018).
38. J. Q. Grim, A. S. Bracker, M. Zalalutdinov, S. G. Carter, A. C. Kozen, M. Kim, C. S. Kim, J. T. Mlack, M. Yakes, B. Lee, and D. Gammon, "Scalable in operando strain tuning in nanophotonic waveguides enabling three-quantum-dot superradiance," Nat. Mater. **18**, 963–969 (2019).
39. S. Mahmoodian, K. Prindal-Nielsen, I. Söllner, S. Stobbe, and P. Lodahl, "Engineering chiral light-matter interaction in photonic crystal waveguides with slow light," Opt. Mater. Express **7**, 43–51 (2017).
40. K. Kuruma, Y. Ota, M. Kakuda, S. Iwamoto, and Y. Arakawa, "Surface-passivated high-Q GaAs photonic crystal nanocavity with quantum dots," APL Photon. **5**, 046106 (2020).
41. S. Barik, A. Karasahin, S. Mittal, E. Waks, and M. Hafezi, "Chiral quantum optics using a topological resonator," Phys. Rev. B **101**, 205303 (2020).
42. L. Sapienza, M. Davanço, A. Badolato, and K. Srinivasan, "Nanoscale optical positioning of single quantum dots for bright and pure single-photon emission," Nat. Commun. **6**, 7833 (2015).
43. P. Schnauber, J. Schall, S. Bounouar, T. Höhne, S.-I. Park, G.-H. Ryu, T. Heindel, S. Burger, J.-D. Song, S. Rodt, and S. Reitzenstein, "Deterministic integration of quantum dots into on-chip multimode interference beamsplitters using in situ electron beam lithography," Nano Lett. **18**, 2336–2342 (2018).
44. T. Pregnolato, X.-L. Chu, T. Schröder, R. Schott, A. D. Wieck, A. Ludwig, P. Lodahl, and N. Rotenberg, "Deterministic positioning of quantum dots in nanophotonic waveguides," APL Photonics **5**, 086101 (2020).
45. M. Strauß, A. Kaganskiy, R. Voigt, P. Schnauber, J.-H. Schulze, S. Rodt, A. Strittmatter, and S. Reitzenstein, "Resonance fluorescence of a site-controlled quantum dot realized by the buried-stressor growth technique," Appl. Phys. Lett. **110**, 111101 (2017).
46. K. D. Jöns, P. Atkinson, M. Müller, M. Heldmaier, S. M. Ulrich, O. G. Schmidt, and P. Michler, "Triggered indistinguishable single photons with narrow line widths from site-controlled quantum dots," Nano Lett. **13**, 126–130 (2013).
47. D. F. Kornovan, M. I. Petrov, and I. V. Iorsh, "Transport and collective radiance in a basic quantum chiral optical model," Phys. Rev. B **96**, 115162 (2017).
48. M. Jalali Mehrabad, A. P. Foster, R. Dost, E. Clarke, P. K. Patil, M. S. Skolnick, and L. R. Wilson, University of Sheffield Research Data Repository, 2020, http://dx.doi.org/10.15131/shef.data.11968089.

Supplemental Document

Chiral topological photonics with an embedded quantum emitter: supplement

Mahmoud Jalali Mehrabad,[1] Andrew P. Foster,[1,*] René Dost,[1] Edmund Clarke,[2] Pallavi K. Patil,[2] A. Mark Fox,[1] Maurice S. Skolnick,[1] and Luke R. Wilson[1]

[1] *Department of Physics and Astronomy, University of Sheffield, Sheffield S3 7RH, UK*
[2] *EPSRC National Epitaxy Facility, University of Sheffield, Sheffield S1 4DE, UK*
[*] *Corresponding author:* *andrew.foster@sheffield.ac.uk*

Supplement DOI: https://doi.org/10.6084/m9.figshare.13176920

Parent Article DOI: https://doi.org/10.1364/OPTICA.393035

Chiral topological photonics with an embedded quantum emitter

Additional simulation and experimental results in support of the paper "Chiral topological photonics with an embedded quantum emitter'.

1. DETERMINATION OF THE TOPOLOGICALLY TRIVIAL OR NON-TRIVIAL CHARACTER OF MODES T AND NT.

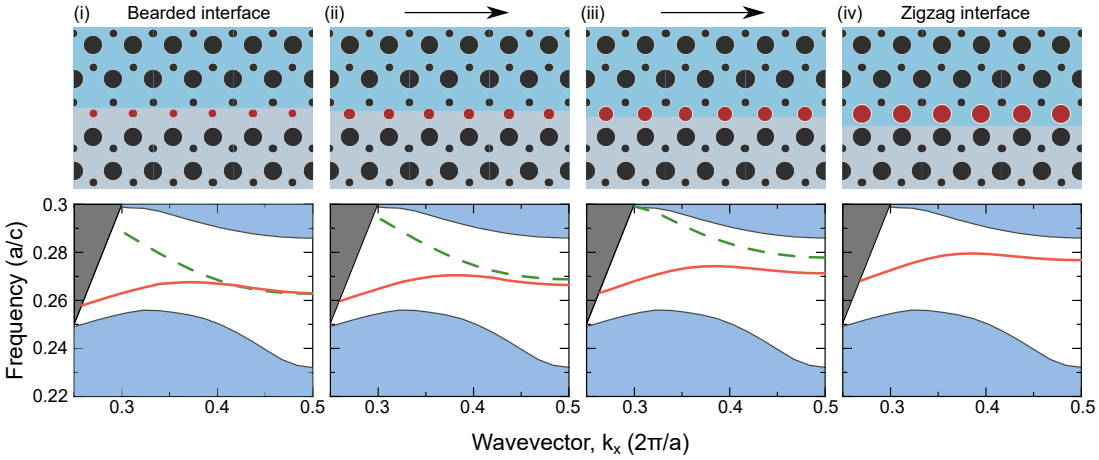

Fig. S1. Projected band structures (bottom) as the topological waveguide interface is changed continuously from (i) bearded type with small circles at the interface to (iv) zigzag type with large circles at the interface (see schematics at top). Blue and grey highlighted regions represent modes in the bulk and above the light cone, respectively. The lattice pitch is given by a and c is the speed of light. The radius r of one row of holes (coloured red) varies as (i) r=0.21a (ii) r=0.29a (iii) r=0.38a (iv) r=0.47a, to enable a smooth transition between the two interfaces. The radii of the other holes remain unchanged at r=0.21a and r=0.47a for the small and large holes, respectively. As the bulk photonic crystal remains unchanged during the transition from (i) to (iv), we expect that a single topologically non-trivial mode should be seen in both cases (i) and (iv). A single mode (orange solid line) is indeed always observed at the interface, and we therefore conclude that this is the topologically non-trivial mode [1]. A second mode (green dashed line) is seen to disappear as the interface is changed from (i) to (iv), which we ascribe to a topologically trivial mode. The assignment of trivial or non-trivial character is supported by the behaviour of the respective modes at sharp corners (see Fig. 1e,f and Fig. 3c,d of the main text). The orange mode (mode NT) traverses corners smoothly, as expected for a non-trivial mode protected against back scatter. In sharp contrast, the green mode (mode T) experiences significant back scatter.

2. TRANSMISSION FROM THE NANOBEAM WAVEGUIDE INTO THE TOPOLOGICAL WAVEGUIDE.

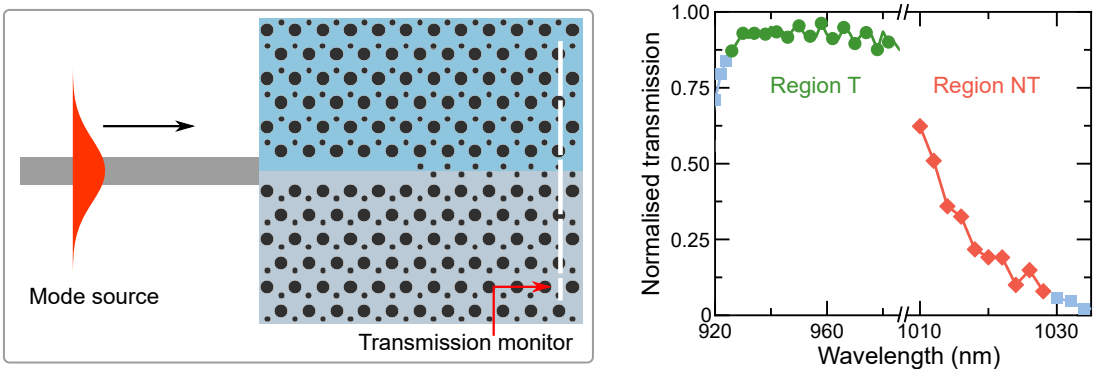

Fig. S2. (Left) Simplified schematic of the 3D FDTD simulation used to evaluate the transmission coefficient for the nanobeam-topological waveguide interface. A mode source is injected into the nanobeam waveguide on the left, and the transmission is monitored within the topological waveguide (white dotted line). (Right) Transmission from the nanobeam waveguide into the topological photonic crystal waveguide. The transmission is normalised to the power injected into the right-travelling mode of the nanobeam waveguide by the mode source. Green circles (orange diamonds) correspond to wavelengths within region T (NT). The blue squares correspond to wavelengths which lie outside the topological bandgap. The break in the abscissa corresponds to the slow light region of the topological waveguide band dispersion (see Fig. 1 of the main text). The average transmission is 92% (31%) for region T (NT).

3. SIMULATED CHIRAL MAP AND UNIDIRECTIONAL EMISSION FOR THE TOPOLOGICALLY TRIVIAL MODE T.

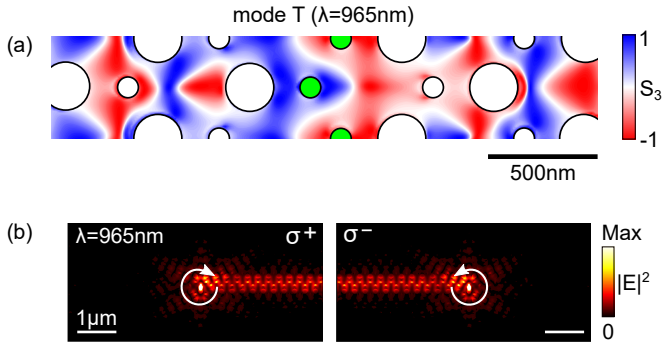

Fig. S3. Simulated chiral coupling of a dipole emitter to the topologically trivial mode T. (a) Normalised Stokes S_3 parameter as a function of position near the topological interface for a wavelength of 965nm (within the bandwidth of mode T). The holes at the interface are shown as green filled circles. The S_3 parameter was evaluated using FDTD simulations by injecting light into the waveguide and monitoring the resulting (complex-valued) electric fields as a function of position. (b) FDTD-simulated electric field intensity maps showing unidirectional emission from (left) σ^+ and (right) σ^- circularly polarised dipoles located at a position where $|S_3| \to 1$. Note that the waveguide is rotated by 90 degrees compared to the S_3 map in (a).

4. CHIRAL COUPLING OF A QD TO MODE T OF THE TOPOLOGICAL WAVEGUIDE.

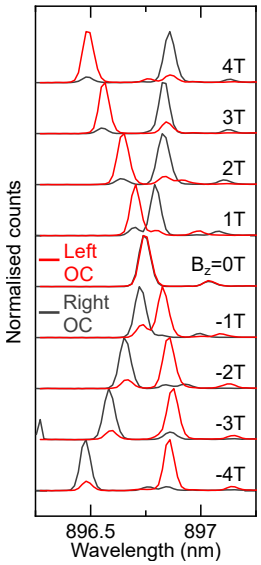

Fig. S4. Chiral emission from a QD coupled to mode T of a topological waveguide. A magnetic field in the Faraday geometry is used to lift the degeneracy of the two spin states of one of the QD's optical transitions. The emission is then measured independently from the left and right outcouplers (OC). At non-zero field the emission is clearly seen to be directional, with emission direction dependent on the handedness of the circular polarisation of the transition. The chiral behaviour is like that seen in topologically trivial glide plane photonic crystal waveguides [2] and arises from symmetry breaking of the photonic crystal lattice.

5. QD CHARACTERISATION: SINGLE PHOTON EMISSION AND DC STARK TUNING.

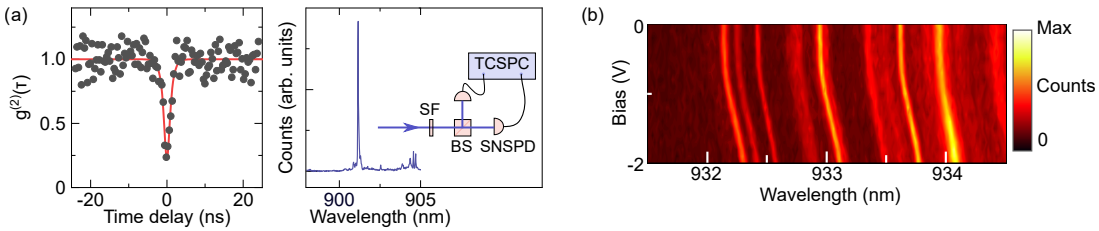

Fig. S5. (a) Hanbury Brown and Twiss (HBT) measurement on a single spectrally filtered QD emission line. The QD is located at the topological waveguide interface. The clear dip below $g^{(2)}(0) = 0.5$ ($g^{(2)}(0) = 0.09 \pm 0.08$, after deconvolution of the instrument response function) indicates that the QD is a single photon emitter. The QD spectrum prior to spectral filtering is shown to the right. The inset shows the detection experimental setup. SF – spectral filter; BS – beamsplitter; SNSPD – superconducting nanowire singe photon detector; TCSPD – time correlated single photon counter. (b) PL intensity map as a function of wavelength and bias, demonstrating Stark tuning of several QD transitions as the bias across the sample is varied. The QD(s) in question are located at the topological waveguide interface.

6. IDENTIFICATION OF THE SPECTRAL WINDOW FOR REGION NT IN A LINEAR WAVEGUIDE.

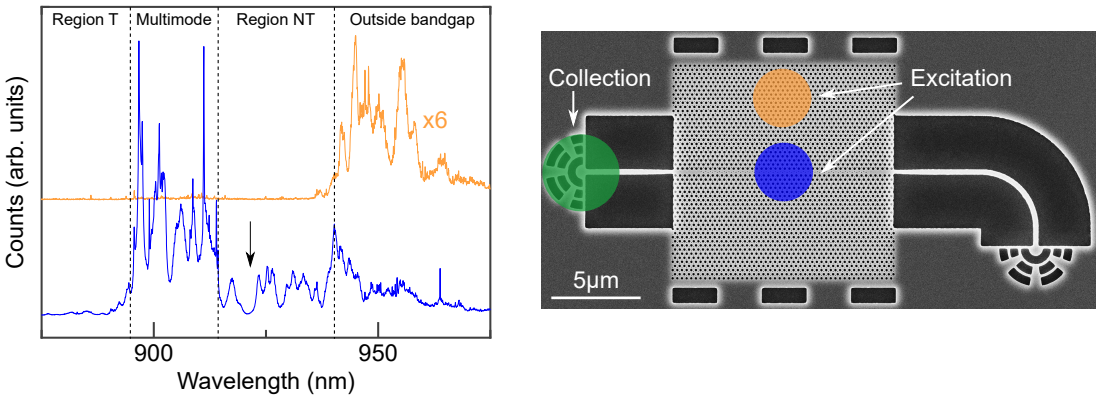

Fig. S6. (Left) PL spectra collected from one outcoupler under high power excitation of either the topological waveguide interface (lower blue trace) or the bulk photonic crystal (upper orange trace) for the waveguide considered in Figure 2b,d of the main text. The spectra are offset for clarity. The schematic to the right shows the excitation and collection locations. In the case of excitation of the bulk crystal, PL is only detected at wavelengths outside of the bandgap, seen on the long wavelength side with a cutoff at $\sim$ 940nm. By comparison with the photonic crystal bandstructure in Fig. 1c of the main text, the longer wavelength limit of region NT is therefore also $\sim$ 940nm. On the other hand, the slow light multimode window for the topological interface can be seen in the enhanced PL signal between $\sim$ 895nm and 915nm when exciting at the interface. This corresponds to a bandwidth of 20nm, which is in good agreement with that obtained from simulation. The short wavelength cutoff for single mode operation of mode NT is therefore $\sim$ 915nm, giving a region NT bandwidth of $\sim$ 25nm, also in good agreement with simulation. The chiral QD we investigate in Fig. 2d of the main paper has a transition at $\sim$ 921.5nm (indicated by the black arrow) and we therefore conclude that it is coupled to region NT of the topological waveguide.

7. SIMULATION OF A SINGLE 120-DEGREE TOPOLOGICAL WAVEGUIDE BEND.

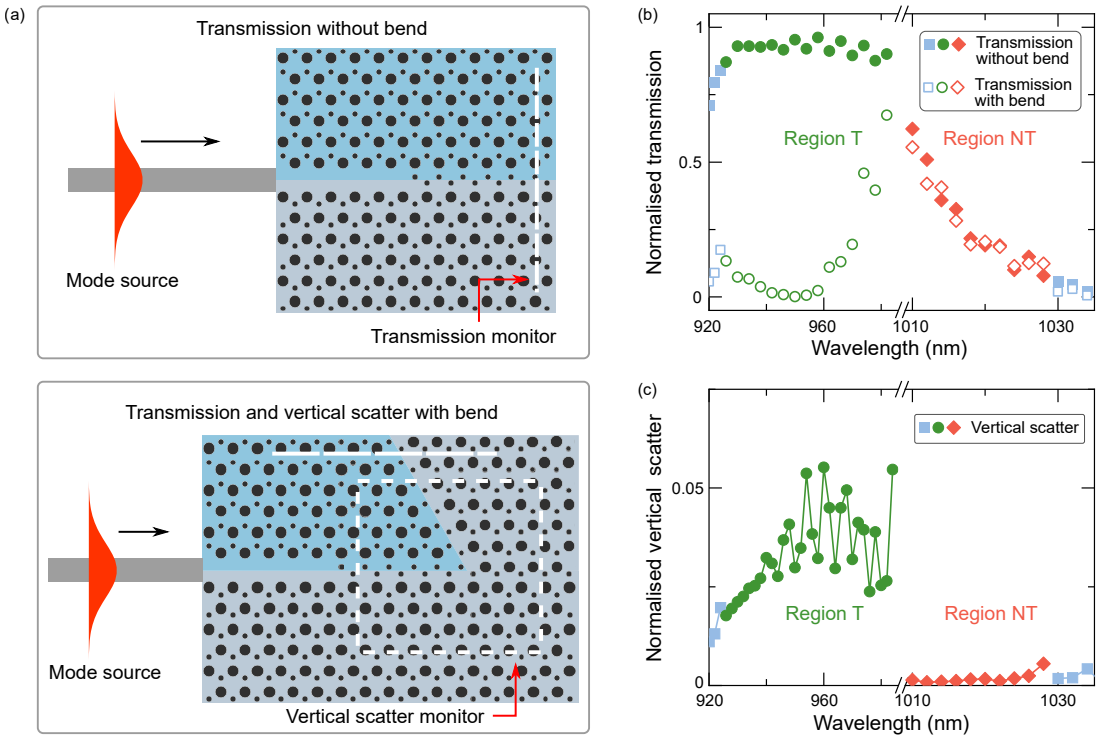

Fig. S7. (a) Simplified schematics of the 3D FDTD simulations used to evaluate (upper) the transmission coefficient of the nanobeam-topological waveguide interface and (lower) the transmission coefficient for a single 120-degree waveguide bend, as well as the vertical scatter caused by such a bend. (b) Normalised transmission for light injected into the nanobeam waveguide fundamental optical mode and subsequently coupled into the topological photonic crystal waveguide. The transmission is measured either without (filled symbols) or after (open symbols) a bend in the latter waveguide (see schematics to the right). (c) Normalised scatter measured (cumulatively) above and below the bend in the topological waveguide. Square monitors with side length of 3μm were placed above and below the bend, as shown in the schematic at the lower right (not to scale). The scattered power was normalised to the power which entered an equivalent topological waveguide in the absence of a waveguide bend. In (a-b), green circles (orange diamonds) correspond to wavelengths within region T (NT). The blue squares correspond to wavelengths which lie outside the topological bandgap. The break in the abscissa corresponds to the slow light region of the topological waveguide band dispersion (see Fig. 1 of the main text). In (b), the waveguide bend is seen to have no effect in region NT, whilst the transmission is strongly reduced in region T, demonstrating that the former is topologically protected. In (c), scattering out of plane is also seen to be strongly suppressed in region NT, in contrast to region T.

REFERENCES

1. H. Yoshimi, T. Yamaguchi, Y. Ota, Y. Arakawa, and S. Iwamoto, Slow light waveguides in topological valley photonic crystals, Opt. Letters **45**, 2648–2651 (2020).
2. I. Söllner, S. Mahmoodian, S. L. Hansen, L. Midolo, A. Javadi, G. Kirsanske, T. Pregnolato, H. El-Ella, E. H. Lee, J. Dong Song, S. Stobbe and P. Lodahl, Deterministic photon-emitter coupling in chiral photonic circuits, Nat. Nano. **10**, 775-778 (2015).

Chapter 5

A chiral topological add-drop filter for integrated quantum photonic circuits

A chiral topological add-drop filter for integrated quantum photonic circuits

M. Jalali Mehrabad,[1,*] A.P. Foster,[1,†] N.J. Martin,[1] R. Dost,[1]
E. Clarke,[2] P.K. Patil,[2] M.S. Skolnick,[1] and L.R. Wilson[1]

[1] *Department of Physics and Astronomy, University of Sheffield, Sheffield S3 7RH, UK*
[2] *EPSRC National Epitaxy Facility, University of Sheffield, Sheffield S1 4DE, UK*

The integration of quantum emitters within topological nano-photonic devices opens up new avenues for the control of light-matter interactions at the single photon level. Here, we realise a spin-dependent, chiral light-matter interface using individual semiconductor quantum dots embedded in a topological add-drop filter. The filter is imprinted within a valley-Hall photonic crystal (PhC) membrane and comprises a resonator evanescently coupled to a pair of access waveguides. We show that the longitudinal modes of the resonator enable the filter to perform wavelength-selective routing of light, protected by the underlying topology. Furthermore, we demonstrate that for a quantum dot located at a chiral point in the resonator, selective coupling occurs between well-defined spin states and specific output ports of the topological device. This behaviour is fundamental to the operation of chiral devices such as a quantum optical circulator. Our device therefore represents a topologically-protected building block with potential to play an enabling role in the development of chiral integrated quantum photonic circuits.

I. INTRODUCTION

Photonic crystals (PhCs) are a well-established component in nano-photonic circuitry, their sub-wavelength features supporting low-loss routing of light on-chip within a compact device footprint. Recently, the translation of concepts from the field of topological insulators to the photonic domain has provided new mechanisms for nanoscale control and manipulation of light within PhCs. Notably, photonic analogues of the spin-Hall [1] and valley-Hall [2] effects have been developed; significant advantages of these approaches include robust transport of light around tight bends, intrinsic backscatter immunity, and the potential to form chiral light-matter interfaces in combination with embedded quantum emitters. Devices containing topological photonic interfaces have been demonstrated experimentally using both spin- and valley-Hall PhCs, predominantly in the silicon [3, 4] and GaAs [5–10] material platforms. In particular, we note that bend robustness has been well established [3–5, 9, 11–13] and leveraged to form PhC topological ring resonators [6–8, 14].

Due to their preservation of time-reversal symmetry, both spin- and valley-Hall photonic analogues support degenerate counter-propagating interface modes, unlike their electronic counterparts. Nevertheless, the modes can be rendered unidirectional by spin selection. At locations known as chiral points, the counter-propagating modes of a topological waveguide have orthogonal circular polarisation. A circularly polarised emitter placed at such a point interacts uniquely with the mode with equivalent handedness, and therefore orthogonal circularly polarised dipoles emit in opposite directions; this is the basis of a chiral light-matter interface [15]. Semiconductor quantum dots (QDs), which have sub-nanosecond radiative lifetimes and have been shown to emit single photons with near-transform limited linewidths [16, 17], are a leading 'matter' candidate in this regard; chiral interfaces have been demonstrated using QDs coupled to both spin-Hall [5] and valley-Hall [6, 8] PhC waveguides. These works built upon substantial prior achievements in topologically trivial chiral systems, for instance those using atoms coupled to microresonators [18, 19] and QDs embedded in nanobeam [20, 21] or glide plane PhC [22] waveguides.

The field of on-chip topological quantum photonics is seeing rapid progress; for example, manipulation of quantum states of light has been demonstrated using relatively large topological photonic waveguide devices [23–26], while at the nanoscale a passive topological PhC devices was recently used as the basis for a simple quantum photonic circuit [27]. In contrast, the development of topological photonic devices with integrated quantum emitters is still very much in its infancy. Here, we combine the compactness and chirality afforded by topology to demonstrate chiral emission from a QD embedded in a valley-Hall PhC add-drop filter (ADF) comprising a resonator and pair of access waveguides. We first demonstrate that the device supports wavelength-dependent routing of light. Then, we observe chiral emission from a QD coupled spatially and spectrally to a resonator mode. In the latter measurement, photons emitted after recombination of a specific QD spin state are coupled into two of the four output modes of the device; the chiral nature of the light-matter interface results in the orthogonal spin state coupling to the other two output

* mjalalimehrabad1@sheffield.ac.uk
† andrew.foster@sheffield.ac.uk

modes. Such a device has potential applications in on-chip routing of light at the single photon level, for instance as a quantum optical circulator [28].

II. VALLEY-HALL RESONATOR DESIGN

Our integrated nano-photonic device is configured within a two-dimensional PhC which has valley-Hall-type topology. The rhombic unit cell of the PhC comprises two equilateral triangular apertures, which are formed within a thin, free-standing dielectric membrane. We evaluate the transverse electric (TE) band structure of the PhC using the freely available MPB software package [29]. When the apertures are of equal size, the TE band structure exhibits a Dirac cone at the K point (see Fig. 1a). Expanding one aperture while shrinking the other, however, leads to the opening of a topological bandgap at the K point, also shown in Fig. 1a. We can then take advantage of the topological bulk-edge correspondence to realise within the PhC a waveguide which supports a topologically non-trivial optical mode. To achieve this, we break the inversion symmetry of the PhC by inverting the unit cells in one half of the PhC, creating a zigzag interface at the boundary between the two regions comprising inverted (labelled VPC1) and uninverted (VPC2) unit cells, respectively. Two possible zigzag interfaces can be formed in this way, characterised by the proximity of either the large or small triangular apertures at the boundary of VPC1 and VPC2 unit cells. We refer to these as type A and type B interfaces, respectively, as shown in Fig. 1b. The associated dispersion diagram shows that both interfaces support a single guided TE mode, which extends across 100% ($\sim 84\%$) of the bandgap for the type A (B) interface.

Two defining characteristics of valley-Hall topologically non-trivial optical modes are (i) their broadband ability to navigate sharp corners without experiencing backscatter (due to the suppression of inter-valley scattering) and (ii) the helical nature of the modes. These properties are critical to the operation of the photonic device reported here. To demonstrate the backscatter protection afforded by topology to the waveguide mode, we use finite-difference time-domain (FDTD) simulations [30] to probe the optical properties of a rhombus-shaped ring resonator, formed by embedding VPC2 unit cells inside a larger VPC1 unit cell matrix, as shown in Fig. 1c. In this structure, a bend with

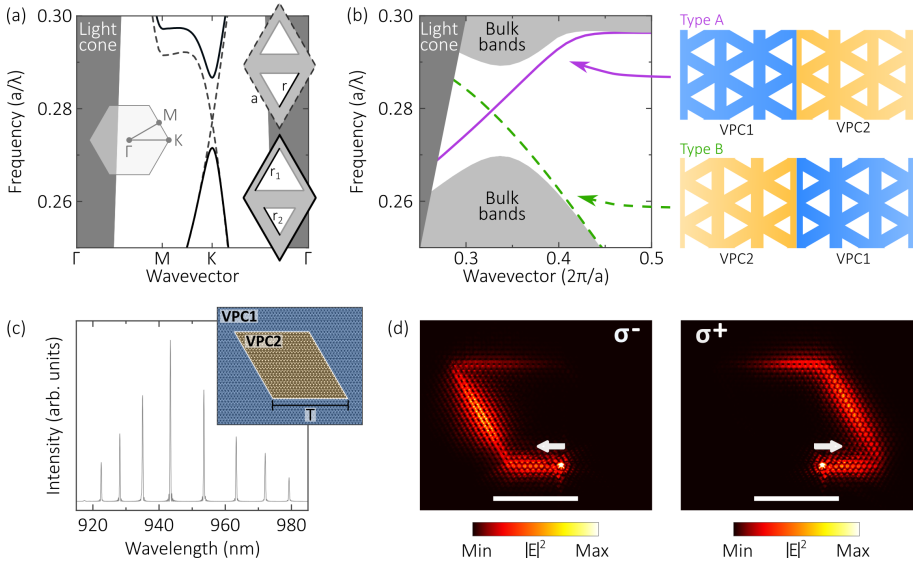

FIG. 1. (a) Band diagram for a triangular lattice PhC formed using either unperturbed (dashed line) or perturbed (solid line) rhombic unit cells. Insets show (left) the first Brillouin zone and (right) schematics of the unit cells, with equilateral triangles representing air holes in a dielectric membrane. The triangle side lengths are $(r, r_1, r_2) = (0.5a, 0.4a, 0.6a)$, where a is the lattice constant. The membrane has a thickness of $h = 0.64a$ and refractive index $n = 3.4$. (b) TE dispersion diagram for two possible zigzag interfaces formed by inverting the unit cells in one half of the PhC. These are labelled type A and type B in the accompanying schematics. (c) Simulated mode spectrum for a rhombic ring resonator formed using the topological zigzag interface. The resonator has a side length of $T = 20$ unit cells and lattice period $a = 266$nm. A schematic of the resonator is shown in the inset. (d) Simulated, spatially resolved electric field intensity when a resonator mode is excited by a dipole positioned at a chiral point on the interface. The dipole is either (left) σ^- or (right) σ^+ polarised. The electric field intensities are averaged over the first 200fs of simulation time. Arrows indicate the direction of light propagation in each case. Scale bars 4μm.

60 (120) degree internal angle connects interfaces of differing (the same) type, giving a maximum resonator spectral bandwidth of $\sim 84\%$ of the bandgap, following from the discussion above. The device parameters used in Fig. 1c are chosen to enable operation in the near infra-red (NIR), compatible with the highest quality QDs and the spectral region in which our later experiments are conducted.

The resulting mode spectrum reveals clear longitudinal modes lying within the topological bandgap ($\sim 920-980$nm), with Q factors of the order of 10^5 for a resonator side length of T=20 unit cells. Significantly, the predicted device performance is broadband in nature, indicating that topological protection overcomes the wavelength dependence commonly observed in light transmission through topologically trivial PhC waveguide bends. Further evidence of topological protection can be found in Fig. 1d, in which we excite the resonator using a circularly polarised dipole source. By suitable positioning of the dipole at a chiral point (see Supplementary Information section S1) a single unidirectional mode is excited, which travels either clockwise (CW) or counter-clockwise (CCW) around the ring, depending on the handedness of the source polarisation. The mode is seen to navigate the resonator corners smoothly and without backscattering. This simulation also serves to highlight the second key element of our device: the potential to realise a unidirectional light-matter interaction between a resonator mode and an embedded quantum emitter, which ultimately enables spin-dependent routing of light on-chip.

III. TOPOLOGICAL ADD-DROP FILTER

To enable integration of the resonator within scalable nanophotonic circuits, we introduce parallel 'bus' and 'drop' waveguides in close proximity to opposing sides of the rhombus-shaped resonator, forming an ADF. The filter is

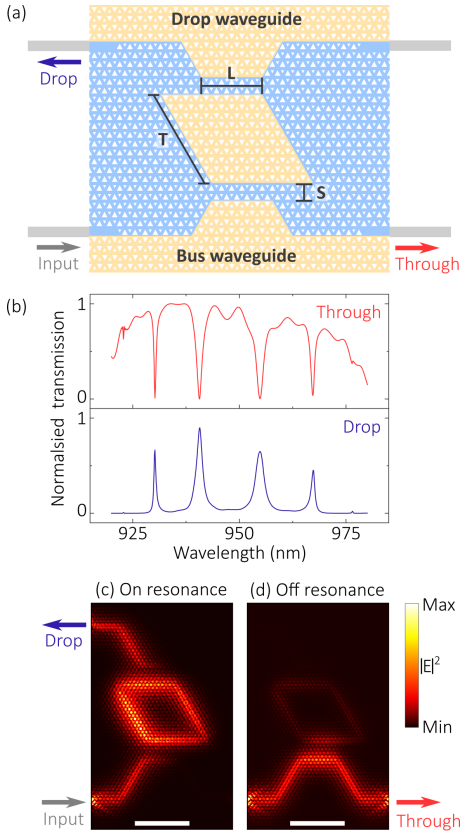

FIG. 2. (a) Schematic of the topological ADF, with PhC unit cells colour coded as in Fig. 1b by orientation (inverted (VPC1) or uninverted (VPC2)). (b) Simulated transmission in the through (lower right) and drop (upper left) directions for an ADF with T=16, S=6 and L=12 unit cells, respectively. The data is normalised to the maximum through transmission. Losses in the simulation stem predominantly from the incomplete optimisation of the nanobeam-photonic crystal interfaces. (c) Time-averaged electric field intensity for light input on resonance with the longitudinal mode at 955nm. (d) Time-averaged electric field intensity when the input is off resonance (969nm). Scale bars in (c,d) are 4μm.

shown schematically in Fig. 2a. Evanescent coupling between waveguides and resonator in this geometry enables light to enter (exit) the resonator from (into) the waveguides. Geometrically, the coupling strength is dependent on the waveguide-resonator coupling length L and separation S. In our structure, bends in each waveguide allow these parameters to be decoupled, providing increased flexibility in device design. The effect of changing S is investigated in Supplementary Information section S2.

The optical properties of the device are demonstrated using an FDTD simulation in which broadband light is injected into the bus waveguide, and the power subsequently transmitted through the bus waveguide or coupled into the drop waveguide is monitored. The simulation results are summarised in Fig. 2b-d. In the through direction, the transmission envelope represents the bandwidth in which the type A and B interface modes overlap spectrally. Within this bandwidth clear dips in transmission are observed at wavelengths which correspond to the longitudinal modes of the resonator. The dips occur due to destructive interference between the mode in the bus waveguide and light coupled back into this waveguide from the resonator. Corresponding peaks are seen in the drop channel signal, showing that light is transferred from the input waveguide to the drop waveguide when resonant with the ring modes. The degree to which the input light is dropped on resonance depends on the waveguide-resonator coupling strength, with critical coupling occurring for $S \sim 4-6$ unit cells (mode dependent). For the device simulated here, the loaded Q factors lie in the range 400-1600. Off-resonance, the dropped signal is strongly suppressed. Note that the dropped signal propagates in the opposite direction to the input signal due to a combination of valley momentum conservation and the use of both type A and B interfaces in the device. This is examined in detail in Supplementary Information section S3.

Experimentally, we fabricate the topological ADF within a nominally 170nm-thin, *p-i-n* diode GaAs membrane, which contains a single layer of InAs QDs within the diode's intrinsic region. A 1.15μm-thick AlGaAs sacrificial layer beneath the membrane is removed to create a free-standing structure. Details of the fabrication procedure can be found in the Methods. A scanning electron microscope (SEM) image of a representative device is shown in Fig. 3a.

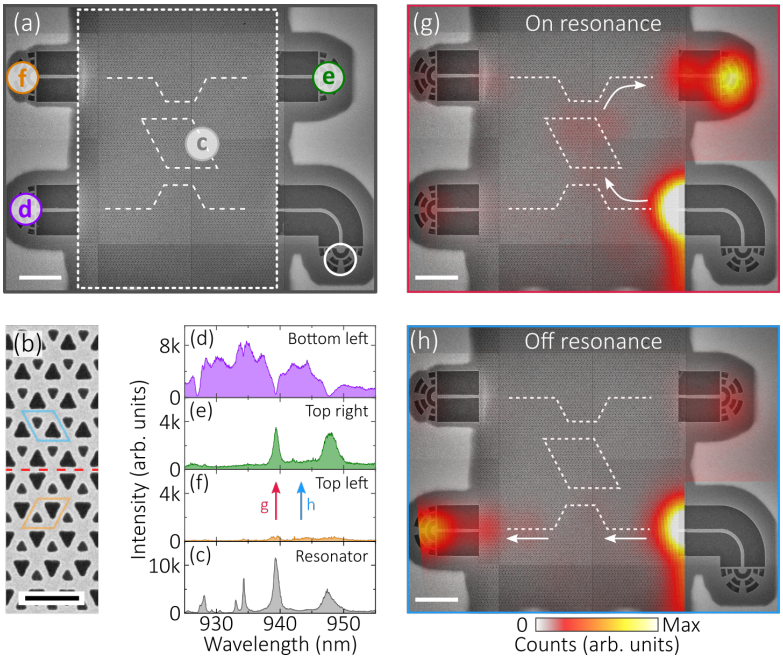

FIG. 3. (a) SEM image of a topological ADF, with waveguide-resonator separation S=6 unit cells. The topological interfaces forming the waveguides and resonator are highlighted by dashed white lines. (b) Higher magnification SEM image of a type A interface (red dashed line). Unit cells on either side of the interface are outlined. Scale bar 500nm. (c) PL spectrum acquired by exciting the QD ensemble at the resonator interface and collecting emission from the lower right OC (open white circle in (a)). (d-f) PL spectra acquired by exciting the QD ensemble in the lower right OC and collecting emission independently from the other three OCs. The collection position in each case is given in (a). (g,h) Integrated PL intensity as a function of collection position, overlaid on an SEM image of the device. The excitation is fixed above the lower right OC. The integration is taken over (g) 939.3nm to 939.5nm and (h) 943nm to 944nm, respectively. The waveguide and resonator interfaces are identified using white dashed lines, while arrows provide a guide to the the direction of light transmission. Data from above the excitation location (lower right corner) has been omitted, and the zero of the colour scale has been made transparent to aid visualisation of the device. Scale bars in (a,g,h) are 4μm.

Note that each output of the ADF is coupled to a nanobeam waveguide, which is terminated using a grating outcoupler (OC) for efficient coupling of light into free space optics. A higher magnification SEM image of a type A interface is shown in Fig. 3b.

To demonstrate the basic operation of the ADF, we inject broadband light into one waveguide via high-power non-resonant excitation of the QD ensemble, and monitor the transmission from the other OCs. We also evaluate the mode spectrum of the resonator itself in a separate measurement, by generating ensemble photoluminescence (PL) from a fixed position along the resonator interface. The resulting spectra are shown in Fig. 3(c-f). We first note that the resonator longitudinal modes are broadened due to evanescent coupling into the two waveguides. Quality (Q) factors of 1100 and 440 obtained for the modes at 939nm and 947nm, respectively, in good agreement with the range of values obtained from simulation.

Considering now the signal transmitted through the bus waveguide (Fig. 3d), we observe several strong dips in transmission which are resonant with the longitudinal modes of the resonator. Indeed, for three of the four modes the transmission is almost completely inhibited. (Note that the spectral envelope in the transmission measurement is governed by the emission from many different QDs, explaining the off-resonant, wavelength-dependent intensity.) In the drop direction (Fig. 3e), corresponding peaks are observed for the modes at 939nm and 947nm, showing that at these wavelengths, light is coupled from bus to drop waveguide via the resonator. Importantly, we see only very weak emission from the other end of the drop waveguide (Fig. 3f), demonstrating suppression of backscatter in the topological resonator.

Next, we focus our attention on the mode centered at $\sim$ 939nm, resonant with which the transmission of the bus waveguide approaches zero (suggestive of critical coupling). We step the collection spot in an x-y grid across the device while keeping the excitation laser fixed above the lower right OC, and acquire a PL spectrum at each collection position. The resulting data is spectrally filtered such that it corresponds to either on or off resonance with the longitudinal mode at $\sim$ 939nm. Spatial maps giving the integrated PL signal are shown in Fig. 3(g,h). On resonance, light is detected predominantly from the drop (top right) OC, showing that it is coupled through the resonator. Conversely, when off resonant the largest signal is from the left hand OC of the bus waveguide, bypassing the resonator. Scattering is also observed at the nanobeam-topological waveguide interfaces, which were not optimised in this device. More significantly, minimal scattering is observed from above the bends in the topological interface, testifying to their quality. A complementary measurement in which the excitation location was scanned whilst PL emission was collected from a single fixed OC is presented in Supplementary Information section S4.

Having demonstrated the basic function of the device, we now consider a second operational paradigm, in which we utilise single QDs embedded at the resonator interface. We first perform a Hanbury-Brown and Twiss (HBT) measurement on photons emitted from a QD which is coupled spectrally and spatially to a resonator mode. In so doing, we collect light into separate optical fibers from either end of one bus waveguide, therefore performing the HBT beam-splitting operation on-chip (see Supplementary Information section S5). We obtain a $g^{(2)}(0)$ of 0.14 after correcting for background emission from other QDs coupled to the same resonator mode, demonstrating the single photon nature of the QD emission.

Next, we investigate the chiral behaviour of a single QD in a similar device. A schematic of the structure and the measured resonator spectrum are shown in Fig. 4a and Fig. 4b, respectively. The QD is excited non-resonantly and PL emission is subsequently detected from all four ports of the ADF. The resulting spectra as a function of magnetic field are shown in Fig. 4c-f. Clear routing of light dependent on the spin state of the QD transition is observed. First, we consider the spectra obtained at $B_z = 0$T, for which the two spin states of the QD transition are degenerate, and note that a single PL emission line is observed from all output ports. Due to the statistical emission from both spin states of the QD, the source in this case is effectively unpolarised and therefore excites both CW and CCW resonator modes, which subsequently decay equally into the four output ports.

However, upon application of a magnetic field in the Faraday geometry, the Zeeman effect leads to spin splitting, giving rise to two non-degenerate, orthogonal, circularly polarised QD transitions. For a suitably positioned emitter, spin-momentum locking at the topological interface ensures that the direction of emission from the QD is dependent on the spin state. One of the spin states therefore couples to the CW resonator mode, while the other spin state couples to the CCW mode. The modes subsequently decay directionally into the two waveguides. Valley-momentum conservation results in a single resonator mode coupling to diagonally opposing ports of the ADF, and therefore a single QD spin state also couples in the same manner in our device. For instance, at a magnetic field of 3T the dominant emission line measured from the top left and lower right OCs is at longer wavelength, while the opposite is true for the other two OCs. When the sign of the magnetic field is flipped, the situation is reversed, with the shorter wavelength peak becoming dominant in the top left and lower right data. Thus, the device acts as a bidirectional chiral router for each spin state of the QD. FDTD simulations for σ^+ and σ^- dipoles placed at the resonator interface support the experimental observation (see Fig. 4(g,h)). Additional experimental data is shown in Supplementary Information section S6 for a second QD coupled to a different mode of the same device, demonstrating the broadband potential of the structure.

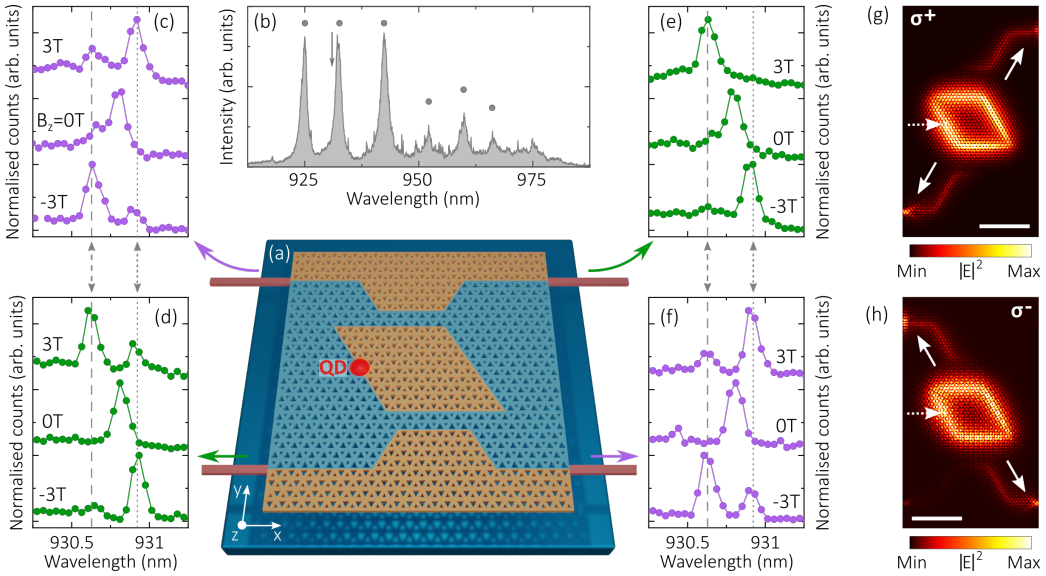

FIG. 4. (a) Schematic of the ADF, with a QD embedded at the resonator interface. Each of the four nanobeam waveguides is terminated with a grating outcoupler (OC), not shown. (b) PL spectrum acquired from an OC under high-power excitation of the resonator interface. The longitudinal resonator modes are marked by filled circles. The device parameters are (T,S,L) = (16,10,11) unit cells, respectively. (c-f) Low power PL spectra for a single QD located at the resonator interface and with an optical transition near-resonant with a longitudinal mode (see arrow in (b)). The spectra are acquired from the OCs in the (c) top left, (d) lower left, (e) top right and (f) lower right of the device, respectively. Data is shown for three different magnetic field strengths, $B_z = -3$T, 0T and 3T, respectively. Dashed and dotted lines indicate the approximate wavelengths of the two QD transitions under non-zero magnetic field. (g-h) Simulated, time-averaged electric field intensity in the plane of the device, for a (g) σ^+ or (h) σ^- polarised dipole placed at a chiral point at the resonator interface (approximate location given by the dashed arrow). Solid arrows indicate the dominant coupling directions from of the resonator in each case. Scale bars 4μm.

IV. DISCUSSION

We have demonstrated an integrated topological add-drop filter operating in the optical domain. The filter consists of a compact resonator coupled to a pair of access waveguides, defined within a valley-Hall topological PhC. Characterisation of the device using broadband emission from the QD ensemble indicates that near-critical coupling between the waveguides and resonator is achieved, allied with suppressed scatter, both in and out of plane. Chiral emission from a QD embedded within the resonator is also demonstrated. One spin state of a QD transition is shown to couple into two of the four output ports of the device, with the orthogonal spin state coupling to the other two output ports.

In future, optimisation of the device to increase the intrinsic (unloaded) resonator Q factor could enable broadband Purcell enhancement [31] of the chiral light-matter interaction. This might be achieved, for instance, by passivation of the semiconductor surface to suppress surface-related losses [31–33]. Scale up could then be envisioned; for example, cascaded chiral resonators could be used for the transport of entangled states on-chip [34]. Addressing the QD resonantly in the coherent scattering regime [35, 36] could ultimately allow for the realisation of a topologically protected quantum optical circulator [28].

V. METHODS

A. Device fabrication

The device layers were grown on a semi-insulating (100) GaAs substrate using molecular beam epitaxy. They are: 1μm $Al_{0.6}Ga_{0.4}As$, 30nm n-GaAs, 50nm $Al_{0.3}Ga_{0.7}As$, 5nm i-GaAs, InAs QDs, 5nm i-GaAs, 30nm $Al_{0.3}Ga_{0.7}As$ and 50nm p-GaAs.

Nanophotonic devices were fabricated using standard lithography and wet/dry etching techniques. A 120nm-thick SiO_x hardmask was deposited on the wafer using plasma enhanced chemical vapour deposition. This was followed by spinning of an electron-beam-sensitive resist (CSAR). The devices were subsequently patterned using 50kV electron

beam lithography (Raith Voyager) and then etched into the hardmask and epitaxial layers using reactive ion etching (RIE) and inductively coupled plasma RIE, respectively. The hardmask and AlGaAs sacrificial layer were removed using a hydrofluoric acid wet etch.

B. Experimental methods

The sample was mounted in a superconducting magnet cryostat (Cryo Industries of America) operating at 4.2K. PL measurements were undertaken using non-resonant laser excitation at 770nm (M Squared SolsTiS). For the creation of spatial PL maps, the excitation or collection spot was rastered across the sample using a motorized mirror in the microscope excitation or collection path, respectively. The use of a relay lens pair ensured that the laser and collection spots remained well-focused across the full scanning range during this process.

For autocorrelation (HBT) measurements, the sample was excited using an 808nm diode laser (Thorlabs CPS808). The signal was collected independently from either end of one bus waveguide, and coupled into separate optical fibers. Two 0.75m monochromators (Princeton Instruments SP-2750) were used to filter the output (filter bandwidth ~ 0.1nm) which was then detected using two avalanche photodiodes (Excelitas SPCM) with a convolved instrument response time of ~ 700ps. Photon arrival times were recorded and time-correlated using two channels of a time tagger (Swabian Instruments TimeTagger Ultra).

AUTHOR CONTRIBUTIONS

M.J.M. designed the photonic structures, which R.D. fabricated. E.C. and P.K.P. grew the sample. M.J.M., A.P.F. and N.J.M. carried out the measurements and simulations. L.R.W. and M.S.S. provided supervision and expertise. A.P.F. wrote the manuscript, with input from all authors.

ACKNOWLEDGEMENTS

This work was funded by the Engineering and Physical Sciences Research Council (EPSRC) (Grant No. EP/N031776/1).

[1] L.-H. Wu and X. Hu, Scheme for achieving a topological photonic crystal by using dielectric material, Phys. Rev. Lett. **114**, 223901 (2015).
[2] T. Ma and G. Shvets, All-Si valley-Hall photonic topological insulator, New Journal of Physics **18**, 025012 (2016).
[3] N. Parappurath, F. Alpeggiani, L. Kuipers, and E. Verhagen, Direct observation of topological edge states in silicon photonic crystals: Spin, dispersion, and chiral routing, Science Advances **6**, 10.1126/sciadv.aaw4137 (2020).
[4] M. I. Shalaev, W. Walasik, A. Tsukernik, Y. Xu, and N. M. Litchinitser, Robust topologically protected transport in photonic crystals at telecommunication wavelengths, Nature Nanotechnology **14**, 31 (2019).
[5] S. Barik, A. Karasahin, C. Flower, T. Cai, H. Miyake, W. DeGottardi, M. Hafezi, and E. Waks, A topological quantum optics interface, Science **359**, 666 (2018).
[6] S. Barik, A. Karasahin, S. Mittal, E. Waks, and M. Hafezi, Chiral quantum optics using a topological resonator, Phys. Rev. B **101**, 205303 (2020).
[7] M. Jalali Mehrabad, A. P. Foster, R. Dost, E. Clarke, P. K. Patil, I. Farrer, J. Heffernan, M. S. Skolnick, and L. R. Wilson, A semiconductor topological photonic ring resonator, Applied Physics Letters **116**, 061102 (2020).
[8] M. J. Mehrabad, A. P. Foster, R. Dost, E. Clarke, P. K. Patil, A. M. Fox, M. S. Skolnick, and L. R. Wilson, Chiral topological photonics with an embedded quantum emitter, Optica **7**, 1690 (2020).
[9] T. Yamaguchi, Y. Ota, R. Katsumi, K. Watanabe, S. Ishida, A. Osada, Y. Arakawa, and S. Iwamoto, GaAs valley photonic crystal waveguide with light-emitting InAs quantum dots, Applied Physics Express **12**, 062005 (2019).
[10] H. Yoshimi, T. Yamaguchi, Y. Ota, Y. Arakawa, and S. Iwamoto, Slow light waveguides in topological valley photonic crystals, Opt. Lett. **45**, 2648 (2020).
[11] J. Ma, X. Xi, and X. Sun, Topological photonic integrated circuits based on valley kink states, Laser & Photonics Reviews **13**, 1900087 (2019).
[12] X.-T. He, E.-T. Liang, J.-J. Yuan, H.-Y. Qiu, X.-D. Chen, F.-L. Zhao, and J.-W. Dong, A silicon-on-insulator slab for topological valley transport, Nature Communications **10**, 872 (2019).
[13] H. Yoshimi, T. Yamaguchi, R. Katsumi, Y. Ota, Y. Arakawa, and S. Iwamoto, Experimental demonstration of topological slow light waveguides in valley photonic crystals, Opt. Express **29**, 13441 (2021).

[14] L. Gu, Q. Yuan, Q. Zhao, Y. Ji, Z. Liu, L. Fang, X. Gan, and J. Zhao, A topological photonic ring-resonator for on-chip channel filters, J. Lightwave Technol. **39**, 5069 (2021).
[15] P. Lodahl, S. Mahmoodian, S. Stobbe, A. Rauschenbeutel, P. Schneeweiss, J. Volz, H. Pichler, and P. Zoller, Chiral quantum optics, Nature **541**, 473 (2017).
[16] A. V. Kuhlmann, J. H. Prechtel, J. Houel, A. Ludwig, D. Reuter, A. D. Wieck, and R. J. Warburton, Transform-limited single photons from a single quantum dot, Nature Communications **6**, 8204 (2015).
[17] F. T. Pedersen, Y. Wang, C. T. Olesen, S. Scholz, A. D. Wieck, A. Ludwig, M. C. Löbl, R. J. Warburton, L. Midolo, R. Uppu, and P. Lodahl, Near transform-limited quantum dot linewidths in a broadband photonic crystal waveguide, ACS Photonics **7**, 2343 (2020).
[18] C. Junge, D. O'Shea, J. Volz, and A. Rauschenbeutel, Strong coupling between single atoms and nontransversal photons, Phys. Rev. Lett. **110**, 213604 (2013).
[19] S. Rosenblum, O. Bechler, I. Shomroni, Y. Lovsky, G. Guendelman, and B. Dayan, Extraction of a single photon from an optical pulse, Nature Photonics **10**, 19 (2016).
[20] I. J. Luxmoore, N. A. Wasley, A. J. Ramsay, A. C. T. Thijssen, R. Oulton, M. Hugues, S. Kasture, V. G. Achanta, A. M. Fox, and M. S. Skolnick, Interfacing spins in an ingaas quantum dot to a semiconductor waveguide circuit using emitted photons, Phys. Rev. Lett. **110**, 037402 (2013).
[21] R. J. Coles, D. M. Price, J. E. Dixon, B. Royall, E. Clarke, P. Kok, M. S. Skolnick, A. M. Fox, and M. N. Makhonin, Chirality of nanophotonic waveguide with embedded quantum emitter for unidirectional spin transfer, Nature Communications **7**, 11183 (2016).
[22] I. Söllner, S. Mahmoodian, S. L. Hansen, L. Midolo, A. Javadi, G. Kiršanskė, T. Pregnolato, H. El-Ella, E. H. Lee, J. D. Song, S. Stobbe, and P. Lodahl, Deterministic photon–emitter coupling in chiral photonic circuits, Nature Nanotechnology **10**, 775 (2015).
[23] J.-L. Tambasco, G. Corrielli, R. J. Chapman, A. Crespi, O. Zilberberg, R. Osellame, and A. Peruzzo, Quantum interference of topological states of light, Science Advances **4**, 10.1126/sciadv.aat3187 (2018).
[24] Y. Wang, X.-L. Pang, Y.-H. Lu, J. Gao, Y.-J. Chang, L.-F. Qiao, Z.-Q. Jiao, H. Tang, and X.-M. Jin, Topological protection of two-photon quantum correlation on a photonic chip, Optica **6**, 955 (2019).
[25] A. Blanco-Redondo, B. Bell, D. Oren, B. J. Eggleton, and M. Segev, Topological protection of biphoton states, Science **362**, 568 (2018).
[26] S. Mittal, V. V. Orre, E. A. Goldschmidt, and M. Hafezi, Tunable quantum interference using a topological source of indistinguishable photon pairs, Nature Photonics **15**, 542 (2021).
[27] Y. Chen, X.-T. He, Y.-J. Cheng, H.-Y. Qiu, L.-T. Feng, M. Zhang, D.-X. Dai, G.-C. Guo, J.-W. Dong, and X.-F. Ren, Topologically protected valley-dependent quantum photonic circuits, Phys. Rev. Lett. **126**, 230503 (2021).
[28] M. Scheucher, A. Hilico, E. Will, J. Volz, and A. Rauschenbeutel, Quantum optical circulator controlled by a single chirally coupled atom, Science **354**, 1577 (2016).
[29] S. G. Johnson and J. D. Joannopoulos, Block-iterative frequency-domain methods for Maxwell's equations in a planewave basis, Opt. Express **8**, 173 (2001).
[30] Lumerical Inc., `https://www.lumerical.com/products/`, accessed: 26-05-2021.
[31] X. Xie, S. Yan, J. Dang, J. Yang, S. Xiao, Y. Wang, S. Shi, L. Yang, D. Dai, Y. Yuan, N. Luo, T. Cui, G. Chi, Z. Zuo, B.-B. Li, C. Wang, and X. Xu, Topological cavity based on slow-light topological edge mode for broadband Purcell enhancement, Phys. Rev. Applied **16**, 014036 (2021).
[32] B. Guha, F. Marsault, F. Cadiz, L. Morgenroth, V. Ulin, V. Berkovitz, A. Lemaître, C. Gomez, A. Amo, S. Combrié, B. Gérard, G. Leo, and I. Favero, Surface-enhanced gallium arsenide photonic resonator with quality factor of $6x10^6$, Optica **4**, 218 (2017).
[33] K. Kuruma, Y. Ota, M. Kakuda, S. Iwamoto, and Y. Arakawa, Surface-passivated high-Q GaAs photonic crystal nanocavity with quantum dots, APL Photonics **5**, 046106 (2020).
[34] W.-K. Mok, D. Aghamalyan, J.-B. You, T. Haug, W. Zhang, C. E. Png, and L.-C. Kwek, Long-distance dissipation-assisted transport of entangled states via a chiral waveguide, Phys. Rev. Research **2**, 013369 (2020).
[35] D. Rattenbacher, A. Shkarin, J. Renger, T. Utikal, S. Götzinger, and V. Sandoghdar, Coherent coupling of single molecules to on-chip ring resonators, New Journal of Physics **21**, 062002 (2019).
[36] A. Brooks, X.-L. Chu, Z. Liu, R. Schott, A. Ludwig, A. D. Wieck, L. Midolo, P. Lodahl, and N. Rotenberg, An integrated whispering-gallery-mode resonator for solid-state coherent quantum photonics (2021), arXiv:2107.12188 [quant-ph].

Supporting Information for: A chiral topological add-drop filter for integrated quantum photonic circuits

M. Jalali Mehrabad,[1,*] A.P. Foster,[1,†] N.J. Martin,[1] R. Dost,[1]
E. Clarke,[2] P.K. Patil,[2] M.S. Skolnick,[1] and L.R. Wilson[1]

[1] *Department of Physics and Astronomy, University of Sheffield, Sheffield S3 7RH, UK*
[2] *EPSRC National Epitaxy Facility, University of Sheffield, Sheffield S1 4DE, UK*

This file contains supporting information for the paper "A chiral topological add-drop filter for integrated quantum photonic circuits".

CONTENTS

* mjalalimehrabad1@sheffield.ac.uk
† andrew.foster@sheffield.ac.uk

S1. MODE PROFILES AND CHIRAL SPATIAL MAPS FOR THE TOPOLOGICAL INTERFACE.

Fig. S1 shows the electric field intensity distribution of the guided mode for the type A and type B valley-Hall zigzag topological interfaces, as introduced in Fig. 1 of the main text. Also shown in each case is the normalised Stokes S_3 parameter (degree of circularity) for the same cross-section of the waveguide. This is otherwise known as a chiral map, with regions of $|S_3| \to 1$ suppporting chiral coupling of an embedded emitter with circularly polarised transition dipole moment. Using the fields obtained from finite-difference time-domain (FDTD) simulations, the S_3 parameter was obtained from the expression

$$S_3 = \frac{-2\mathrm{Im}(E_x E_y^*)}{|E_x|^2 + |E_y|^2}, \tag{S1}$$

where S_3, E_x and E_y are dependent on x and y, with $z = 0$ (corresponding to the centre of the PhC membrane).

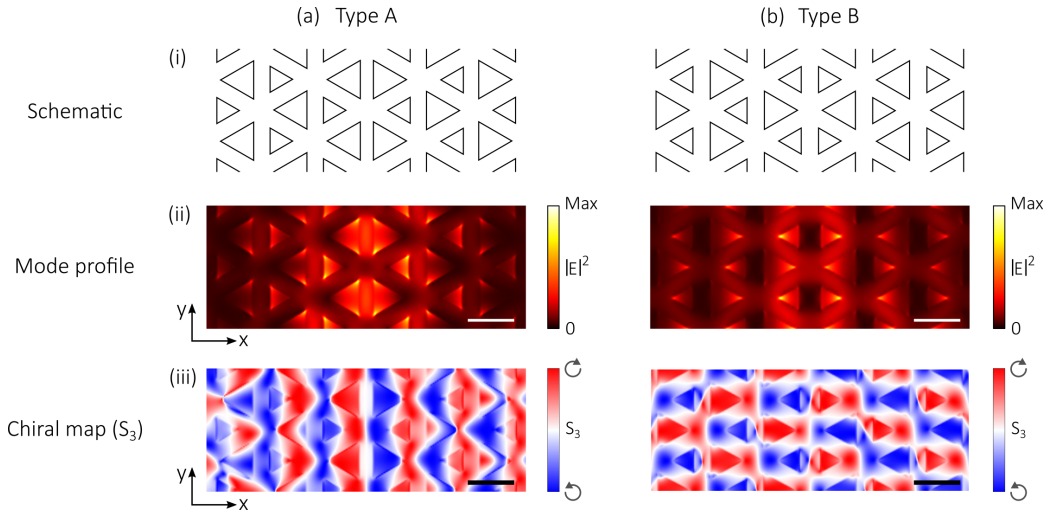

FIG. S1. Mode profiles and chiral maps for (a) type A and (b) type B valley-Hall zigzag topological interfaces, respectively. In each case (i) shows a schematic of the interface, (ii) gives the electric field intensity spatial map of the guided mode and (iii) shows the (normalised) S_3 Stokes parameter, giving the degree of circular polarisation of the mode as a function of (x, y) position. Scale bars in (b,c) are 200nm.

S2. CONTROL OF ADF COUPLING STRENGTH USING WAVEGUIDE-RESONATOR SEPARATION.

Here, we demonstrate control of the the add-drop filter (ADF) coupling strength at the design stage. To do so, we vary the waveguide-resonator separation S while keeping the parameters T and L constant (see Fig. S2a). By setting $S = 10, 6$ or 2 unit cells, the ring resonator and the bus and drop waveguides can be weakly, critically or over coupled, respectively. This is demonstrated in Fig. S2b, in which FDTD simulations are used to evaluate the time-averaged electric field intensity when light, resonant with the same longitudinal mode in each case, is injected into the drop waveguide of the ADF.

Next, we experimentally investigate structures with these same parameters using integrated photoluminescence (PL) intensity raster scans; the results are shown in Fig. S2d. For each of the three devices, we position the collection spot above the lower left outcoupler (OC) and raster scan the excitation laser across the device, as shown in Fig. S2c (this is the reverse of the collection raster scan used in the main text). By virtue of the spatially distributed nature of the QD ensemble, this approach effectively provides a user-positioned broadband light source with which to probe the optical response of the device. We integrate the measured PL intensity over a bandwidth corresponding to the same resonator mode in each case.

For $S = 10$, light from the drop waveguide weakly couples to the ring, and we see emission which originates from both waveguides, and from within the resonator. For the $S = 6$ case, in which the the mode is near-critically coupled, light is seen to couple through the resonator from the drop (upper) waveguide, while light from the other ends of the drop or through waveguides is not detected. This light is instead coupled via the resonator to the OC on the right hand side of the bus waveguide, in a mirror image of the data shown here. Finally, when $S = 2$, the resonator is overly coupled to the waveguides. In this scenario, the light coupled from the drop waveguide to the ring subsequently couples quickly to the bus waveguide.

Note that the approaches used to obtain the simulation data in Fig. S2b and experimental data in Fig. S2d are not directly equivalent; nevertheless, in combination they clearly demonstrate how changing the parameter S changes the resonator-waveguide coupling strength.

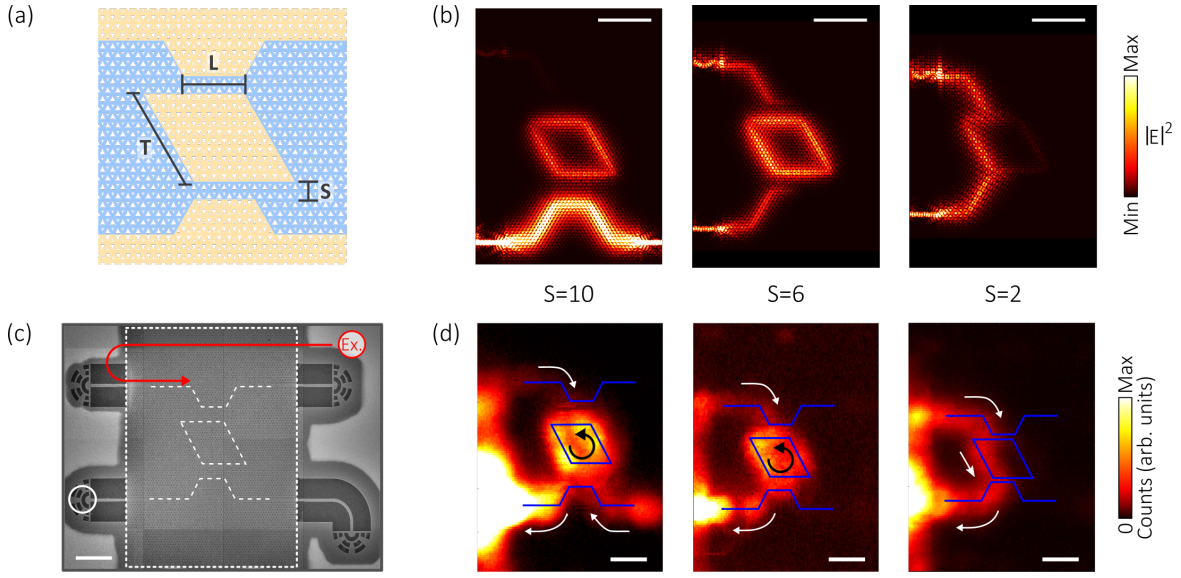

FIG. S2. Control of ADF coupling strength by changing the waveguide-resonator separation. (a) Schematic of the ADF. (b) Time-averaged electric field intensity spatial maps for three ADFs with different waveguide-resonator separation (from left to right, S=10, 6 and 2 unit cells, respectively). In each case, light which is resonant with a single longitudinal mode of the resonator is injected into the bottom left waveguide. (c) SEM of an ADF. Ex. - excitation spot location. (d) Integrated PL intensity spatial maps for devices with (left to right) S=10, 6 and 2 unit cells. PL is collected from the OC terminating the lower left output port, while the excitation laser spot is rastered across the device (indicated by the red arrow in (c)). In each case, the integration is taken over a single longitudinal mode at $\sim$ 1000nm. Solid blue lines give the positions of the waveguides and resonator. White and black arrows indicate the dominant direction of power flow. Scale bars in (b,c) are 4μm.

S3. VALLEY MOMENTUM CONSERVATION IN THE ADF.

The direction in which light propagates in the ADF depends on the interface type (A or B) and is dictated by valley momentum conservation [1]. This can be understood by considering the phase winding of the H_z field at the K and K' points in the Brillouin zone, and the dependence of the winding direction on the orientation of the PhC unit cell (and therefore the interface type). In Fig. S3a we plot the phase of the H_z field for the lowest frequency TE mode at the K and K' points, for both VPC1 and VPC2 PhCs. (The phase was obtained using the freely available MIT Photonic Bands (MPB) software package [2].) For a PhC formed using VPC1 unit cells, the phase at the K point winds by 2π in the clockwise (CW) direction about the centre point. When the unit cells are inverted (i.e. the PhC becomes VPC2-type) the phase rotates in the counter-clockwise (CCW) direction. Conversely, at the K' point the opposite behaviour is observed.

A type A interface is now formed by positioning a VPC1 PhC above a VPC2 PhC (i.e. separated in the y direction), with the resulting waveguide oriented along the x direction (see schematic 1 in Fig. S3b). At the K' point, the field vortices indicate that the interface mode will propagate in the positive x direction. Conversely, for a type B interface the VPC2 PhC is positioned above the VPC1 PhC, and the field vortices are therefore reversed. The K' interface mode in this case propagates in the negative x direction (see schematic 4 in Fig. S3b).

Within the ADF, there are six different combinations of interface type (A or B) and direction (inclined at 0, 60 or 120 degrees to the x axis). However, these can all be traced back to one of the two scenarios outlined above, by a suitable rotation of the waveguide. For instance, the interfaces in schematics 1, 2 and 3 in Fig. S3b are equivalent

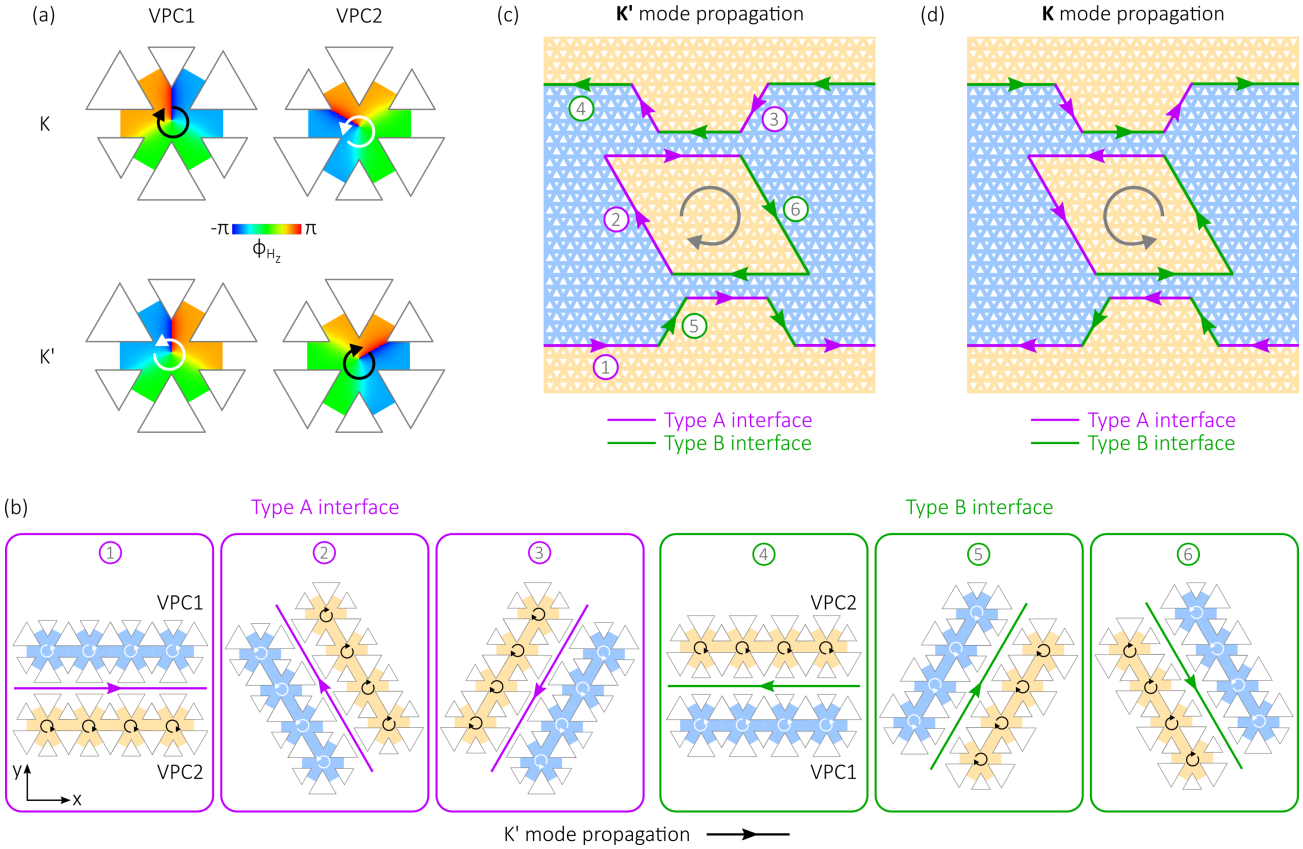

FIG. S3. (a) Phase vortices for the H_z field at the K and K' points of the lowest frequency TE band, for PhCs formed using either inverted (VPC1) or uninverted (VPC2) unit cells. (b) Schematic showing the direction of light propagation within the K' mode for the six possible combinations of interface type and waveguide orientation in the topological PhC. The phase vortices for the VPC1 and VPC2 unit cells are given by white and black circular arrows, respectively. Straight arrows for the type A and B interface propagation directions are coloured purple and green, respectively. Waveguides 1, 2 and 3 are equivalent, differing only by rotation; the same is true for waveguides 4, 5 and 6. All arrows are inverted for propagation in the K direction. (c,d) Schematic showing the direction of light propagation within the (c) K' or (d) K mode of an ADF.

other than by a rotation. The same is true for the interfaces labelled 4, 5 and 6. Using this basis, we indicate on a schematic of the ADF in Fig. S3c the direction of propagation for the K' mode. If light is injected into the right travelling mode in the bus (lower) waveguide, a CW resonator mode is subsequently excited; this decays into the left travelling mode in the drop (upper) waveguide. The reversed situation for the K mode is shown in Fig. S3d.

Using the above considerations, if light is injected into the K mode in the bus waveguide (i.e. propagating from right to left), transmission into the left travelling K' mode in the drop waveguide should be inhibited, as this necessitates flipping of the k-vector. In Fig. 3f of the main text, this suppression of coupling into the 'wrong' mode of the experimental drop waveguide is clearly seen.

Note also that topological protection should result in suppression of reflection by the ADF, as this also necessitates flipping of the k-vector. An observation along these lines has been made recently in an elastic wave spin-Hall system [3], in which topological protection prohibits quasi-spin flips.

S4. EXCITATION PL SPATIAL MAPPING.

In addition to the collection raster scans shown in in Fig. 3 of the main text, we have performed excitation raster scans on the same device. In this complementary measurement, we position the collection above the bottom right OC and raster scan the excitation laser across the device (the reverse of the collection raster scan shown in the main text). When the PL emission is spectrally filtered such that the emission energy is off-resonance with the mode, the (integrated) PL is seen to originate only from the through waveguide (Fig. S4c). In this scenario, the resonator and waveguide modes are decoupled. On resonance, however, light is detected which originates either from one end of the drop waveguide (i.e. coupled through the resonator), or from within the resonator itself (Fig. S4b). As the mode is near-critically coupled, light from the other ends of the drop or through waveguides is not detected. This light is instead coupled via the resonator to the OCs on the left hand side of the device, in a mirror image of the data shown here.

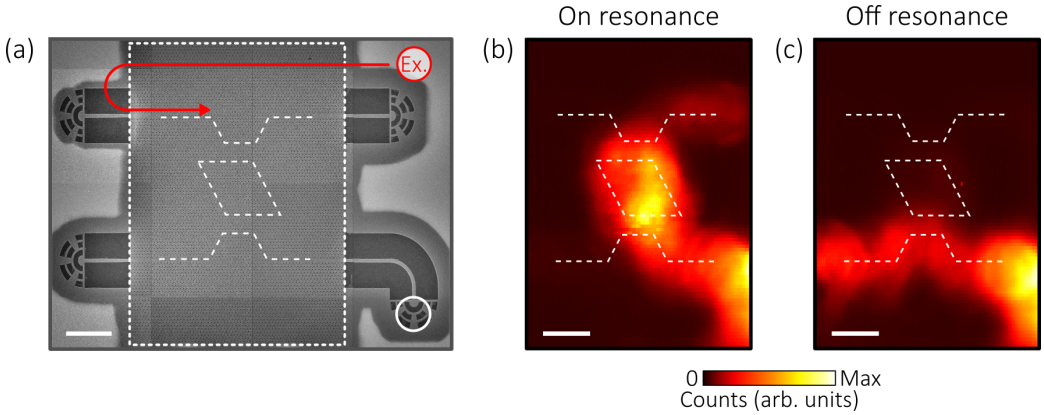

FIG. S4. (a) SEM of an ADF. Ex. - excitation spot location, which is rastered across the device. (b, c) Integrated PL intensity as a function of excitation position, for the device shown in Figure 3 of the main text. PL is collected from the OC terminating the lower right OC (white circle in (a)), while the excitation laser spot is rastered across the device. The integration is taken over (b) 939.3nm to 939.5nm or (c) 943nm to 944nm. Dashed white lines give the positions of the waveguides and resonator. The area shown in the maps corresponds to the dotted white box in (a). Scale bars in (a-c) are 4μm.

S5. ADF AS A SINGLE PHOTON BEAMSPLITTER FOR AUTOCORRELATION MEASUREMENTS.

Second order autocorrelation measurements (or Hanbury-Brown and Twiss (HBT) measurements) are a standard technique to demonstrate single photon emission from a quantum emitter such as a QD. Typically, one collects photons emitted by the QD and directs them to a pair of single photon detectors via a 50:50 beamsplitter. For a perfect single photon source, correlations between arrival times of the photons show complete suppression at zero time delay. Here, we use the add-drop filter itself as an on-chip beamsplitter. An SEM of the device is shown in Fig S5a. First, we identify the spectral position of resonator modes which are coupled to the bus waveguides. We probe the transmission of the lower bus waveguide by exciting ensemble PL from within the bottom right hand OC, detecting the signal from the bottom left hand OC. The resulting transmission spectrum is shown in Fig S5b, with several clear dips observed due to waveguide-resonator coupling.

Next, we identify a QD located within the resonator and coupled to the mode at $\sim$ 952nm. Using low power non-resonant excitation ($\lambda_{\text{laser}} = 808$nm), we collect PL simultaneously from both ends of the lower bus waveguide, as indicated in the schematic in Fig S5c. The QD couples to both CW and CCW resonator modes with similar efficiency, and the modes subsequently decay in either direction along the bus waveguide, thereby realising an approximately 50:50 beamsplitting operation. We filter the signal collected by both fibers using separate monochromators with $\sim$ 100pm filter bandwidth, with the signals prior to filtering shown in Fig S5d. Note that due to the relatively high density of QDs in the sample, the filtered signal still contains a contribution from QDs other than the target QD transition. We then correlate the arrival times of photons from either collection fiber using a pair of APDs and time tagging electronics. The result of the HBT measurement is shown in Fig S5e, with $g^{(2)}(0) = 0.53$ after deconvolution of the instrument response. If we then account for the signal to background ratio obtained from the filtered PL spectra, we obtain a corrected value of $g^{(2)}(0) = 0.14$, clearly demonstrating the single photon nature of the emission.

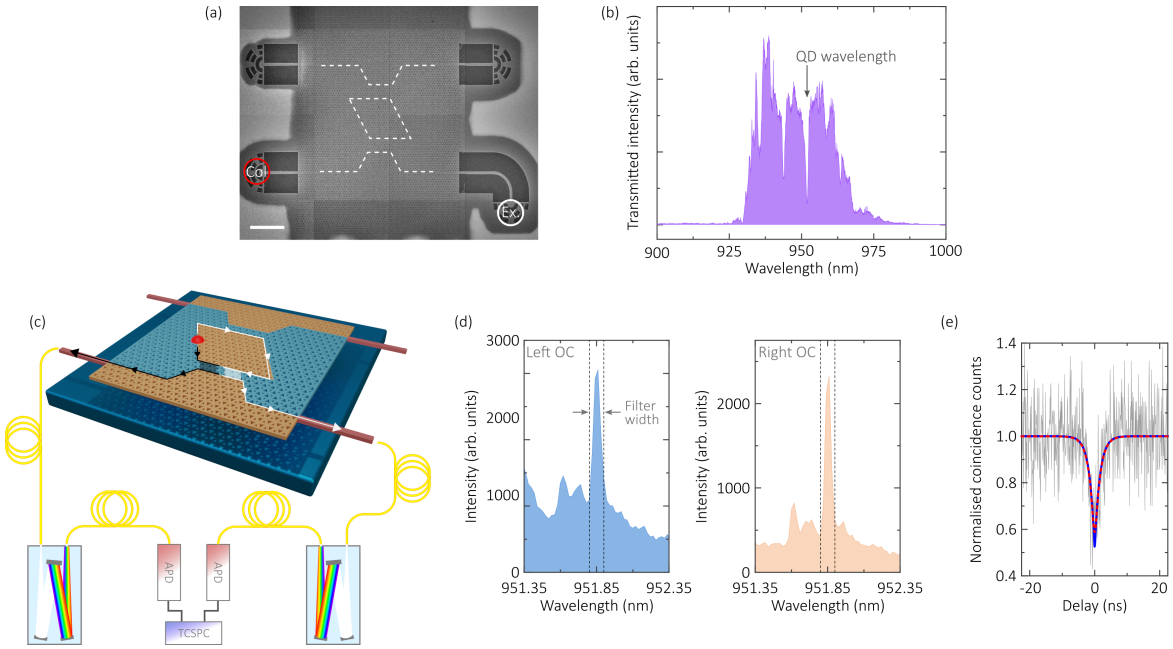

FIG. S5. (a) SEM of an ADF. Scale bar 4μm. (b) Transmitted PL spectrum acquired from the bottom left OC (red circle in (a)) after excitation of the QD ensemble in the bottom right OC. (c) Schematic of the HBT experimental setup. APD - avalanche photo diode; TCSPC - time correlated single photon counter. (d) PL spectra obtained from the left and right OCs of the waveguide in (c), respectively, when exciting a QD positioned at the resonator interface. The spectra are shown prior to spectral filtering. The QD transition is resonant with a cavity mode (arrow in (b)). (e) Second order auto-correlation measurement for the QD transition in (d). The red dashed line shows a convolved fit to the data, while the blue line shows the deconvolved fit, with $g^{(2)}(0) = 0.53$. The bin width is 100ps.

S6. BROADBAND NATURE OF CHIRAL COUPLING IN THE ADF.

Fig. S6 shows chiral coupling of a second QD to the device considered in Fig. 4 of the main text. Most importantly, note that the QD is coupled to a different mode of the resonator in this case. The QD is excited non-resonantly and PL emission is subsequently detected from the two ports on the right hand side of the ADF. The resulting spectra as a function of magnetic field are shown, clearly demonstrating routing of light dependent on the spin state of the QD transition.

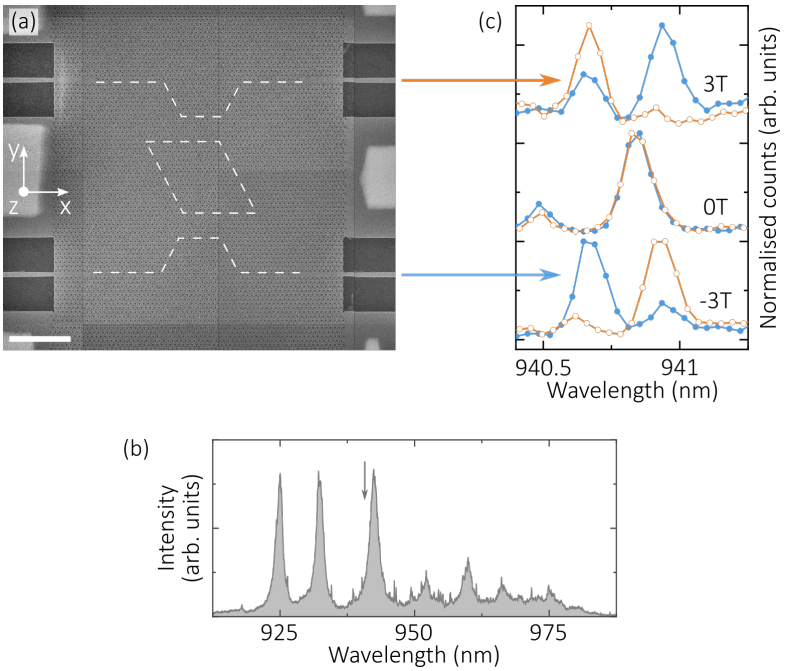

FIG. S6. SEM image of a representative ADF, with waveguide-resonator separation S=6 unit cells. Note that the measured device has S=10 unit cells. Dotted lines outline the waveguide and the resonator interfaces. Each nanobeam waveguide is terminated with an OC (not shown). Scale bar 4μm. (b) PL spectrum acquired from an OC under high-power excitation of the resonator interface. (c) Low power PL spectra for a single QD located at the resonator interface and with an optical transition near-resonant with a longitudinal mode (see arrow in (b)). The spectra are acquired from the OCs at the top right (orange line) and bottom right (blue line) of the device, respectively. Data is shown for three different magnetic field strengths, $B_z = -3$T, 0T and 3T, respectively.

[1] Y. Chen, X.-T. He, Y.-J. Cheng, H.-Y. Qiu, L.-T. Feng, M. Zhang, D.-X. Dai, G.-C. Guo, J.-W. Dong, and X.-F. Ren, Topologically protected valley-dependent quantum photonic circuits, Phys. Rev. Lett. **126**, 230503 (2021).
[2] S. G. Johnson and J. D. Joannopoulos, Block-iterative frequency-domain methods for Maxwell's equations in a planewave basis, Opt. Express **8**, 173 (2001).
[3] S.-Y. Yu, C. He, X.-C. Sun, H.-F. Wang, J.-Q. Wang, Z.-D. Zhang, B.-Y. Xie, Y. Tian, M.-H. Lu, and Y.-F. Chen, Critical couplings in topological-insulator waveguide-resonator systems observed in elastic waves, National Science Review **8**, 10.1093/nsr/nwaa262 (2020).

Chapter 6

Conclusion

The emerging field of topological photonics with embedded quantum dots offers a bridge between quantum optics and topology. This thesis presented the development of a number of novel topological nano-photonic devices, which were designed and studied to harness the intrinsic unidirectionality and robust propagation of topological states of light. Several key components of optical circuits, such as uncoupled and waveguide-coupled optical ring resonators were studied in details. Semiconductor QDs were then integrated in these devices to form a platform for on-chip generation and manipulation of single photons. The integrated topological quantum optics platform discussed in this thesis may serve as a stepping stone towards realization of topological effects and chiral quantum optics at the single photon regime with promising applications in quantum information science and technologies.

Leading on from the studies in this thesis, one can consider a number of possible directions and further investigations. One direction may be efficacy improvement of mode conversion between topological and non-topological (conventional) nano-photonic optical components. Another direction can be improvement of the ring resonator quality factors for investigation of non-linear optical effects. Chiral coupling of multiple quantum emitters in these systems can lead to the possibility of studying optical super/sub-radiance effects. Additionally, coupling between multiple ring resonators for optical filtering, QD-coupled slow-light topological waveguides and ring resonators for Purcell-enhanced chiral effects can be studied.

Appendix A

Electrical and Optical Properties of III-V Semiconductor QDs

A.1 Supplementary information

This section provides supplementary information on optical and electrical characteristics and relevant properties of SAQDs used for the work presented in this thesis.

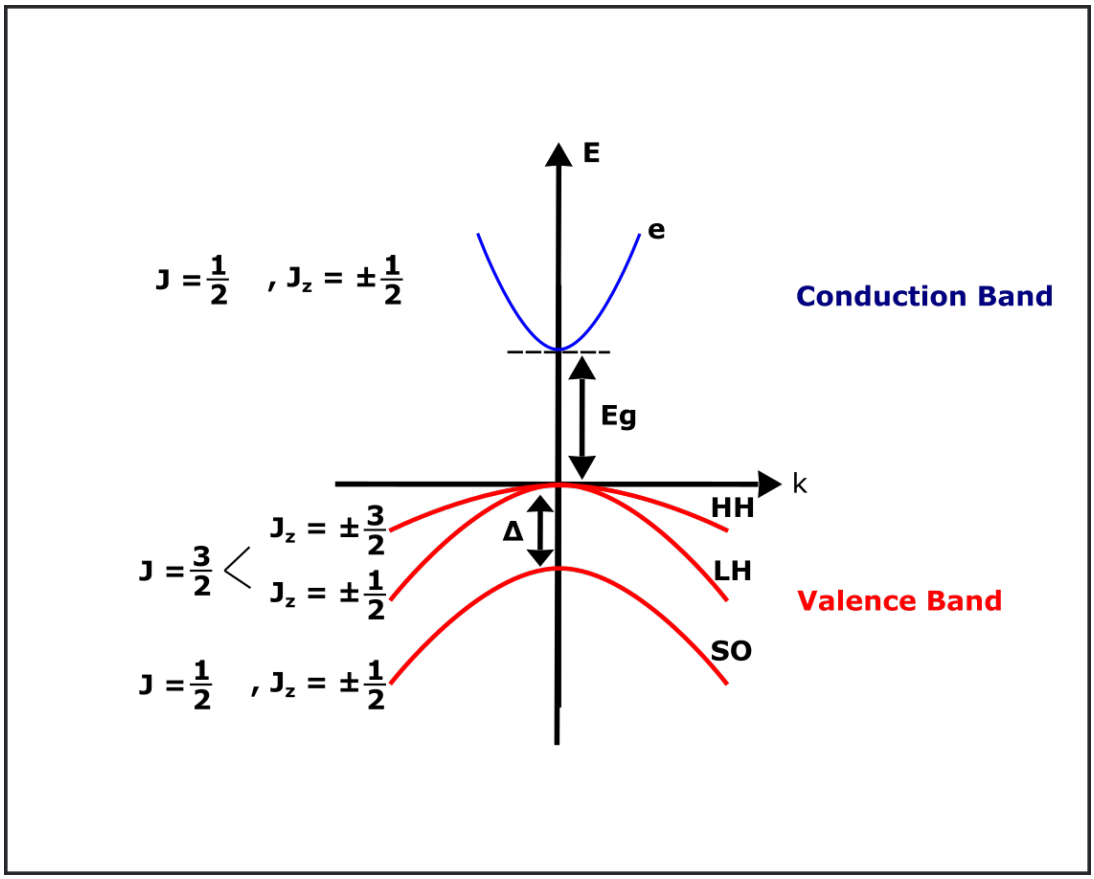

Figure A.1: Schematic band structure of a typical bulk III-V semiconductor. The bandgap (Eg) separates the single conduction band (blue curve) from the valence band (red), which consists of a heavy hole (HH), light hole (LH) and split-off (SO) band, respectively. Spin-Orbit splitting splits the SO band from the other valence bands by (delta). At k = 0 (Gamma point), LH and HH bands are degenerate, but they split as detuning from k = 0 is increased.

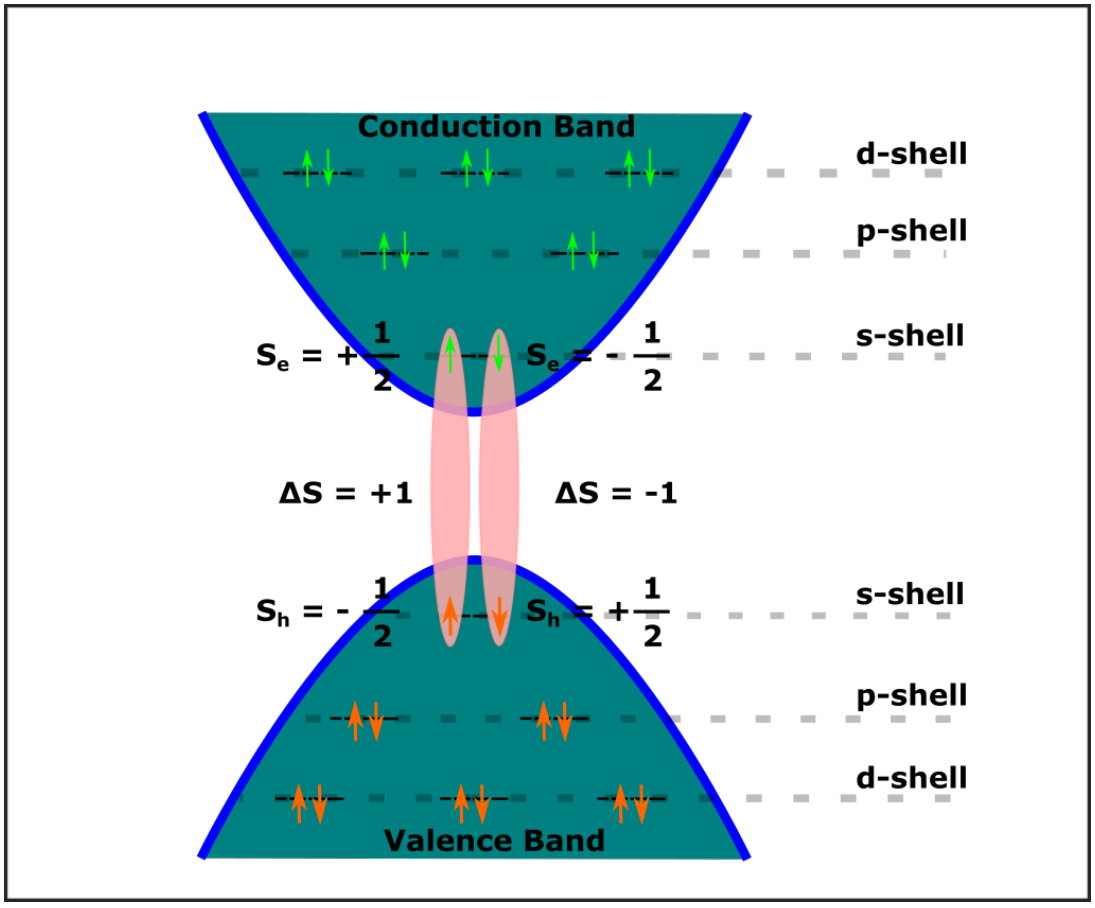

Figure A.2: Illustration of the level structure of a SAQD. Carriers have filled the s, p and shells. Shells may contain one, two or three pairs of Carriers (either electrons or heavy holes with opposite spins), respectively. The bright exciton states, which are highlighted in red, have opposite electron/hole spins.

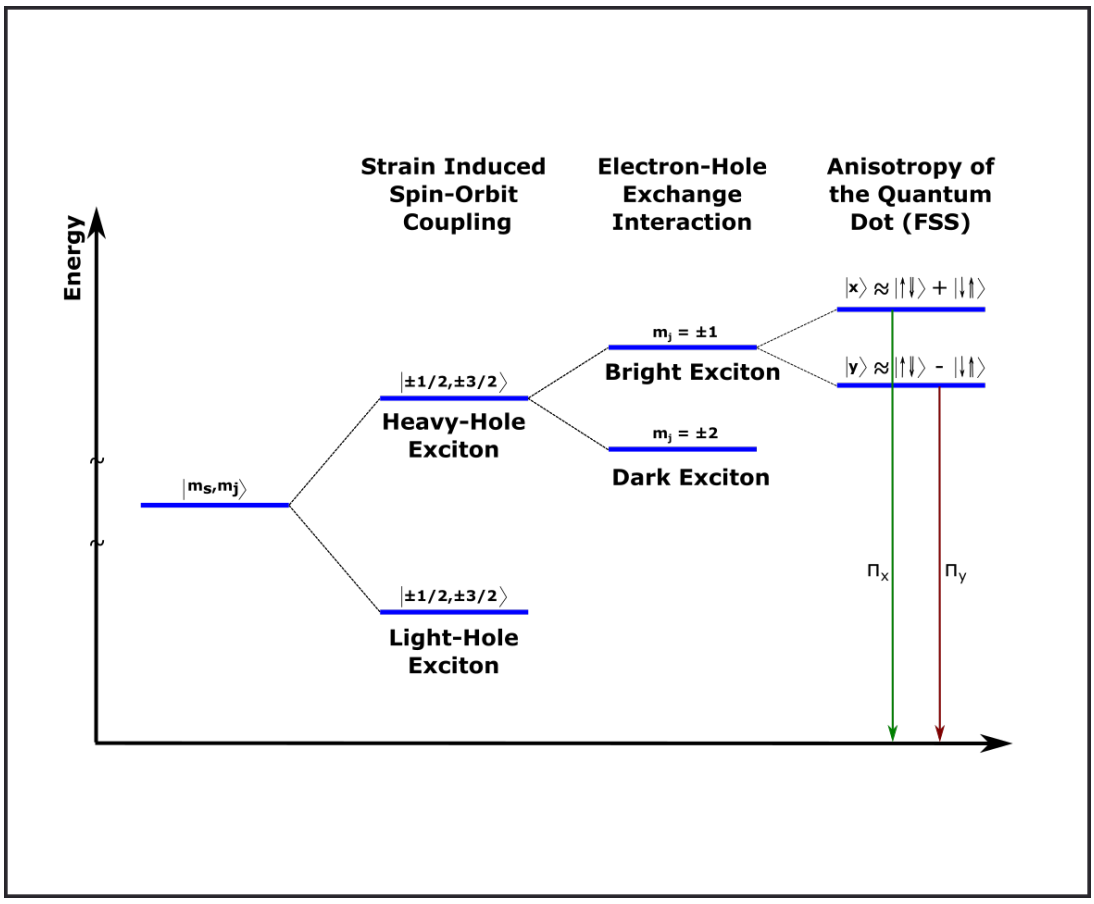

Figure A.3: Schematic diagram of the energy levels for a neutral exciton state in a InAs SAQD.

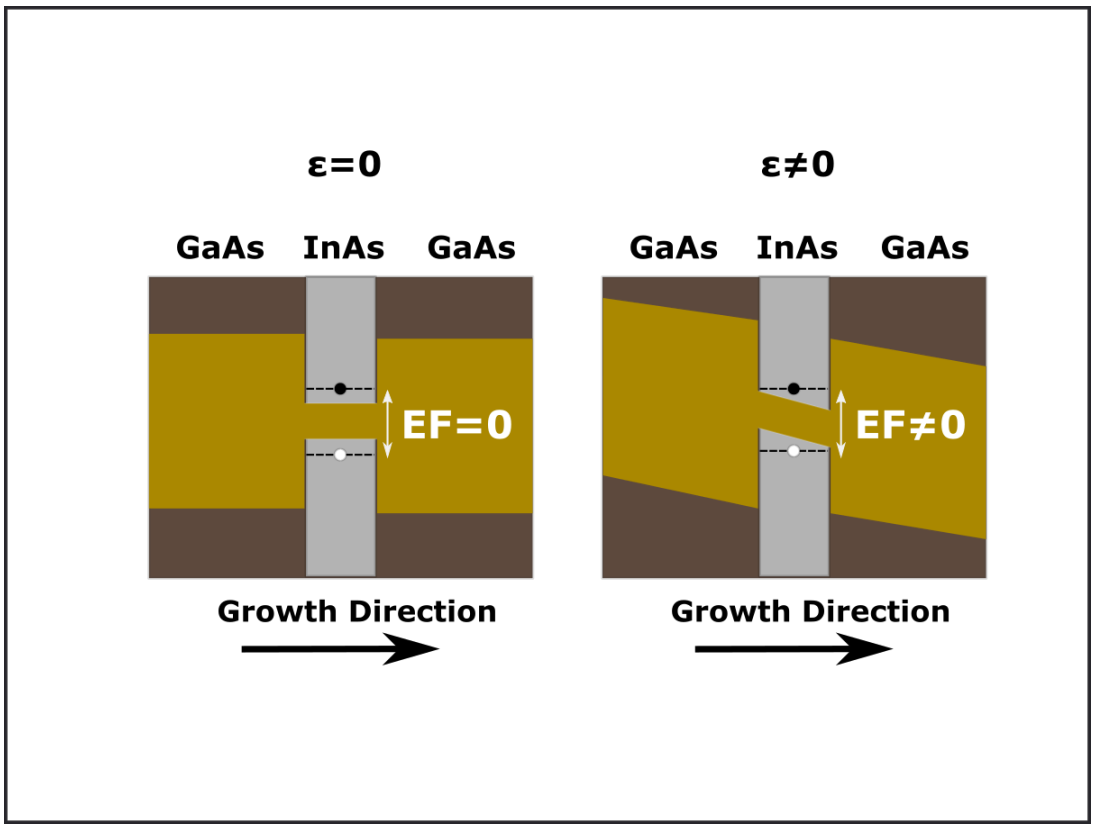

Figure A.4: Schematic illustration of electronic band structure of a SAQD in the (left) flat-band condition (no electric field) and (right) presence of electric field in the structure. An applied electric field results in a reduction of the energy difference between the states of the electron and hole.

Appendix B

Notes on the Papers Presented in Chapter Three and Four

B.1 Supplementary information

This section provides supplementary information and further discussions on the papers presented in this thesis.

B.1.1 Chapter Three: Experimental Quality Factors of the Ring Resonator

The GaAs wafer used in the paper presented in chapter three is a suspended, nominally 170nm thick p-i-n membrane with embedded InAs QDs, which is used for formation of the topological ring resonator. In such membranes, there can be several potential surface-related effects leading to lower experimentally measured Q factors than the simulations. Due to the thin, suspended nature of the structures, the surfaces have potentially much more effect than in a bulk microcavity.

These effects might include surface scattering due to surface roughness, imperfection in the verticality of side-walls of the PhC holes which can lead to out-of-plane scattering due to TM-TE coupling, in-plane absorption due to the high density of QDs embedded in the membrane, dopant related absorption and surface-related absorption due to oxidation. Passivation of the surface of such nanophotonic devices can strongly suppress the surface absorption and improve the Q factors. It is shown in [73, 74] how techniques such as surface passivtion and lifetime enhancement of free carriers can be used to significantly improve the experimental Q factors.

B.1.2 Chapter Four: Spin Vortices in the Ring Resonator

Vortices are phenomena with spin-texture which can arise in topological systems due to coherent superposition of counter propagating modes, leading to formation of quantised angular momenta (OAM) entities. They can be characterised by phase winding of an integer multiple of 2π around a core. A potential platform for realisation of vortices can be topological photonic systems, as shown recently in a photonic quantum Hall system [75].

The eigenstates of the valley-Hall topological ring resonators presented in chapter four can be discussed in terms of half-vortices or spin-vortices. The photonic quantum valley-Hall effect gives rise to in-plane propagation of photons coupled to counter-propagating modes confined to a two-dimensional membrane due to total internal reflection. Using the chiral modes of the topological ring resonator, one can introduce compact and integrated optical vortices formed from counter-propagating photons in the ring with opposite circular polarization.

The coherent superposition of the two chiral valley-Hall modes present in the ring resonator with anti-rotating OAM and opposite photon pseudo-spin may lead to new types of these topological entities, usually referred to as vector vortex beams in photonics [76]. These vortices are characterized by quantized polarisation winding instead of pure phase winding [77, 76].

The topological photonic ring resonators based on the quantum valley-Hall effect may enable the direct and integrated generation of such vortices from light travelling at the interface between two topologically dissimilar photonic structures. This could be a potential further investigation of the ring resonators presented in this thesis.